Investigation of the plate-impact method as a precursor of physical phenomena and chemical processes

Maya Mounir Daou

THÈSE DE DOCTORAT DE L'UNIVERSITÉ PIERRE ET MARIE CURIE

Spécialité : Génie des Procédés

École Doctorale de Sciences Mécaniques, Acoustique, Electronique et Robotique de Paris (ED 391)

Présentée par :

Maya Mounir DAOU

Pour obtenir le grade de

DOCTEUR DE L'UNIVERSITÉ PIERRE ET MARIE CURIE

Investigation of the plate-impact method as a precursor of physical phenomena and chemical processes

---

Dirigée par

Hélène PERNOT au Laboratoire de Réactivité de Surface

et Stéphane ZALESKI à l'Institut Jean le Rond ∂'Alembert

Soutenue à l'UPMC le 05 Octobre 2017 devant le jury composé de

Michel ARRIGONI	ENSTA Bretagne	Rapporteur
Daniel FUSTER	UPMC ∂'Alembert, Paris	Encadrant
Claude JOLIVALT	UPMC LRS, Paris	Examinatrice
Christophe JOSSERAND	Ecole Polytechnique, Paris-Saclay	Examinateur
Hélène PERNOT	UPMC LRS, Paris	Directrice
Javier RODRIGUEZ-RODRIGUEZ	UC3M, Madrid	Examinateur
Rhodri WILLIAMS	Swansea University	Rapporteur
Stéphane ZALESKI	UPMC ∂'Alembert, Paris	Directeur

"Out of suffering have emerged the strongest souls;
the most massive characters are seared with scars."

Gibran Khalil Gibran

Abstract This manuscript aims at characterizing a new device based on a plate impact on a liquid surface to generate cavitation and evaluate its potential to induce chemical reactions. The device is composed of a reactor containing a liquid that a piston hits due to pressure difference. This impact generates a strong and uniform pressure increase in the medium followed by a depressurization. We show that the gas/vapor layer trapped between the piston and the liquid free surface influences the pressure peaks and frequencies generated in the medium. High-speed camera visualization shows that depressurization activates nucleation sites leading to bubble appearance in the solution. Bubbles expand and collapse intensively generating high velocity jets under some conditions. We also investigate the response of pre-existing bubbles. We identify a critical bubble radius that depends on the impact height, external pressure and piston's characteristics. Bubbles with an initial radius larger than the critical one collapse at the moment of impact while smaller bubbles are only activated after it (under tension). Significant differences are observed in the pressure recordings after the impact depending on the presence/absence of large bubbles. We finally study the oxidation of phenol. We show that impacting on pure water is incapable of generating radical species responsible of the degradation. By adding hydrogen peroxide as an oxidant we show that the molecule is decomposed under certain conditions. In general, the amount of hydrogen peroxide required to initiate a significant oxidation decreases when increasing the intensity of the impact on which the degradation rate mainly depends.

Key-words Cavitation ; Bubble collapse; Solid-liquid impact; Oxidation reactions; Process intensification; Phenol

Résumé Ce manuscrit a pour but d'étudier un nouveau dispositif générateur de cavitation dont le potentiel favorable à l'intensification de réactions chimiques est évalué. Ce dispositif est constitué d'une plaque mobile qui frappe un liquide contenu dans un réacteur. L'impact génère une forte augmentation de pression dans le milieu suivi d'une dépressurisation. Nous montrons que la couche de gaz/vapeur piégée entre le piston et la surface du liquide influence les pics de pression et les fréquences générées dans le milieu. La visualisation à l'aide d'une caméra rapide montre que la dépressurisation active les sites de nucléation à l'origine des bulles de cavitation qui grandissent et implosent en générant occasionnellement des jets de grande vitesse. Nous étudions aussi la réponse de bulles préexistantes. Nous identifions un rayon de bulle critique qui dépend de la hauteur d'impact, de la pression extérieure et des caractéristiques du piston. Les bulles dont le rayon initial est supérieur à la valeur critique implosent au moment de l'impact, tandis que les petites bulles ne sont activées qu'après (sous tension). Des évolutions de pression différentes sont observées après l'impact en fonction de la présence/absence de grandes bulles. Nous étudions enfin l'oxydation du phénol en montrant que l'impact sur l'eau pure est incapable de générer des espèces radicalaires responsables de la dégradation. En ajoutant du peroxyde d'hydrogène comme oxydant, la molécule est décomposée sous certaines conditions. En général, la quantité d'oxydant requise pour déclencher une oxydation significative diminue lors de l'augmentation de l'intensité de l'impact sur lequel dépend le taux de dégradation.

Mots-clés Cavitation; Implosion de bulles; Impact solide-liquide; Réactions d'oxidation; Intensification des procédés; Phénol

Acknowledgements

This work has been accomplished from September 2014 to September 2017, carrying out the research work in Laboratoire de Réactivité de Surface (LRS) and Institut Jean Le Rond ∂'Alembert (IJLRA). I am therefore grateful to the laboratory directors, Hélène Pernot and Stéphane Zaleski for welcoming me in their respective laboratories during my PhD.

I want to start by thanking my advisers, Hélène Pernot and Daniel Fuster for guiding me and supporting me during these three years. I have always heard that each researcher has a scientific parent. Hélène, I am happy to call you my "scientific mother". You have encouraged me to move on and surpass myself because you believed in me. I see in you a role model and to that words betray me to express my gratitude. Daniel, you are the fighter. Together we have known lots of difficulties. You always found a way to set them aside and make me go on in my work. You also believed in me when I was in doubt. To that, THANK YOU.

I gratefully thank Guillaume Laugel for he has been the first to believe and trust in me. Guillaume, I will never forget the valuable discussions we had over the last few years. Whether for the internship, the PhD or life in general, your words have always been of such comfort. I hope that I have not let you down.

I also wish to thank Claude Jolivalt and Xavier Carrier for their advice, their support and all the scientific discussions which we had. Anne-Félicie Humblot, words are not enough to express the joy I had to meet a person like you. Your words still resonate in my mind. You are such a sweet soul. My deepest regards go also to Guillaume Legros for all his help throughout these three years.

I must also express my deepest gratitude and thanks to the all the LRS members. You have made both my internship and PhD experiences very pleasant. For all the support and love you have showed me, thank you. I mention in particular Annie Mettendorf, the times that you have comforted me are numerous, and you always had the best words. Laetitia Valentin, for all the laughs we shared, the help you provided me and the reassurance you showed me, thank you.

I also owe my earnest gratitude to all my friends and colleagues who shared with me my experience: Yara, Youmna, Johnny, Ashraf, Wadih, Vincent, I want to thank you for the laughs we shared, the comfort you attested towards me, the love you showed me and much much more.

I finally and most importantly thank my parents (Mounir and Maria), my sisters (Clara and Tania) and my grand- father (Afif). Words can never express how grateful I am. You have accepted me leaving you five years ago, you trusted me and showed me that distance does not matter when it comes to love. Tears are brought into my eyes when I think about the suffering that I have put you into, I just hope that I will always make you proud, as much as I am proud of you! Mona, you have been a second mother to me and you will always be. Petro and David, I hope to make you proud as well. Baby Ralph, I hope one day you will say that your aunt rocks!
A very special thought to Jean-François Krawczynski, a colleague in the past and a family member now and always. The love and support you showed me surpassed my expectations. Your wisdom and the beauty of your soul make you one special person. I am so lucky to have met you. Pierrette and Jean-Louis, I am so lucky to call you family.

My last thoughts go to Nohad, Eugénie, Elias, Samir D., Samir AA., Laudy, and all my beloved ones that are watching us from above.

Contents

List of Figures

List of Tables

Abbreviations

AOP	**A**dvanced **O**xidation **P**rocess
BPA	**B**is**P**henol **A**
CNT	**C**lassical **N**ucleation **T**heory
DO	**D**issolved **O**xygen
FID	**F**lame **I**onization **D**etector
GC	**G**as **C**hromatography
GR	**G**reen **R**ust
HPLC	**H**igh-**P**hase **L**iquid **C**hromatography
LLE	**L**iquid–**L**iquid **E**xtraction
MRR	**M**ethyl **R**adical **R**ecombination
PAA	**P**oly**A**cryl**A**mide
SBSL	**S**ingle **B**ubble **S**ono**L**uminescence
WAO	**W**et **A**dvanced **O**xidation

Symbols

A_{x}	The area of the peak related to the specie x
C	A constant
c_{l}	The speed of sound in the liquid
C_{m}	The mass concentration of hydrogen peroxide in the bottle
C_{x}	The concentration of x in the solution where x is a chemical molecule
$C_{\mathrm{H_2O_2}}^{bottle}$	The concentration of hydrogen peroxide in the bottle
d	The distance between two plates for the displacement of the lower piston
D_f	The dilution factor
D^{M}	The averaged mass diffusivity of the gas/vapor mixture
ΔP	The difference between the bubble's internal and external pressures
D^{T}	The averaged thermal diffusivity of the gas/vapor mixture
F	A force
f_{max}	The maximal generated frequency extracted from Daubechies wavelets
f_N	The bubble's natural frequency
γ_{eff}	The effective polytropic coefficient of the gas/vapor mixture
H	The position of the upper piston
H_0	The initial impact height of the upper piston
h_{c}	The thickness of the gas/vapor layer at $t_{U_{max}}$
$H_{0,\mathrm{l}}$	The height of the liquid in the reactor
k_{x}	The response factor of the specie x
m_{p}	The upper piston's mass
N	The number of impacts of the piston
n_{x}	The number of moles of the chemical specie x
$P_{\mathrm{top},0}$	The initial pressure under the piston at $t < 0$
P_{atm}	The atmospheric pressure

P_{bott}	The temporal pressure at the bottom of the reactor
Pe	The Péclet number
Pe_{c}	The critical Péclet number
$\overline{P_{\text{int}}}$	The effective pressure in the reactor
Pe	The external pressure surrounding the reactor
P_{max}	The pressure around the bubble
P_{vap}	The saturated pressure of the liquid at ambient temperature
P_{top}	The temporal pressure under the piston
$P_{\text{top,max}}$	The maximal temporal pressure under the piston
P_{liq}	Liquid's initial pressure
P_{v}	The pressure of the bubble at R_{max}
R_{c}	The critical radius of the bubble for which $t_{\text{i}} = t_{\text{Rayleigh}}$
R_{bub}	The radius of the bubble
R_{max}	The maximal radius of the bubble
R_{min}	The minimal radius of the bubble
R_0	The initial radius of the bubble
S_{bub}	The section of the bubble
S_{p}	The section of the piston
t_{col}	The collapse time of the bubble
t_{i}	The compression time of the gas/vapor layer
t_{Rayleigh}	The Rayleigh collapse time
$t_{U_{max}}$	The time when $V = U_{\text{max}}$
$T_{\text{max}}^{\text{bubb}}$	The maximal temperature inside the bubble when $R = R_{\text{min}}$
T_{max}	The initial temperature of the medium
U	The velocity of the piston
U_{bub}	The total velocity of the bubble
U_{flow}	The velocity of the flow
U_{max}	The maximal velocity of the piston
U_{min}	The minimal velocity of the piston
V_{tot}	The total volume of the solution
V	The volume of the gas/vapor layer
V_{x}	The volume of the solution containing the specie x
x	A chemical species (H_2O_2 or C_6H_5OH)

$\rho_{\mathrm{H_2O_2}}^{mother\ sol}$	The density of the mother solution of hydrogen peroxide
ρ_l	The density of the liquid
λ	Wavelength

To my parents,
grand-father,
sisters and brothers-in-law,
Ralph and JFK,
and the memory of my beloved ones.

General introduction

Motivation and objectives

When, for some reason, the pressure of a liquid maintained at a constant temperature suddenly drops, vapor bubbles can grow in the liquid bulk in a process similar to boiling. This localized change of state within the liquid volume is referred to as cavitation. This process is usually associated with the violent collapse of bubbles, promoting turbulence and mixing at very small length-scales making this phenomenon interesting to intensify processes limited by heat and mass diffusion.

Cavitation can be generated by different means based on pressure variation in a liquid using for example ultrasound, hydrodynamic machinery or by pressure variation induced after the impact of a solid substance on a liquid. The spectrum of applications based on the dynamic response of bubbles to pressure changes evolves in fields as different as medicine, material synthesis and waster water treatment techniques.

Industrial waste water treatments are as varied as the industries themselves, the treatment and depollution methods being function of the composition and concentration of their contaminants. Waste characteristics vary within a single industry over time and become unpredictable. The contents of the effluents can vary in composition with the presence of inorganic waste to extremely toxic organo-chemical substances. Having different chemical and physical properties, there exists different techniques to treat waste waters among which techniques based on cavitation proved their efficiency in recent years.

It is in this context that this work has been conducted. To design new systems able to control and enhance processes promoted by the collapse of bubbles remains a major challenge nowadays. This motivates the investigation of processes at laboratory scale in controlled conditions with the aim at clarifying the role of each separate mechanism promoted by the collapse of bubbles on the global intensification of chemical processes.

The purpose of this work is to characterize a novel experimental apparatus based on the impact of a piston on a liquid surface and to evaluate the potential of this technique to induce chemical reactions in the system.

Outline

The manuscript is divided into five chapters.

Chapter 1 presents the principal aspects of cavitation-based techniques applied to waste water treatment and a review of the relevant literature. The interest in developing new devices and techniques due to limitations in the currently used devices is stressed out. The cavitation phenomenon is briefly re-introduced with a particular attention given to techniques based on the occurrence of tension states to promote the appearance of bubbles. Finally, the efficiency of cavitation-based techniques applied to waste water treatment, in particular the oxidation a model molecule, the phenol, is also discussed.

Chapter 2 deals with the experimental facility, the equipment and the measurement techniques used in this work. Some characteristic parameters related to the piston impact are discussed such as its maximal velocity and the pressures induced in the medium upon the impact. Based on this analysis, two configurations of the device are compared and their effect on the system response are also discussed. Some of the work presented in this chapter is published in Daou et al. [2].

The bubble dynamic response to the piston impact is discussed in Chapter 3. A critical parameter is introduced to differentiate bubbles based on their radii. Image recordings of large bubbles allowed to divide their behavior into two characteristic stages and to relate their characteristic collapse time with their maximal radii. The behavior of small bubbles is also investigated showing that the current technique is able to induce jet formation during the collapse of bubbles. Some of these results are published in our work [2].

Chapter 4 explores the possibility of using the plate-impact technique to induce chemical reaction processes. Based on its wide use in literature and its presence in industrial discharges, phenol is chosen as a model molecule. Its oxidation is studied in the presence of an oxidant, hydrogen peroxide. Impacts on pure water and on hydrogen peroxide are used to unveil the effects of different physical and chemical parameters on the process of phenol's oxidation.

Finally, a general conclusion and some perspectives for further studies are given.

Chapter 1

Bibliographical Review

Contents

To develop a sense of existing works combining the understanding of the dynamic response of bubbles and chemical reactions, this chapter first provides an overview of the previous work describing the cavitation phenomenon (section 1.1). The chemical activity induced by cavitation with a further insight on cavitation-based techniques for chemical processes are then summarized in section 1.2. This chapter concludes with a review of waste water treatment techniques and the usual contaminants with an emphasis on the toxicity and eco-toxicity of a model molecule found in industrial discharges and extensively used in the literature, the phenol (section 1.3).

1.1 Cavitation: description of the physical phenomena

1.1.1 Introduction

Whether depressurizing the liquid medium (like in a nozzle or around the helices of a boat) or heating it (like in boiling or using a laser beam), using a dynamic or a static method, the mechanisms of bubble nucleation and their dynamic response arose a large interest among researchers of different domains like chemistry, fluid mechanics/dynamics, physics or biology.

Cavitation is a phenomenon at the origin of bubble appearance when the liquid's pressure is decreased. It can be defined as the process of formation of a vapor phase in a

liquid when this liquid is subjected to a depressurization. The vapor phase formation is almost identical to the boiling of a liquid. However, boiling is achieved by the addition of heat thus increasing the temperature of the fluid up till its boiling point. In cavitation, it is generally assumed that the process occurs at constant temperature by lowering the pressure of the medium below its saturation pressure. It is important to differentiate between cavitation and flashing. During the latter, the vapor formed will remain in the gaseous phase. Cavitation is therefore defined as a thermodynamic change of phase with mass transfer from liquid to vapor phase and the other way around which makes cavitation bubbles implode when the pressure increases. In all these processes, bubbles appear due to the presence of small impurities or microscopic gas bubbles called nucleation sites.

The ability of a liquid to sustain a tension (negative pressure) before it eventually cavitates is known since long time[3,4]. Cavitation was first detected in 1894 by Reynolds[5] who observed and reported the boiling of water in an open tube at ordinary temperatures. This was the result of the pressure drop of the water passing by a converging-diverging glass tube. However, the word cavitation was introduced a year later when it was recognized as the reason why a new British destroyer, HMS *Daring*, failed to reach its designed speed. Indeed, the thrust of the propellers failed to develop sufficiently: as the screw sheared into the water, it created a wake of holes or voids which grew into a large cavity as the speed rose, changing the shape of the pressure profile on the screw and reducing its efficiency[6]. The contribution of cavitation to the damage of solid materials was firstly investigated in the twentieth century by Parsons and Cook[7]. Ever since, cavitation has been widely studied and continues to be an intense topic of research on a fundamental basis[8,9] (and references herein) or an applicative/industrial basis[10–14].

1.1.2 Tension states, nucleation sites and cavitation inception

Liquids can be put in a meta-stable condition[15] (and ultimately generate cavitation) in two different ways: first by super-heating it above its boiling temperature and second, by stretching it below its saturated vapor pressure. An interesting review is proposed by Caupin and Herbert[16]. The existing techniques can be classified based on whether they are static or dynamic.

The method of cooling, also known as the Berthelot tube[4] owes its name to its inventor Marcellin Berthelot. Its various stages are briefly as following: a hermetically glass or steel sealed tube is almost completely filled with the test liquid whereas the remaining volume is a mixture of air and liquid vapor. Upon heating, the liquid expands until it completely fills the tube at a certain filling temperature, T_f (the air being forced into

the solution). This generates positive pressure in the liquid. Next, the tube is cooled slowly ($T < T_f$) and the liquid continues to expand and adheres to the internal walls. The liquid's pressure decreases to become null then negative (tension) until the liquid breaks at a lower breaking temperature T_b. In his first experiment, Berthelot [4] noted a sudden increase in the external volume of the tube because of the release of tension in the liquid at the same time. The Berthelot tube method raised interest on both the experimental [17–20] and theoretical [17,18,21–23] aspects.
Only one method based on the Berthelot tube can attain the cavitation pressure predicted by the classical nucleation theory (CNT) which is around $-140\,\mathrm{MPa}$ at room temperature [24,25]. It consists in cooling microscopic inclusions of aqueous fluids (micrometer size water droplet for example) trapped in quartz or other crystals in such a way that the liquid, which sticks to the hydrophilic walls, follows an isochore (constant density path) [26–29].

Another static application to put liquids under tensions is the centrifugal method. Lord Reynolds was the first to report this centrifugation method [30]. It consists in rotating a tube containing the test liquid, both ends of the tube being opened and at atmospheric pressure. When spun, a negative pressure develops on the rotation axis. As the spinning velocity increases, the pressure decreases and becomes negative. At a certain critical spinning velocity, the liquid inside the tube ruptures: knowing the value of the critical velocity, one can calculate the breaking tension.
In 1950, Briggs [31] reported that in a Pyrex glass capillary Z-shaped tube, a breaking tension of about $-25\,\mathrm{MPa}$ was recorded at $10\,^{\circ}\mathrm{C}$. This was the highest experimental value recorded for distilled water using this method at that time. Briggs also determined the influence of the temperature variation of the liquid on the tension recorded. Winnick and Cho [32] proposed an interesting centrifugal force method but were not capable of going beyond Brigg's limit. They were however able to measure the volume expansion of liquids under negative pressures.

Discrepancies between the theoretical and experimental tensile strength values seem to be related to the presence of heterogeneous (nucleation) sites at the origin of tensile failures in liquids. Determining the tensile strength dynamically revealed to be a way of surpassing this barrier. Indeed, the maximum tensile strength is generated in the bulk solution away from the solid-liquid interfaces, with experiments of short duration so that complexities related to the presence of appearing and disappearing bubbles are minimized and the dynamic method allows to study the kinetics of the failure process [33].

Liquids can be put under tension when a pressure wave is reflected at an interface between water and a medium with lower acoustic impedance[a] such as air. A well known example of this principle is underwater explosions. They have been used in many fields such as in radio-acoustic or for the investigation of underwater sound propagation. Preliminary studies started during the second world war by some independents and nowadays the general character of underwater explosions is well established (refer to Cole [34]).

When a high explosive is detonated underwater, the detonation wave propagates through the liquid and converts it into gas at a very high pressure. Then, a shock wave is radiated into the fluid. When the shock wave reaches the surface, it is reflected as a tension wave which may cause cavitation. When considering a relatively smooth surface of the water, this surface could be disturbed to a certain extent as s function of the detonation intensity. Indeed, when the detonation is sufficiently strong to generate to the same extent a strong shock wave, the area above the explosion charge may form a dome (of broken water). Wilson et al. [35] showed that by determining experimentally the initial velocity of the dome U_0 using a high-speed camera, the tensile strength can be evaluated by extrapolation of Equation 1.1 to when U_0 is null using:

$$U_0 = \left(\frac{2}{\rho_\mathrm{l} U_\mathrm{w}}\right)\left(P - \frac{P^\mathrm{neg}}{2}\right), \tag{1.1}$$

where P is the maximum pressure of the explosion,P^neg is the negative pressure in the reflected shock wave ρ_l the density of the liquid and U_w the pressure wave velocity.

Another technique highly used in research and also based on the dynamic stress of a liquid is called the bullet- piston method. It has the same principle as underwater explosions. The experimental set-up consists of firing a bullet at a piston fitted into the bottom of a vertical cylindrical tube containing the liquid. This technique revealed inconsistent results when it came to the tensile values in water in comparison to the Berthelot tube for example. Sedgewick and Trevena [36] reported a value of the tensile strength F for deionized water by the bullet-piston method equal to 1 MPa whilst Jones et al. [20] recorded 4.6 MPa using the Berthelot tube for water. Several attempts have been made to explain the reason behind these inconsistencies. Temperley and Trevena [37] proposed the idea of a meta-stable transition layer (between liquid and vapor) at the surface of water making it an imperfect reflector for a pressure wave incident upon it. Williams and Williams [38] proved that this explanation was erroneous. Indeed, through an improved version of the bullet-piston apparatus, they came to the conclusion that the anomalously low values of F determined in previous experiments based on the reflection principle are to be attributed to the deficiencies in the technologies used to record

[a] Acoustic impedance is a measure of the amount by which the motion induced by a pressure applied to a surface is impeded. It can be calculated as the ratio between pressure and velocity.

dynamic tensions. In 1969, Couzens and Trevena[39] demonstrated that the evolution of the (F, P) curve reaches a "*plateau*" which value is determined according to the experimental conditions. Indeed, Sedgewick and Trevena[40] determined the values of F for divers kinds of water whilst Overton and Trevena[41] proposed a new way of presenting the experimental data. The latter included several portholes in their tube at different depths and displayed the data as (tension, depth) graphs. After determining the critical depth, i.e. the depth at which the incident and reflected pulses are separated (no longer overlap), they varied the piston's length and the bullets' nature before plotting the resulting tension peaks F as a function of the peak pressure in the incident pulse P. As in Couzens[39], the authors found a "*plateau*".

It is worth mentioning that studies based on the reflection of a wave on a suitable liquid-solid interface also exist (see for example Carlson and Henry[42]). Using an interferometric technique to monitor the motion of a Mylar film, the authors determined the tensile strength in glycerol at room temperature using pulsed electron beam deposition on a solid target (Astrel 360). The stress pulse produced in the plate was transmitted to the liquid and then reflected as a tension wave at a Mylar film causing it to move.

Another way of generating tensions in liquids is by producing the tension pulse *ab initio* in the liquid by an impact. One way is through the tube-arrest technique. In his attempt to study bubbles' dynamics, Chesterman[43] chose a method which he qualified as "of extreme simplicity". He used a vertically mounted, half water filled glass tube which was normally at rest against a rubber buffer. When pulled down against rubber-tensioned supports and released, the tube rose vertically before being arrested by the buffer. By continuing its vertical motion and causing a tension pulse, the liquid (water) generated a cavity near the bottom of the tube. Overton and Trevena[41] proposed a similar experimental apparatus and presented using a transducer, the pressure changes in the liquid that they related to bubbles radii variations. They also proposed an explanation of the oscillatory nature of the pressure records.

Using the water shock tube method, tension is either generated directly or by reflection (of a positive pulse). In the former case, the tensile pulse is the result of the sudden release of the pressure of a gas above the liquid, and in the latter, it is due to the combustion of a gas above the liquid, the combustion giving rise to a compressional wave which travels down and back before being reflected at the liquid's free surface. The water shock tube is widely used in cavitation studies and both techniques are discussed herein. Fujikawa and Akamatsu[44] studied the collapse of cavitation bubbles using the direct method of this technique. The authors disposed of a sealed vertical tube composed of a lower chamber of degassed tap water and an upper part containing a gas mixture of helium and air under pressure the whole sealed by a diaphragm. Using

water electrolysis, hydrogen or oxygen bubbles were generated at the bottom of the tube using platinum electrodes before breaking the diaphragm using an electro-magnetic plunger once the bubbles of interest in the field of view. This mechanism is at the origin of an expansion (rarefaction) wave which propagates down the helium-air tube to the water column before being reflected at the bottom of the shock tube. Bubbles were then photographed by a high-speed camera during the period of growth, collapse and rebound and pressure signals recorded by means of transducers.

The combustion of a gas above a liquid also generates tension. The experimental set-up resides upon the generation of a compression wave due to the combustion above the liquid of a combustible. The wave is reflected after traveling down and back. Richards et al. [45] developed a technique in which they placed deionised water in a vertically mounted, stainless-steel, combustion-driven shock tube to study tension in the liquid. The bottom of the tube consisted of a Mylar diaphragm and the upper part of oxyacetylene equivolume mixture (used as combustible). When the latter was ignited, a detonation wave traveled down the tube and reflected at its bottom. The combination of the Mylar diaphragm and water can be almost assimilated to a free surface since their acoustic impedances are almost the same and due to the flexibility of the diaphragm.

Whilst this technique was developed to study bubble dynamics and cavitation [45], it also extended its application in process safety like for example in the work of Thomas and Oakley [46] in which the authors tried to determine in a more forward way the interaction between the type of the explosion wave (deflagration or detonation) and the water volume/containment vessel walls.

A common limitation of the technology cited above is that some specific sites promote the growth and the macroscopic appearance of vapor bubbles. These locations are called *nucleation sites* [15]. Unlike the boiling process in which the highest tensions are experienced by the liquid in contact with the heated surface, the liquid bulk experiences in cavitation a reduction in pressure making contaminants, such as small particles or micro-bubbles, a potential source for bubble nucleation sites. Harvey et al. [47] were the first to suggest the presence of micron-sized cavities on which cavities could develop explaining the difficulties in reproducing results from one laboratory to another. Nucleation sites are of three different natures. Micro-bubbles are perhaps the most readily contaminants which will grow into an observable macro-bubbles when the liquid medium is subjected to tension. Microscopic cavities can be either gas (air)- filled bubbles or vacuous (vapor-filled bubbles) and may be stabilized against gaseous diffusion by a skin of organic impurity. They are stabilized against dissolution due to surface properties. Iyengar and Richardson [48] proposed measurements based on physical means to detect

these gaseous nuclei in water. Solid particles can also act as nucleation sites. As mentioned earlier, gas can be trapped in small crevices and give rise to bubbles. These crevices can be either existing in solid particles (motes) or in the walls of the vessel containing the liquid.

1.1.3 Bubble collapse

The fundamental equation governing the dynamics of a spherical bubble was first developed by Lord Rayleigh [9] who established the first equation for the collapse of a cavity as:

$$R\ddot{R} + \frac{3}{2}\dot{R}^2 = \frac{P(R) - P(\infty)}{\rho_l}, \tag{1.2}$$

where R is the bubble's radius and P the liquid's pressure ($P(R)$ and $P(\infty)$ are respectively at the interface and in the bulk solution away from from the bubble). A dot represents a differential with respect to time. Later on, Equation 1.2 was further developed by Plesset to take into account some other terms such as surface tension (σ), dynamic viscosity (μ) and gas/vapor content of the bubble which gave place to Equation 1.3 today known as the Rayleigh-Plesset equation.

$$R\ddot{R} + \frac{3}{2}\left(\dot{R}\right)^2 = \frac{1}{\rho_l}\left[P(R) - P(\infty) - \frac{2\sigma}{R} - \frac{4\mu}{R}\dot{R}\right] \tag{1.3}$$

When a pre-existing cavity is subjected to tension, it follows three stages: *nucleation*, *growth* and *collapse*. Based on Equation 1.3, the evolution of the radius of a bubble with time can be determined for different boundary conditions and assumptions showing that a bubble passes through successive growth and collapse stages which can continue indefinitely without attenuation in the absence of dissipation mechanisms [49]. The content of the bubble also plays an important role on its behavior. In general, it is assumed that bubbles contain a certain quantity of contaminant gas at a certain partial pressure (related to their size) and temperature.

It is important to note that when bubbles collapse close to a boundary the dynamic response is more complex. The surface of the bubble suffers an involution, the collapse is asymetrical [50] and the surface away from the rigid boundary folds into the interior. This is called "jetting" and it usually occurs for bubbles close to the boundary. Visual examples are presented in the works of Lauterborn and Bolle [51] and Field [50]. This bubble elongation contributes to solid damaging but can also be interesting for surface cleaning.

During the collapse of a single bubble, its volume decreases whilst the pressure of the gas/vapor mixture inside the bubble increases. The presence of gas inside the bubble

plays an important role in the deceleration of the collapse and thus on the overall bubble dynamic response[49]. In addition to micro-jets formation and turbulence, it is also at the origin of the generation of shock waves during the rebound phase of the bubble taking place after the first collapse . If the implosion of bubbles is strong enough, high temperatures an pressures generated in their vicinity also affect the components. In an aqueous medium, vapor pressure enters the growing bubble and can thus be cleaved generating reactive species.

Bubbles' content can also be represented as a bi-phasic entity of vapor and gas. In the case of water, the first consists of water vapor while the second is formed starting from the dissolved gases in the liquid of which oxygen. Nucleation sites are at the origin of the appearance of bubbles in the medium. When they grow from an initial size of radius R_0 to many times their original size, they reach a maximum radius $R_{\max}$ before starting the *collapse* stage when the pressure is restored to its reference value. The growth of the bubbles is a combination of the expansion of the pre-existing gas/vapor and the diffusion of the vapor of the liquid (solvent and volatile solutes including gaseous compounds). In the early 1900s, Lord Rayleigh[9] discussed the consequence of the presence of a gaseous fraction in the bubble by considering that the compression of the gas is isothermal. Nowadays, it is well-established that the compression of a bubble's components is approximately adiabatic[52] when the compression velocities are high enough. According to Brennen[49], the maximum pressure and temperature generated inside a collapsing bubble are around 10^7 GPa and 4×10^4 times the ambient temperature assuming that the depression pressure is around 10 kPa, $R_{\max} = 100R_0$, the initial partial pressure of the gas in the bubble is about 0.1 MPa and that this same pressure at the beginning of the collapse is about 0.1 Pa. This result is evidently dependent of many factors, however, it gives an idea of the possible conditions generated upon the bubble's collapse.

Estimations of the bubble temperature have been widely discussed in the literature. Researchers use thermodynamic models to predict the maximal temperature generated inside the cavity by taking into consideration certain effects or simply by stating some hypotheses to simplify the problem. For example, if one neglects the heat dissipation between the bubble and its environment, the thermal conductivity of the gases and the consumed energy for the gas/vapor decomposition inside the bubble, the maximum theoretical temperature $T_{\max}$ can be estimated according to Equation 1.4[53,54] where T_0 is the temperature of the solution, P_{liq} the pressure in the liquid, γ the specific heat ratio of the gas/vapor mixture defined as $\gamma = \frac{c_p}{c_v}$ and P_v the pressure in the bubble at $R_{\max}$.

$$T_{\max} = T_0 \left[\frac{P_{\text{liq}} (\gamma - 1)}{P_v} \right] \tag{1.4}$$

Other researchers intended to use experimental techniques to determine this important parameter. For instance, Single Bubble SonoLuminescence (SBSL) is considered to be a useful probe of the extreme conditions generated during the bubble collapse. SBSL is a consequence of an acoustic excitation of a single bubble. Several studies found in the literature estimate the peak temperatures reached in SBSL in a variety of liquids[55,56]. An interesting review on the origin of this technique and the existing knowledge are presented in the work of Jarman[57]. The temperature bubble estimation, depends on several factors such as the liquid's nature and temperture, the nature of the dissolved gases[57] and the used frequencies[58]. It is important to note that light emission is not restricted to SBSL experiments, but it is also observed in flowing liquids[59].

One way to estimate the peak temperatures reached during the bubble collapse is to use the Methyl Radical Recombination (MRR) proposed by Hart et al.[60]. Bubble temperature is estimated by studying the degradation of a simple hydrocarbon, methane (CH_4) in an aqueous solution under an argon atmosphere (to suppress any large-scale oxidative side reactions) and by detecting the relative yield of the major decomposition products, i.e. ethane, acetylene and ethylene. The products are the result of the recombination of the methyl radicals $CH_3^{\bullet}$ generated by the methane decomposition in the cavitation bubble. The temperature determination method is well explained in the work of Rae et al.[61]. The authors calculate an absolute temperature ranging from 2720 to 1930 K for solutions containing respectively 10 and 100 % of CH_4. Other organic molecules were also studied[52,61] however it is admitted that the calculated temperatures reflect an average core temperature since the decomposition and recombination must take place in different temperature regions.

The consequences of bubble collapse are very interesting in chemical applications. The generated temperatures and pressures inside their vicinity are at the origin of the formation of radical species capable of reacting with chemical compounds in water. However, the mechanisms by which bubbles participate to chemical processes is not fully understood yet. Although efforts were made to understand this contribution, they were based on simplified models[62] (and included references). In their work, Hauke et al.[62] studied numerically the dynamics of isolated and ultrasound cavitating bubbles completely immersed in a liquid. The authors showed using the different models that the chemical reaction depends on several factors such as bubble contents (influencing the properties in the vicinity of the bubble), reaction rate and the production of radicals.

1.1.4 Description of existing cavitation-based techniques

Excluding laboratory techniques such as laser induced pulses[15], classical techniques to induce cavitation include ultrasound and hydrodynamic machinery. The depressurization generated in cavitation-based techniques promote bubble appearance at nucleation sites that release bubbles into the liquid's bulk. This is clearly observed with boiling water: at the initiation of boiling, bubbles are produced at specific sites and as the times passes, more and more sites are activated. Note that it is also possible to generate cavitation via laser pulses[51].

Originally, acoustics referred to the study of sound, i.e. pressure waves in air which can be detected by the human ear. It was then extended to lower and higher frequencies called infra- and ultra-sounds. Acoustic cavitation refers to the utilization of ultrasound to generate an acoustic wave in the medium. The resulting wave is composed of a succession of positive and negative half periods (see Figure 1.1) generating in the medium a succession of compression and rarefaction (tension) phases respectively. The passage of waves in the medium exerts forces on the molecules and cause them to compress and stretch around an average molecular spacing. If the wave's amplitude in the negative half-cycle is large enough, bubbles appear in the medium. This is explained by the passing wave which is able to break-down the minimum molecular distance required to hold the liquid intact. Once the pressure in the medium increases back (positive half-cycle), the bubble will shrink before it re-grows in the next half-cycle.

Ultrasonic devices use a source to generate ultrasound. For example, an ultrasonic bath uses transducers which can either work with only one frequency or with multiple ones. In general, transducers are situated at the bottom or the sides of the bath for a better homogenization of the ultrasonic power distribution. Another device is the ultrasonic probe in which the transducer is directly immersed in the container. There exists different types of probes with different shapes and of different materials and are almost all equipped with a temperature- control option. The efficiency of acoustic devices depend of several parameters such as the frequency or the acoustic power. Ultrasonic cavitation gained much attention over the years but still requires further understanding and design enhancement for a future industrial application. Gogate et al.[63] proposed an interesting paper on the scale-up design process of acoustic reactors which primary difficulty is to maintain a uniform distribution of cavitational activity. The authors attempted to provide criteria selection for operating parameters to optimize the design which they divided into operating (such as frequency and intensity of irradiation) and geometric parameters (like number and location of transducers) in addition to the liquid's nature.

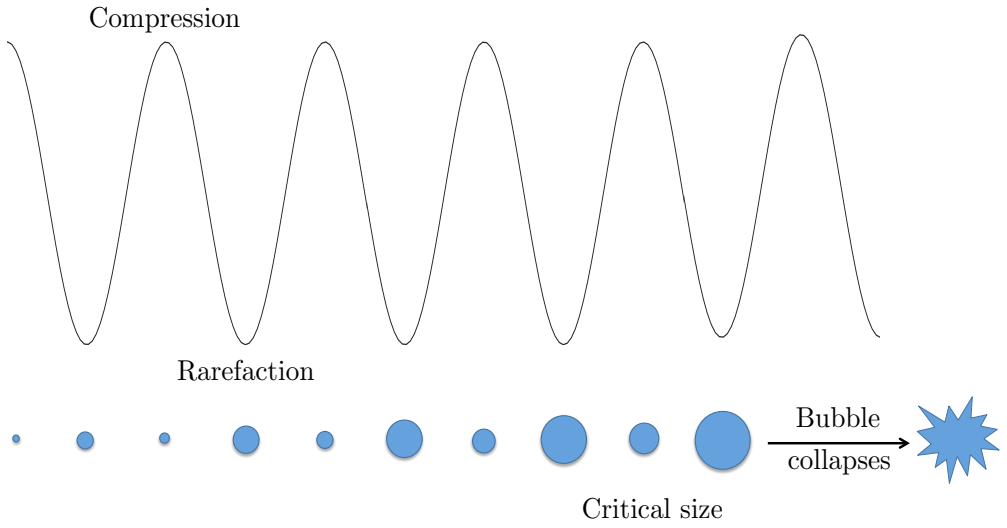

FIGURE 1.1: The response of a bubble to the passage of an acoustic wave.

Hydrodynamic cavitation techniques are based on the pioneering work of Reynolds[5] in 1894, who reported the boiling of water in an open tube at ordinary temperatures. This was the result of the pressure drop of the water passing by a converging-diverging glass tube. Bubble behavior and flow regime transitions studies based on the passage of a liquid through a constriction are detailed in literature based on simulations and/or experiments[64–66].

Accordingly, varying the velocity of a horizontal flow with a relative low viscosity subjects it to a depressurization. Venturi tubes are a common example of a device to generate hydrodynamic cavitation. The Bernoulli equation is

$$\frac{P_1}{\rho_l} + \frac{1}{2}U_1^2 = \frac{P_2}{\rho_l} + \frac{1}{2}U_2^2 + g\Delta z + E_d, \tag{1.5}$$

where E_d includes all viscous and turbulent mass energy losses, P is the pressure, U the velocity, g the acceleration due to gravity and Δz the elevation of the point above a reference plane. $\frac{P}{\rho_l} + \frac{1}{2}U^2$ is constant along a streamline such that when U increases, P decreases and bubbles appear. This phenomenon can also occur in hydraulic machinery like pumps, propellers, artificial hearts, etc. Cavitation in hydraulic systems is thoroughly studied by engineers to suppress it since it generates some mechanical erosion of exposed surfaces.

Gogate and Pandit[64] studied the effect of the operating parameters on bubble behavior and pressures generated in a plate orifice. The authors showed based on simulations that the system's response depends on the inlet pressure, the initial cavity size and the diameter of the holes. In an interesting review on hydrodynamic cavitation, the same authors[67] resumed pertinently the advantages and the disadvantages of hydrodynamic reactors of which the relative low cost of such a technology and its ease of scale-up on one hand, but lower intensity of collapse of the bubbles on the other hand especially compared to the generated pressures and temperatures with acoustic cavitation.

To compare acoustic and hydrodynamic cavitation reactors, Moholkar et al.[68] proved that identical cavitation conditions can be generated with both techniques with some advantages related to hydrodynamic cavitation. It was more energy-efficient, a simpler method and offered better operating parameter control. This result is in accordance with the study carried out by Gogate et al.[69] who compared acoustic and hydrodynamic cavitation reactors based on a model reaction with potassium iodide (KI) called the Weissler reaction.

As mentioned earlier, cavitation bubbles can appear through mechanisms different than those typically investigated in the literature, i.e. ultrasound and hydrodynamic machinery. Bubbles can be generated as a response of a liquid or solid to a sudden impact[70]. The impact submits both the liquid and the flier (in occurrence a solid) to a stress wave[50]. In solid mechanics e.g. spallation or dynamic fracture, cavitation occurs upon the impact of a solid on a target[71–73].

The first to investigate spalling was Hopkinson[74] at the beginning of the previous century. The basic principle is to impact a medium with a projectile or a flier. Following the reflection of the initial compression wave, a tensile stress wave is generated in the medium and when the local tensile strength is larger than the material's strength, small defects present in the solid structure are activated in a process similar to that of cavitation in liquids. This phenomenon appears when the pressure falls below Blake's threshold[75–80]. In this context, spallation refers to the ejection or vaporization of a material from the target in response to an impact.

In liquids, the impact of a projectile flying across a vessel full of liquid is known to induce the formation and collapse of bubbles[81]. For instance, Dear and Field[82] used the "tube arrest" method[43] to study both the collapse of a single cavity and an array of cavities contained between two transparent plates after the impact of a slider[84]. Using a water/gelatine mixture, the authors were able to control several parameters such as the shape and the size of the bubbles[70,82]. Other relevant works include those of Daily et al.[85], who studied the catastrophic rupture of glass bottles induced by the collapse of bubbles after an impact, Rodríguez-Rodríguez et al.[86] who report experiments on the

dynamic response of bubbles in supersaturated media triggered by the impact on a vessel and Dular and Coutier-Delgosha[87] who use the "tube arrest" method to investigate the thermodynamic effects associated to the collapse of a single bubble.

There exist several devices for liquid-solid impact(s)[70], the simplest case consisting of a normal impact. In a model liquid-solid impact problem the liquid is considered to have a well-defined free surface and the solid's deformation reversible during the first instants after the impact[70]. It is also assumed that the liquid is inviscid. The appearance of the bubbles depends on the speed of impact and the physico-chemical properties of the medium,

In his work, Glenn[88] used a normal impact geometry to better understand the phenomena of liquid- solid impact and studied the model of shock reflection in one-dimension. The contribution of the collapse of a cavity to the damage of solid materials was investigated in the beginning of the twentieth century by Parsons and Cook[7,70]. Few years later, Cook[7] calculated using the water- hammer theory the pressure with which a collapsing cavity can erode a propeller blade. This theory is used to describe a pressure wave propagating when a moving fluid is forced to stop. Interesting reviews dealing with its development are presented in the works of Ghidaoui et al.[89], Bergant et al.[90]. The general form of the theory is given in Equation 1.6 in which ΔP is the pressure variation, c the acoustic speed and ΔU the velocity variation.

$$\Delta P = \rho_l c \Delta U \tag{1.6}$$

According to Kornfeld and Suvorov[91], the calculation made by Cook[7] was irrelevant since it is only valid when the bubble is attached to the surface to be able to deform it. The authors also pointed out that for the damage to take place, the bubble should disappear completely resulting in a singular behavior where the pressure reached during the collapse is not well defined. Solid-liquid impact also generates surface damage[92], being well accepted that jet formation is a relevant mechanism responsible of erosion. When bubbles implode violently, high pressures and temperatures called "hot-spots" are generated in the vicinity of the bubbles, which means that using such techniques it is possible to concentrate energy in small zones and overcome processes with large activation energy (e.g. chemical reactions).

1.2 Chemical activity induced by cavitation

1.2.1 The generation of hydroxyl radicals in cavitation

As explained earlier, cavitation bubbles can, under certain conditions, be assimilated to micro-reactors and hence generate hydroxyl radicals $HO^{\bullet}$ in aqueous media. Thus, techniques based on cavitation find application in water treatment where oxidation processes need to be promoted and radical species react with the organic matter contained in the liquid.

Hydroxyl and hydrogen radicals are the result of the homolytic cleavage of a water molecule[93,94],

$$H_2O \xrightarrow{\Delta} H^{\bullet} + HO^{\bullet} \quad (1.7)$$

$$H^{\bullet} + HO^{\bullet} \longrightarrow H_2 + O \quad (1.8)$$

$$2\,HO^{\bullet} \longrightarrow H_2O + O \quad (1.9)$$

$$O + HO^{\bullet} \longrightarrow O_2 + H^{\bullet} \quad (1.10)$$

In cavitation bubbles, the water vapor molecules diffuse into the bubble interior during the growth stage and $HO^{\bullet}$ are generated during the collapse, i.e. when he temperature inside the bubble is maximal. The radical species can recombine and/or react together to form molecular O or diatomic oxygen O_2 (see Equations 1.8, 1.9 and 1.10)[53] meaning that sonolytic processes can not be strictly anoxic. Hydrogen radicals are present in a much smaller number than hydroxyl radicals[94] and therefore their presence is disregarded herein despite their ability to produce $HO^{\bullet}$ radicals[95].

There exists quantification methods for $HO^{\bullet}$ radicals and cavitational activity using hydroxyl radical dosimeters[96,97,97]. These methods allow for example to compare the efficiency of different ultrasonic reactors[98] and hydrodynamic machinery[99]. Several compounds can be used as dosimeters. Among them, iodide is a good example since the oxidation of this molecule is an indicator of the presence of an oxidizing agent. One of the advantages of this so-called Weissler reaction is related to its simple use. Indeed, the oxidation of iodide I^- into iodine I_2 or triiodide I_3^- (when I^- is in excess[98]) is obtained exclusively due to the action of $HO^{\bullet}$. In addition, intermediate products are transparent in the final result. Iodide remains as a standard dosimeter for sonochemical

reactions[100,101] and the proposed reaction mechanism is as follows[102]:

$$\begin{aligned} I^- + HO^\bullet &\longrightarrow HO^- + I^\bullet \\ I^\bullet + I^- &\longleftrightarrow I_2{}^{\bullet-} \\ 2\,I_2{}^{\bullet-} &\longrightarrow I_2 + 2\,I^- \\ I_2 + I^- &\longleftrightarrow I_3{}^- \end{aligned} \tag{1.11}$$

Note that the hydroxyl radical in Equation 1.11 comes from water molecule dissociation (see Equation 1.7). Triiodide formation is easily monitored spectrophotometrically at a wavelength equal to 355 nm[98]. It colors aqueous solutions from light yellow to dark brown as a function of its increasing concentration in the medium. Furthermore, in the presence of starch, it confers a blue/black color to the solution thus making it easily to see. It is noteworthy that the most important parameter governing the efficiency of the radical generation is probably the intensity with which the bubbles collapse. This is the same mechanism governing the resulting noise and damage in pumps. Hence, the more intense the collapse is, the higher the radical population should be.

The application of ultrasound to chemical reactions was first observed in the 1950s. Table 1.1 lists some examples of the different reactions types and applications of cavitation studied in literature. This non-exhaustive list shows the increasing interest in the field of applying cavitation-based techniques to different domains. Since cavitation bubbles can be at the origin of the generation of hydroxyl radicals, cavitation-based-techniques are employed in waste water treatments[103,104]. However, the combination of cavitation and chemical reactions is very complex and further understanding of the occurring mechanisms is necessary.

Luche et al.[105] differentiated in their work between true and false sonochemistry. The first resulting from the action of free radicals attack whilst the second resulting from mechanical effects around the bubble. Therefore, based on the differentiation made by the author, the high temperatures generated in the bubble vicinity are at the origin of the chemical reactions[106]. However, the mechanism by which the organic molecules are destroyed is very complex and the nature of the molecule influences the mechanism. To better understand the place of occurrence of oxidation reactions, different scenarii can be imagined and either be taken separately or combined: the reaction can take place within the bubble, at the bubble/solution interface or in the bulk solution[104] (assuming that they are capable of *escaping* the bubble's interior). This proves the complexity of the mechanism by which organic molecules are destroyed. It is shown in acoustic cavitation that hydrophobic and/or volatile chemicals tend to diffuse into the bubble's vicinity whilst hydrophilic and/or non-volatile compounds tend to remain in the bulk liquid.

Therefore, the place in which the reaction takes place is different. Hydrophobic and/or volatile molecules are most readily destroyed at the bubble-liquid interface and/or inside the bubble. Hydrophilic and/or non-volatile compounds react in the liquid medium and/or the bubble-liquid interface depending on their concentration [107].

Molecule	Application/Reaction	Cavitation type	Reference
Waste and fresh cooking oil	Transesterification	Hydrodynamic	[108]
Phenol and bisphenol A	Oxidation	Ultrasound	[109]
Antistreptavidin IgG1 and rhGH	Protein aggregation	Mechanical shock	[110]
Invasive weeds	Enzymatic hydrolysis	Ultrasound	[111]

TABLE 1.1: A list of some reactions and applications of cavitation in literature.

The radical attack mechanism and the interaction at the bubble's interface is investigated first. The $HO^{\bullet}$ radicals are thought to be responsible of much of the occurring chemistry. By studying the sonolysis of tert-butyl alcohol in an aqueous medium, Tauber et al. [52] claim that the concentration of the hydroxyl radicals was high at the interface of the bubbles (estimated to $10^{-2}\,\mathrm{mol}\cdot\mathrm{L}^{-1}$) and that a great number recombines to form hydrogen peroxide (H_2O_2) according to:

$$2\,HO^{\bullet} \longrightarrow H_2O_2. \tag{1.12}$$

If scavenger molecules are present at the gas-liquid interface, part of the $HO\cdot$ radicals react with them and H_2O_2 concentration decreases compared to when the scavenger molecules are absent. To highlight the presence of H_2O_2, Henglein [53] showed that the H_2O_2 yield is decreased in the presence of $HO^{\bullet}$ scavengers such as acetic acid, dioxane and 1-hexanol (see Figure 1.2). The author correlated the concentration of the molecules to the hydrophobicity ratio R defined as the ratio between the hydrophobic to the hydrophilic groups in the molecule. For example, four hydrophobic groups (CH_2) and two hydrophilic groups (O) are present in a dioxane molecule thus $R_{\mathrm{dioxane}} = 2$. Following the same reasoning, $R_{\mathrm{acetic\ acid}} = 1$ and $R_{1-\mathrm{hexanol}} = 6$.

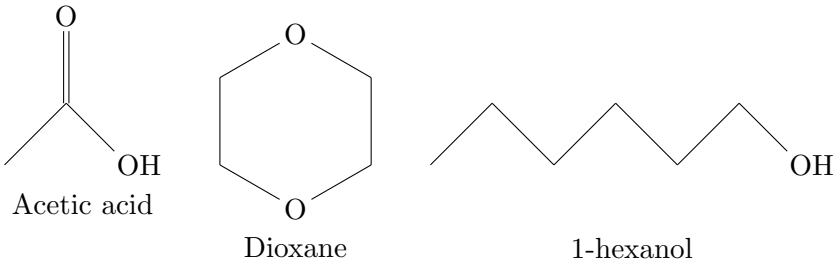

FIGURE 1.2: The structural formula of some $HO^{\bullet}$scavengers.

The results showed that the higher R is, i.e. the more hydrophobic the molecule, the more the molecules will tend to accumulate at the bubble/liquid interface. Hence, the concentration of the molecule will decrease since the scavengers will react more rapidly with the radicals and prevent their recombination into H_2O_2. The scavenging efficiency is dependent on the scavenger and its scavenging power. In this way, the author highlighted the formation of hydrogen peroxide at the bubble's interface but it is important to note that part of the H_2O_2 is also being destroyed by $HO^\bullet$ radicals[52]. The molecule's physico-chemical properties are one of the many parameters which influence the occurrence of the chemical reaction. For example, considering the volatility of the organic molecules, volatile/hydrophobic compounds diffuse into the bubble whereas non-volatile/hydrophilic molecules stay in the bulk solution[112,113].

When we are able to generate a repetitive transient[b] bubble, the majority of the produced radicals are imprisoned in the bubble interior by the bubble surface[114]. Soluble products from the bubble can still diffuse into the solution bulk[115]. The lifetimes of bubbles and radicals are a key parameter for a better understanding. As mentioned earlier, radical species are generated inside the bubble because of the high temperatures induced by bubble collapse. If the lifetime of the bubbles is smaller than that of the radicals, then these latter are released into the bulk solution following the former's fragmentation or by their dissolution. In the opposite case, the radicals are trapped inside the bubble and will have time to recombine and give H_2O_2 molecules (see Equation 1.12). Since the bubbles lifetimes depend on the acoustic frequency, this parameter is of great importance in sonochemistry.

1.2.2 Examples based on existing techniques

Kidak and Ince[113] studied the effect of operating parameters on the removal of phenol molecules using ultrasound. They showed that at a frequency equal to 20 kHz, the treatment was ineffective. The authors explained that by referring to the volatility of the molecule. Since phenol is a low volatile molecule (see section 1.3.1), it will preferably stay in the bulk solution or at the bubble's interface[116,117]. In addition, at frequencies between 20 and 100 kHz, the lifetime of the bubbles is long and since the generated radicals are formed in regions of high temperatures[118], they will stay *trapped* inside the bubble and therefore inaccessible to the organic molecule. However, higher frequencies seem more suitable for phenol degradation. Indeed, they tested two higher frequencies of 300 and 520 kHz, with the optimum found at 300 kHz. In fact, even though the increase in frequency generates a higher concentration of free radicals[119], it also decreases the

[b] Qualifies a bubble undergoing a high-energy phenomenon which will cause its instability and later violent collapse[49].

collapse's intensity[120]. Note that this phenomenon is observed for a given acoustic power.

The pressure amplitude is a key parameter in the sonochemical systems that is usually related to the power transferred to the medium. It influences to a certain extent the number of cavitation bubbles, the temperature of collapse and the reaction yield[120,121]. When operating at low pressure amplitudes, limited active cavitation is observed because bubbles undergo low and stable energy oscillation[122]. Therefore, to obtain transient or non-linear response, i.e. bubbles which will eventually collapse violently and give rise to free radicals, high pressure amplitudes must be transferred to the liquid.

In systems resorting to acoustic cavitation, it should be kept in mind that the frequency and the acoustic power are related though the vessel resonance properties, that at the same time depend on the amount of bubbles present in the system. As a general rule, the number and size of cavitating bubbles increases with increased frequency and the number of active bubbles depends strongly on the acoustic power. The main question arises when it comes to the attribution of the efficiency of water treatments in the presence of cavitation bubbles to radical species. Indeed, the oxidation of the contaminants can occur following another reactional mechanism based on the direct pyrolysis of the organic matter[53,123]. According to Henglein[53], the action of the ultrasounds is not only restricted to the generation of $HO^{\bullet}$ radicals. The organic molecules are also subjected to a direct thermal action in the presence of acoustic waves[52,53] in regions of high temperature.

When sodium acetate is subjected to sonolysis under an argon atmosphere, the author observed the formation of "unusual" products. The formation of a single product, succinic acid (when subjected to γ-radiolysis) is the reason behind the utilization of this organic compound. The presence of this molecule, also detected in sonolysis, with other products such as carbon monoxide (CO) and methane (CH_4) can not be explained by a radical attack[53]. They are the result of the thermal decomposition of the parent molecule in regions of very high temperatures which the author qualified as "*interfacial regions*".

The work of Nagata et al.[124] shows a significant decrease in the degradation rate of chlorophenols in the presence of *tert*-butanol, a good $HO^{\bullet}$ radicals scavenger[52,53,125]. Thus, the authors demonstrated that the main degradation pathway is via the radical attack[103,126]. As for the study by Kang and Hoffmann[123] concerning the oxidation of MTBE (methyl *tert*-butyl ether) in the presence of ozone, it shows that the reaction pathway followed three routes. These different examples show the complexity of the sonolysis systems and the underlying mechanisms.

Despite their interest, cavitaion-based techniques are costly. For example, cavitation in itself is not sufficient to achieve high destructive rates of industrial waste pollutants [127]. Accordingly, researchers combined this method to other available AOPs like oxidation using hydrogen peroxide.

In the field of water treatment, the use of two agents is typically adopted since it generates a more intense cleaning action. Indeed, water alone is a poor cleaner, and soap is not a cleaner at all. However, the combination of these two provides an efficacious cleaning. On this basis, the efficiency of a water treatment process depends on the speed of the generation of the oxidizing species, i.e. the free radicals and the duration of contact between these radicals and the polluting molecules. Thus, the optimization of the process becomes a major challenge. The similarity between the mechanisms of AOPs for the destruction of contaminants and the difficulties to find the optimal operating conditions make their combination interesting and challenging. Previous research showed that the synergy between cavitation and AOPs improves the overall process performance compared to the individual techniques or their simultaneous use [128]. However, under certain circumstances, the combination effects may not be additive or even antagonistic.

By combining different techniques, some of the problems experienced with one or the other method are surpassed. Taking as an example the photocatalytic oxidation, the difficulties of mass transfer and solid fouling can be overcomed by coupling the technique to ultrasonic irradiation [129]. In fact, not only the quantity of $HO^{\bullet}$ radicals increases significantly in the medium due to cavitation, but also the generated turbulence by the ultrasonic irradiation makes it possible to remedy the problem of mass transfer and facilitates the regeneration of the catalyst. Many possibilities exist when it comes to combining some oxidants to cavitation - especially ultrasound - of which ultrasound-s/H_2O_2 stands out.

Lim et al. [109] tested the effect of the H_2O_2 concentrations on the enhancement of the sonochemical degradation of two organic molecules, phenol and bis-phenol A (BPA) of initial concentration equal to 0.044 mmol in a 1 L reactor. The ultrasonic reactor consisted of a 10 cm cup-horn single piezoelectric transducer operating at 35 kHz. The authors showed that in the absence of hydrogen peroxide and only under the cavitational effect, BPA was more readily degraded than phenol. They explained the observed results by referring to the chemical properties of the molecules. Since BPA is more hydrophobic and volatile than phenol, it has a higher probability of entering the bubble and be degraded by the free radicals whereas phenol will preferably stay in the solution. In the presence of the H_2O_2/ultrsaounds system, the addition of the oxidant had little effect on the degradation of BPA whilst it had a significant effect for the phenol degradation. Due to its chemical properties, H_2O_2 stays in the solution with phenol and therefore

react together. Remarkably, the increase of the hydrogen peroxide concentration had little effect on the efficiency of the reaction. It must be noted that the influence of H_2O_2 depends on the compounds[128] and that its role as a $HO^{\bullet}$ scavenger makes the determination of its optimal concentration delicate.

Although an intense research is done on the combination of water treatment and ultrasounds, fewer work exists on the oxidation of recalcitrant molecules and other types of cavitation-based techniques such as solid-liquid impact induced cavitation[130]. Given the potential of cleaning to induce high intensity cavitation in solid-liquid impact techniques, it is interesting to explore these technologies for the degradation of pollutants.

1.3 Waste water treatment

In France, industries (paper and food industries particularly) account for half of all organic pollutants released into the natural environment, with the remaining 50 % coming from local authorities. Moreover, the industries are still responsible for a large proportion of toxic waste in water despite the efforts made in recent years to reduce the quantities of the discharged pollutants and to monitor them. Indeed, they are restrained to reduce the contamination to an acceptable level by using different techniques.

In 2002, the French Ministry of the Environment implemented over a period of 4 years a national action for the detection and reduction of the Release of Dangerous Substances in Water by classified installations (RDSW). As per that Ministry, "*any industrial or agricultural operation likely to create risks or cause pollution or nuisance, notably in terms of local residents health and safety, is a classified installation*". Between 2002 and 2007, the campaign analyzed the discharges of 180 industrial plants and urban waste water treatment plants in the Provence-Alpes-Côte d'Azur region. This operation included a phase of research of substances likely to be present in the discharge (by activity sector), called initial monitoring followed by a phase of consolidation of the perennial monitoring of substances emitted. Finally, a phase of proposal strengthened by a technical and economical analysis or an action plan[131] was proposed. Among other things, this study made it possible to say that the paper industry is the most polluting sector in the industrial sectors and that the food industry has increased its discharges by 80 % due to its development.

1.3.1 Usual contaminants: the case of phenol

The organic matter, present under dissolved or solid forms, contributes to the reduction of dissolved oxygen in aquatic environments leading to the asphyxiation of living

organisms. This organic matter is composed of carbon atoms associated with other elements such as hydrogen, oxygen and nitrogen mainly. Waste water can contain various pollutants ranging from pathogenic microorganisms to numerous chemical substances presenting risks to human health and the environment. As a result, waste waters must be collected and treated before releasing them into the natural environment.

The criteria for assessing the quality of industrial effluents play an important role in finding the appropriate treatment to reduce pollutants' concentration in industrial discharges. The quality of the effluents is judged according to different criteria[132] such as the Chemical Oxygen Demand (COD)[c], the Biochemical Oxygen Demand (BOD)[d] and the Total Organic Carbon (TOC)[e].

Phenol is an organic molecule widely studied in literature and present in industrial discharges. Discovered in 1650 by Johann Rudolf , it is mainly found in the waste waters coming from coal processing plants, petroleum refineries, paper industries, paint, textile, pesticide, pharmaceutical and tannery manufacturing plants. Phenol has a simple molecular structure (see Figure 1.3).

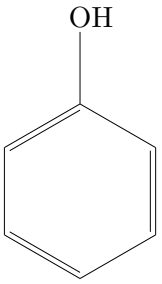

FIGURE 1.3: Structural formula of a phenol molecule.

More generally, the term "phenol" includes a group of substituted hydroxylated molecules derived from benzene (simple phenols) and its higher homologues (cresols known as methylphenol) and polycondensed nuclei molecules (sulphonated naphthols and naphthols). Phenol has a a wide range of applications from synthetic resins (bisphenol A, etc.) to dyes (diazo compounds, etc.), food additives (vanillin, etc.), medicines (aspirin, paracetamol, etc.), herbicides (chlorophenols, etc.), etc. When reacting with acetone and in the presence of an acid catalyst, phenol can be converted to bisphenol A (see Figure 1.4), a monomer for the manufacture of plastic (bisphenol A polycarbonates).

[c] In mg/L. COD is the equivalent amount of oxygen required to oxidize organic matter (bio and non-biodegradable substances) present in a water sample by means of a strong chemical oxidizing agent.

[d] In mg/L. BOD corresponds to the quantity of oxygen required by bacteria for the degradation of organic matter. Not all organic matter is oxidized in BOD analysis, only bio-degradable ones. This criterion is defined as BOD_5 when evaluated over 5 days and depends, among other things, on the microorganisms used for the biodegradation.

[e] In mg/L. TOC represents the totality of carbon present in the organic matter dissolved and/or suspended in aqueous media.

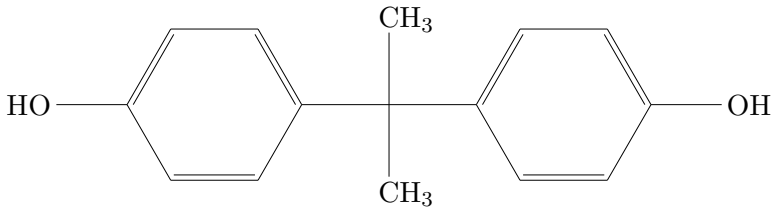

FIGURE 1.4: The structural formula of a Bisphenol A molecule.

Phenol is not classified as an alcohol due to its unique properties. Indeed, in an alcohol, the hydroxyl group −OH is bonded to a saturated carbon atom, whereas in the phenol molecule, this group is linked to a non- saturated aromatic structure (alternating simple and double bonds). Thus, phenols acquire a higher acidity than alcohols. The pKa value of the phenol/phenolate pair is equal to9.9 at 25 °C. Phenol is also a low-volatile compound with vapor pressure equal to 0.41 mmHg at 25 °C.

Even though the phenol present in the environment can be extracted from tar or waste water from cracking units, it is mostly produced synthetically. Phenol world production was estimated around 6 Mt/yr in 2008[133] and it remains one of the major products of the organic chemical industry even though its use has somewhat been replaced by new plastic material. Its role as an intermediate has also been reduced by using cyclohexane and its derivatives.

The main disadvantage of phenol molecule is that to destroy it, very high temperatures and oxidizing agents are necessary. The organic molecule reacts strongly with strong oxidizers such as peroxides. Around 800 °C, the phenol molecule is reduced to benzene in the presence of zinc. At higher temperatures, pure phenol decomposes entirely into carbon monoxide, carbon and hydrogen[134]. For its uneasy to destroy this refractory molecule, phenol has become one of the model molecules studied in waste water treatments.

1.3.2 Waste water treatment techniques for phenol and its derivatives

One of the aims of waste water treatment is to remove pollutants which can harm the aquatic environment. The presence of dissolved oxygen (DO) is very important for aquatic life and when the concentration is low it has deleterious effects on the aquatic environment. Therefore, waste water engineers focus on the removal of pollutants which cause the depletion of DO such as phenol.

Due to the toxicity and biodegradability problems related to phenol and its derivatives, these molecules represent a real problem for polluted waters. Indeed, they are harmful at low concentrations for the organisms and they are dangerous pollutants because of

their potential harmful effects on human health[135–137]. Consequently, a well adapted treatment must be set in place to eliminate them.

The choice of the optimal water treatment method depends on several factors such as the constituents (organic or inorganic), their concentrations and toxicities, the volume to be treated, etc.[138,139]. From a general point of view, there are two types of water treatment which can be used to classify the methods concerning phenol removal: the first is based on the pollutant's recovery whilst the second directly aims at destroying it. To recover the organic molecule from waste waters, physical techniques are set in place such as adsorption[137,138,140–142], membrane-based separations like pervaporation[142–144], ultrafiltration[145] and liquid membrane extraction[142,146–148]. As for the destructive methods, the most commonly used are the incineration as well as biological treatments[149] and chemical oxidation reactions[150,151]. These latter include Wet Air Oxidation (WAO) and Advanced Oxidation Processes (AOPs) of which we cite photolocatalytic reactions[126], Fenton reaction[152,153] and cavitation[127].

1.3.2.1 Toxicity, eco-toxicity and other properties

Anyone can be exposed to phenol through the environment, the consumption of contaminated water or food, and the use of phenol-containing products[154]. When an effluent is released into the environment without prior treatment, it causes severe damage by contamination of the soil, surface and water. Some laws have been therefore set in place to regulate the phenol content of waste waters.

Phenol is an irritating and highly corrosive substance. It has a strong ability to penetrate the body through the skin and mucous membranes. The European Union has classified phenol as category III mutagen and the majority of phenols and their derivatives are toxic. This makes them hazardous waste and some are known to be carcinogenic. The "Agency for Toxic Substances and Disease Registry" has listed phenol on the "Priority List of Hazardous Substances"[155]. If absorbed, phenol is rapidly distributed in the body[134]. The concentrated application of phenol on the skin can cause severe skin lesion[156] and cases of fatal poisoning[157] have been registered. In the case of infants, the ingestion of minimal amounts of phenol (5 to 500 mg) whether accidental or intentional is fatal. As for adults, cases of death occur after ingesting 1 to 32 g[158,159].

A significant amount can enter the skin when the body is in contact with phenol vapors. Due to their toxicity, the limit value of the concentration in air is fixed at $0.0002\,\mathrm{mg}\cdot\mathrm{L}^{-1}$ in France[160]. These molecules are transformed into other chemicals called metabolites which are rapidly eliminated within a few days a priori in the urine. As for inhalation, the majority of phenol rapidly enters the body through the lungs and gives signs of

respiratory irritation with cough and dyspnea. During exposure by inhalation of a human being to phenol vapors at concentrations of 6 to 20 $mg \cdot m^{-3}$, 60 to 80 % of phenol is absorbed [134] causing various effects from intense thirst to nausea and in some cases a coma [160]. Livers and kidneys of animals exposed to phenol in the air can undergo, among other things, pneumonia and morphological alterations [161].

Phenols are also soluble in water and can therefore reach drinking water sources where they can generate unpleasant odors and tastes even at low concentrations [140,162]. Accordingly, they are toxic and very dangerous for aquatic life [136]. They can modify the aquatic ecosystems and cause damage to the biota [135,137]. According to literature, bioaccumulation of 2 $mg \cdot L^{-1}$ or more of phenol alters the development of certain fish and the disappearance of the aquatic life is reached for concentrations ranging between 10 and 100 $mg \cdot L^{-1}$ within 96 h [137,162].

The "United States Environmental Protection Agency" recommends a maximum limit of 0.001 $mg \cdot L^{-1}$ [163]. The general limit for the discharge of phenol effluents is 0.05 $mg \cdot L^{-1}$, before being discharged into watercourses [163]. The "World Health Organization" limited the concentration of phenol in drinking water to 0.001 $mg \cdot L^{-1}$ [158]. The European Union Directive 80/778 /EC requires a total phenol concentration of less than 0.0005 $mg \cdot L^{-1}$ in drinking water [164] whereas in France, it must be less than or equal to 0.1 $mg \cdot L^{-1}$ [165] (phenol index)[f].

The tolerated amounts of phenol in water is very low which drives researchers and industrials to find divers means to reduce its presence in waters. As mentioned earlier, phenol can either be extracted from these waters or destroyed.

1.3.2.2 Non-destructive techniques

Physical treatments are used to separate pollutants from their matrices. Non-destructive methods use an extraction-based technique relying on the chemical or physical properties and result in a selective separation of one or more compounds from a mixture. Due to the formation of toxic by-products such as chlorinated phenols, physico-chemical methods become sometimes very costly and present intrinsic disadvantages [158]. For example, distillation require the use of organic solvents which in some cases are more contaminating than the starting pollutant itself with a limited effectiveness thus making the process very expensive. Nevertheless, techniques such as adsorption, liquid-liquid extraction and membrane-based processes (the latter not detailed herein) do not alter the nature of the species.

[f] Method of detection including all phenols reacting with amino-4-antipyrine and para-nitraniline.

Adsorption Adsorption is a useful technique for eliminating deleterious micropollutants. It is highly used for the treatment of drinking water from underground or surface sources. During adsorption, the interactions between gas or liquid molecules (adsorbates) and a solid surface (adsorbents) take place. These interactions fix the adsorbate to the solid surface. There exists various types of adsorbents used in literature[166] such as eco-friendly polymeric adsorbents[167].

Activated carbon is the primary adsorbent in water industry thanks to its physicochemical properties which make it a good adsorbent to organic molecules[168]. It has a large surface area, a good pore size distribution and a high mechanical strength[169]. Activated carbon precursors are mainly coal and lignocellulosic-based waste biomass such as coconut shell and wood[163,170–175]. The raw material can be used directly however activation enhances the absorbance performance. The physical activation implies that the carbon medium, once prepared from precursors, is subjected to stream (a gas like water, argon or nitrogen) and high temperature (800 to 1000 °C) usually in an oxygen-free environment. As for the chemical activation, it requires the need of chemical species such as zinc chloride or potassium hydroxide[173]. As a result, during its preparation, the pyrolysis conditions and the activation procedure influence the final product characteristics and therefore its activity[168,176].

It is noteworthy that activated carbon is inefficient in treating large amounts of phenol[177–180]. In addition, it is very costly: the price range per kilogram varies from 2–4 dollars to 20–22 dollars depending on its quality[166]. This makes it difficult to use when waster waters contain high concentrations of organic matter[177–180]. Efforts have been made to find more economical natural adsorbents and clays proved to be an interesting alternative[181].

Liquid-Liquid Extraction Another non-destructive technique is the liquid-liquid extraction (LLE) which allows the separation and purification of chemical compoundsCote[182]. Unlike distillation which is based on boiling point differences, LLE is based on the separation of compounds (solutes) based on their relative solubility in two immiscible liquids (and of different densities), generally water (aqueous phase, carrier) and polar organic solvents (organic phase, solvent). This separation method implies a mass transfer through the two liquid phases. One important operating parameter is the solvent's choice judged according to its capacity to transfer efficiently the solute from the carrier to the solvent. In general, an ideal solvent has certain properties of which a high solubility for the solute, a low solubility for the carrier liquid and a low cost. This technique is used primarily for highly loaded effluents[183] (phenol concentration greater than $1000\,\mathrm{mg}\cdot\mathrm{L}^{-1}$ [164,184]), which results in a big advantage over other technologies. Kiezyk

and Mackay[185] propose an interesting review on the waste water treatment based on solvent extraction. The author discussed the economical aspect of this technique and its application potential. Hence, LLE is a useful technique when it comes to the phenol recovery[164,184,186] becoming profitable when phenol concentration is greater than $10\,000\,\mathrm{mg}\cdot\mathrm{L}^{-1}$[184].

1.3.2.3 Destructive techniques

Incineration Incineration was the first water treatment technique to be marketed. It refers to the combustion of the sewage sludge produced in waste water treatment plants. The energy produced by the combustion can be either used directly by the plant or sold since the sludge contains 10 times the energy needed to treat it[187]. The combustion takes place in specific furnaces, the pollutants being in the gaseous state and the furnace at temperatures exceeding 850 °C[188].

This technique is only advantageous when it becomes self-sufficient in energy. In other words, when the water to be treated is loaded with more than $30\,\mathrm{g}\cdot\mathrm{L}^{-1}$ of COD, i.e. highly polluted effluents[189] able to sustain self-combustion. Several types of incinerators exist in the industry however, this method is expensive due to the high costs of installation and operation (high working temperatures)[188]. Its main disadvantage is that it converts the waste into ash, solid waste and toxic fumes containing among others CO_2, NOx, SOx, furans and dioxins. Garrido-Baserba et al.[187] proposed a study of sludge treatment alternatives including incineration whilst taking into account the economical and environmental aspects of each technique. Their conclusion is that thermal treatments (such as incineration) are the worst option for all scenarios.
The use of incineration is divisive. Supporting arguments by the industry regarding this technique include: fine particles are removed by processing them through filters and scrubbers, the produced energy can be utilized and replace power generation plants, the emission of furans and dioxins is controlled. However, environmental activists still oppose to it given that heavy metals are produced along the way and additional treatment is sometimes required when injurious matter is present at the end of the operation.

Biological treatment Biological treatment necessitates the use of microorganisms of animal or vegetable origin for the destruction of oxygen-demanding pollutants. They are mostly organic pollutants and also ammonia, which is an important inorganic pollutant. Aquatic microorganisms eliminate biodegradable organic materials which serve them as nutrients and their particularity is that they are capable of surviving lower DO levels than higher life forms.

This technique can be classified according to two major types of operation[190,191]. The first consists on the degradation of organic residues in the presence of dioxygen (aerobic degradation), forming initially catechol (see Figure 1.5) which can be further degraded releasing carbon dioxide. The second takes place in its absence (anaerobic degradation) leading to fermentation and releasing carbon dioxide and methane[192]. Each of these alternatives has its advantages and disadvantages as described in the work of Chan et al.[191].

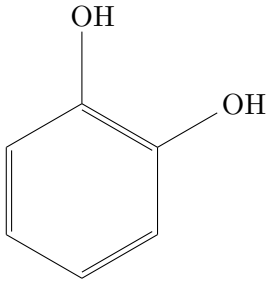

FIGURE 1.5: The structural formula of a catechol molecule.

Several species of bacteria are known to degrade the phenol molecule like *Alcaligenes*, *Acromobacter* and *Pseudomonas Putida* in addition to certain mushrooms such as *Fusarium* and *Penicillium* species[193]. Bio-processing is a long process requiring the control of various parameters such as pH, temperature, oxygen concentration, etc. In addition, the treatment of solutions containing high concentrations of contaminants and organic loads remains problematic[149]. Phenol has phyto-toxic effects on active microorganisms[194] making it difficult to these organisms to degrade solutions at concentrations greater than $200\,\mathrm{mg}\cdot\mathrm{L}^{-1}$[144]. Indeed, the toxicity of phenol may cause the inhibition of the degradation processes: a lack of growth of microorganisms is rapidly established in effluents with high concentrations of phenol[195]. Nevertheless, the use of a sequential biological reactor (SBR) was suitable for the treatment of phenolic solutions with moderate concentrations[149,196,197].

Oxidation reactions Liquid-phase oxidation offers a real solution for the treatment of effluents which are toxic and difficult to treat. Chemical oxidation aims to mineralize the contaminants to carbon dioxide, water and inorganics or at least transform them into harmless products. Much research has been done over the past decade concerning two types of processes based on the type of oxidant used: Wet Air Oxidation (WAO) processes involving dioxygen (O_2) and Advanced Oxidation Processes (AOPs) in which oxidizing agents like ozone (O_3), hydrogen peroxide (H_2O_2) and species activated by particular means (such as radiation) are employed. These techniques have evolved rapidly and belong to the latest generation of technologies developed to treat water.

WAO is a process used in water treatment to degrade the contaminants (organic or inorganic, in an aqueous solution or in suspension) using molecular oxygen (direct use or from air) as the oxidizing agent. The oxidizing potential of O_2 is equal to 1.2 eV. WAO is able to treat waste waters which are too concentrated to be biologically treated and too dilute for incineration. Its principle relies on the enhancement of the contact between these molecules.

First developped by Zimmermann[198], its industrial application gave rise to the Zimpro and Kenox processes. The operating conditions consist of high pressures and temperatures with or without the presence of a catalyst, all of which favor the solubility of oxygen in water. Since the oxidation takes place in the liquid phase, and the working temperature range is between 150 to 320 °C, the medium must be pressurized (2 to 15 MPa)[199–202] to keep a sufficient quantity of water in the liquid state, the water also being a moderator for its heat transfer capacity. Hence, the solubility of oxygen at high temperatures influences the oxidation force of the system which in turn increases the rate of the reaction and the production of free radicals involved in the formation of intermediate products.

Previous research showed that like most other techniques, the oxidation degree of the effluents depends on different factors like the temperature, oxygen or air pressure, reaction time and finally the medium's oxidability. As a result, in the case of a complete degradation, carbon, nitrogen, halogens and sulfur are respectively converted into carbon dioxide, dinitrogen, halides and inorganic sulphate[202]. In some cases, WAO can be used as a pre-treatment like before the biological treatment for the purpose of partial oxidation. However, this implies that the remaining products in solution are non-toxic and biodegradable.

WAO remains an efficient water treatment technology[200]. Unfortunately, it is limited on an industrial aspect for its necessary to operate at certain conditions requiring high costs. To remedy to these constraints, other treatment techniques have been developed, called Advanced Oxidation Processes which require milder operating conditions and an easier industrial scale-up.

1.3.2.4 Advanced Oxidation Processes

In the 1980s, Advanced Oxidation Processes (AOPs) were set in place for the treatment of drinking water before being utilized later on for waste waters treatment. This technology relies on the generation of highly oxidizing radical species such as hydroxide ($HO^{\bullet}$) in sufficient quantities to eliminate a majority of pollutants (organic and inorganic) or as a pre-treatment to biological processes. Later on, the concept was extended

to other radical species such as sulfate radicals $SO_4^{\bullet -}$ which gained attention as a powerful oxidizing agent. Indeed, radicals are very reactive species which can readily degrade recalcitrant organic molecules and sometimes inorganic pollutants.

Different AOPs are implemented in the industry and developed in research. It is important to note that the efficiency of the process depends on several parameters such as the contaminants physico-chemical properties, the operating conditions and the AOP type. To generate $HO^{\bullet}$ radicals, AOPs make use of several oxidants like hydrogen peroxide (H_2O_2) and ozone (O_3) which are relatively expensive oxidants. Thus, this treatment procedure is economically viable when the contaminated waters are poorly polluted, i.e. COD contents $\leq 5\,g \cdot L^{-1}$ [203]. The efficiency of the oxidation process mainly relies on the chemical agent and its oxidizing power. A more powerful oxidant results in a better oxidation reaction. There exists various oxidants which can be classified as a function of their oxidation potential:

$$HO^{\bullet}\ (2.8\,eV) > O_3\ (2.1\,eV) > H_2O_2\ (1.8\,eV) > O_2\ (1.2\,eV).$$

As this classification shows, all oxidants are stronger oxidizing agents than O_2 and the hydroxyl radical $HO^{\bullet}$ is the specie having the highest oxidizing power making it the most sought-after oxidant for the degradation of pollutants. $HO^{\bullet}$ radicals have the virtue of being non-selective and react very rapidly with various species with a rate constant of the order of 10^6 to $10^9\,L \cdot mol^{-1} \cdot s^{-1}$ [139,204,205]. Having very short lifetimes, hydroxyl radicals are produced *in situ* starting from other oxidizing agents (like O_3 or H_2O_2) sometimes in the presence of transition metal ions (like Fe^{2+}) or in the presence of irradiations (like ultraviolet light or ultrasounds) [188]. AOPs based on the combination of these latter also exist (H_2O_2/Fe^{2+} (Fenton), H_2O_2/ Fe^{3+} (Fenton-like), H_2O_2/Fe^{2+}, O_3/UV, etc.). Several processes will be briefly discussed hereafter. For more details the reader is referred to the work of Huang et al. [188].

Oxidation using ozone Ozone, a water-soluble gas, arose interest for drinking water treatment when the use of chlorine as both a disinfectant and oxidizing agent had to be abandoned since free chlorine generates by-products such as trihalomethanes, harmful to human health. Ozone first proved to be a promising oxidizing agent in the drinking water treatment field in 1906 at the Bon Voyage plant in Nice, France. Because it is an unstable gas, it must be generated *in situ* starting from O_2 (directly or in air) in the presence of plasma (corona discharge) which is the most common technique following a

two-step formation:

$$\begin{aligned} O_2 &\xrightarrow{\text{corona discharge}} O^\bullet + O^\bullet \\ O^\bullet + O_2 &\longrightarrow O_3 \end{aligned}$$

O_3 can also be generated photochemically using ultraviolet light ($\lambda \sim 185\,\text{nm}$) resulting from arc discharge lamps. In the presence of UV light ($h\nu$), hydrogen peroxide (H_2O_2) is furtherly formed thus increasing the oxidizing power of the system according to:

$$O_3 + H_2O \xrightarrow{h\nu} H_2O_2 + O_2$$

Once generated, O_3 must be transferred to the waste water, the most used technique being the counter- current sparged column. Once it is dissolved in the waste water it reacts with the contaminants; the faster the reaction is, the more O_3 will be dissolved and the more rapidly it will cross the water/gas boundary. Different pathways have been proposed, the overall mechanism generating hydroxyl radical $HO^\bullet$ from O_3 being as follows[204]:

$$3\,O_3 + H_2O \longrightarrow 2\,HO^\bullet + 4\,O_2$$

The action of ozone on the cleavage of the unsaturated molecules like phenol is highly effective however, ozone's reactivity towards aliphatic halides and neutral compounds is very low[188,205,206]. Turhan and Uzman[206] studied the removal of phenol from water in the presence of ozone. The authors used a mechanically stirred semi-batch reactor supplied with a counter-current of ozone. They showed that the reaction was extremely selective and limited to unsaturated aromatics and aliphatic compounds. Indeed, they observed the formation of catechol (see Figure 1.5) and hydroquinone (see Figure 1.6) during the first reaction stages, then p- and o- benzoquinone, maleic and oxalic acids. CO_2 and H_2O products were observed in alkaline media. To increase the ozone quantity

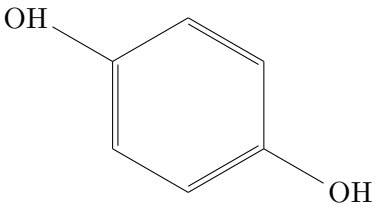

FIGURE 1.6: The structural formula of a hydroquinone molecule.

in the medium, "catalytic" ozonation processes are well described in literature[139,205,207]. We mention as an example the combination of ozone to ultraviolet radiations with or without the presence of hydrogen peroxide. Unfortunately, ozone is unstable in water since it decomposes to oxygen at a rate proportional to the pH of the water[206] and

therefore the pH of the solution influences the final result[139]. Moreover, its reaction with the organic matter results in the formation of by- products which are more readily biodegradable than their precursors but will promote biological growth thus limiting its efficiency. In addition, many refractory and/or dangerous by-products persist after treatment[127,208] meaning that high disposal costs or the development of regeneration methods must be set in place[194,209]. To justify its main application in the disinfection of drinking water, one has to resort to its effectiveness in destroying bacteria, viruses and certain algae and as a pre-treatment for biological purification[210].

Oxidation using hydrogen peroxide Hydroxyl radicals can also be generated starting from various oxidants such as hydrogen peroxide H_2O_2. The processes using this oxidizing agent are known as Wet Peroxide Oxidation (WPO). Even though it is a less powerful oxidant compared to ozone (see section 1.3.2.4), H_2O_2 is liquid in normal conditions reducing the phase transfer problems. When added to the contaminated water without any additional external contribution, this oxidant is unable to treat the organic matter[151]. Indeed, hydrogen peroxide must be decomposed into free hydroxyl radicals, which can be accomplished in the presence of a transition metal ion which plays the role of a homogeneous or heterogeneous catalyst (like classic Fenton or Fenton-like reaction). Sometimes, H_2O_2 is decomposed in the presence of the catalyst *and* UV- visible radiations (like for the photo-Fenton reaction)[203,211]. Other decomposition systems can be set in place, like for example H_2O_2/ultrasounds.

In 1894, Fenton used a ferrous ion/hydrogen peroxide system (Fe^{2+}/H_2O_2) to oxidize tartaric acid[212]. This catalytic system is nowadays known as the Fenton reagent and the hydroxyl radicals generation occurs according to Equation 1.13 (classic Fenton reaction) based upon a first comprehensive paper by Barb et al.[213]. However, research showed that at some pH values, the reduction of Fe^{2+} to Fe^{3+} can occur (Fenton-like reaction)[214] engendering another reaction which can take place in the medium according to Equation 1.14[215].

$$\underset{\text{ferrous ion}}{Fe^{2+}} + H_2O_2 \longrightarrow Fe^{3+} + HO^- + HO^\bullet, \tag{1.13}$$

$$\underset{\text{ferric ion}}{Fe^{3+}} + H_2O_2 \longrightarrow Fe^{2+} + H^+ + HOO^\bullet. \tag{1.14}$$

Whether the classic Fenton reaction or the Fenton-like process, the reactive system remains of much interest for researchers whether for its mechanism comprehension[216,217] or its amelioration in the water treatment field[211,218]. In their work, Matta et al.[151] showed that a $0.53\,\text{mmol}\cdot\text{L}^{-1}$ solution of phenol is readily oxidized in the presence of $155\,\text{mmol}\cdot\text{L}^{-1}$ of hydrogen peroxide by varying the amount of a synthetic mixture

of ferrous- ferric hydroxides called Green Rust (GR) at neutral pH and ambient temperature. The authors observed that phenol was transformed after 1 min mainly into catechol and hydroquinone (see Figures 1.5 and 1.6) however complete mineralization was unachievable. They compared this experiment to another one in which no GR was added to the medium and concluded that oxidation of phenol was always negligible in the absence of GR (thus the absence of $HO^{\bullet}$ radicals).

WPO operating conditions are milder than WAO [198,200] (see section 1.3.2.3), but remains a partial process. The aqueous medium remains refractory since products such as acetic acid and other di-carboxylic acids (oxalic acid, succinic acid, etc.) still persist in the medium [151]. However, other metallic salts may replace or be added to iron salts to improve the oxidation of certain compounds (such as Cu^{2+}, Mn^{2+}, Co^{2+}, etc.). In this way, a homogeneous Fe/Cu/Mn catalyst has been developed to obtain further oxidation which was possible due to synergistic effects [219].

Just like with ozone, the effectiveness of the treatment depends on various parameters including reagents concentration, pH and temperature. For example, an optimum temperature range of 100 to 140 °C appears to be necessary to achieve a satisfactory degradation of a wide variety of compounds [200] whereas the decomposition of hydrogen peroxide into $HO^{\bullet}$ radicals is favored at a pH varying between 3 and 4 [218,220,221].

Oxidation in the presence of ultraviolet radiations Hydroxyl radicals can be generated in the presence of ultraviolet radiations (UV). The radicals are the result of the interaction between photons and a chemical substance (a catalyst and/or an oxidant) such as H_2O_2 or titanium dioxide (TiO_2) which are capable of absorbing UV light. Another variant of the classical Fenton reaction (see section 1.3.2.4) is the photo-Fenton reaction in which the catalytic system is formed by Fe^{2+}/UV irradiation. In the following, we will briefly discuss the interest of the UV radiations. Interesting reviews are found in the literature [127,222,223].

Photocatalytic processes have gained much attention in the waste water treatment field due to several factors of which complete mineralization, mild operating conditions and low cost in comparison to the other purification techniques [127,223]. In the presence of UV radiations ($\lambda < 280\,nm$), H_2O_2 molecules are cleaved into hydroxyl radicals according to Equation 1.15 which is the most accepted mechanism. This cleavage is pH dependent [139,222].

$$H_2O_2 \xrightarrow{h\nu} 2\,HO^{\bullet} \tag{1.15}$$

UV radiations can also be used in the presence of solid catalysts (semi-conductors) such as titanium dioxide TiO_2. When TiO_2 is irradiated by a UV source with an energy equivalent to or greater than the photocatalytic semiconductor's band energy, the incidence of a photon results in the formation of electrons (e^-) in the conduction band and positive holes (h^+) in the valence band, as well as the formation of $HO^\bullet$ radicals[204,224–226]. Thus, when the position of the holes meet with the hydroxyl radicals or any other electron donor (likeH_2O or O_2) and are adsorbed on the surface of the catalyst, free radicals are generated[204].

In their work, Yawalkar et al.[227] compared two catalytic systems for the degradation of phenol using UV from solar radiation: H_2O_2/UV and TiO_2/air/UV. The authors showed that the reaction's mechanism in both systems is different. Indeed, in the presence of TiO_2, the amount of the reaction's intermediate products is smaller than in the presence of H_2O_2 and thus leading to higher concentrations ofCO_2, the final reaction product . This catalytic system was also cheaper.

Other semiconductors acting as photocatalysts exist, such as tungsten trioxide (WO_3), strontium titanate ($SrTiO_3$), zinc sulfide (ZnS), etc[223]. However, TiO_2 remains the most advantageous. Thus, the majority of studies aim to improve its efficiency since it is biologically and chemically inert, inexpensive and corrosion resistant. The emission of UV light has been tested on many pollutants such as dyes[228] and chlorophenols[229]. However, the separation of the treated effluent and titanium dioxide (TiO_2) is difficult to achieve given that the latter tends to agglomerate during this operation. In addition, the low overlap between the solar spectrum and the absorption spectrum of TiO_2 reduces the efficiency of the process. Thus, these problems are the two main disadvantages of the heterogeneous photocatalysis in the presence of this catalyst.

Almost all water treatment plants until recently include conventional processes such as physical or chemical treatment methods. However, new technologies have emerged to meet the needs of health authorities and respect the law in a more efficient and economical way. Since cavitation bubbles produce highly reactive oxidizing species in their vicinities, cavitation-based techniques are considered to be part of the AOPs. Cavitation proved to be quite interesting and many studies were developed to optimize this phenomenon for industrial waste water treatments[127,129].

Chapter 2

Physical response of a liquid to an impact

Contents

As presented in Chapter 1, there exists several techniques to induce fast pressure changes in a liquid. In particular, a piston impact on a liquid surface generates series of pressure fluctuations which, under certain conditions, induce the appearance of bubbles under tension states followed by their implosion.

In this chapter, we examine the phenomena induced by the impact of a piston on a liquid containing bubbles of controllable size confined in a closed vessel[230]. This device is designed to overcome the classical problems of acoustic and hydrodynamic cavitation and to control several variables which have been proven to have a great influence on the bubble collapse process such as the bubble radius distribution and the frequency and amplitude of the excitation wave. To control the intensity of the bubble collapse is the first step towards the control of the physical and chemical phenomena triggered by the collapse of bubbles[1,55,62,231].

This chapter is structured as follows: in section 2.1 we present the experimental device and we provide details about the methods used to obtain the experimental data. In section 2.2 we investigate the dynamics of the impact of a piston on a liquid free surface enclosed in the reactor when the bottom of this latter is fixed. We present the results of

the generated pressures in the medium, the characteristic impact times and frequencies and we present a model that gathers all the parameters influencing the strength and main frequency content induced by the impact of the piston on the free surface. Finally, in section 2.3, we compare the effect of the mobility of the bottom of the reactor on the parameters mentioned earlier.

2.1 Experimental set-up and measurements

2.1.1 Experimental set-up

The experimental arrangement, developed by Fuster et al. [230], is schematically presented in Figure 2.1 along with the velocity and pressure measurement systems.

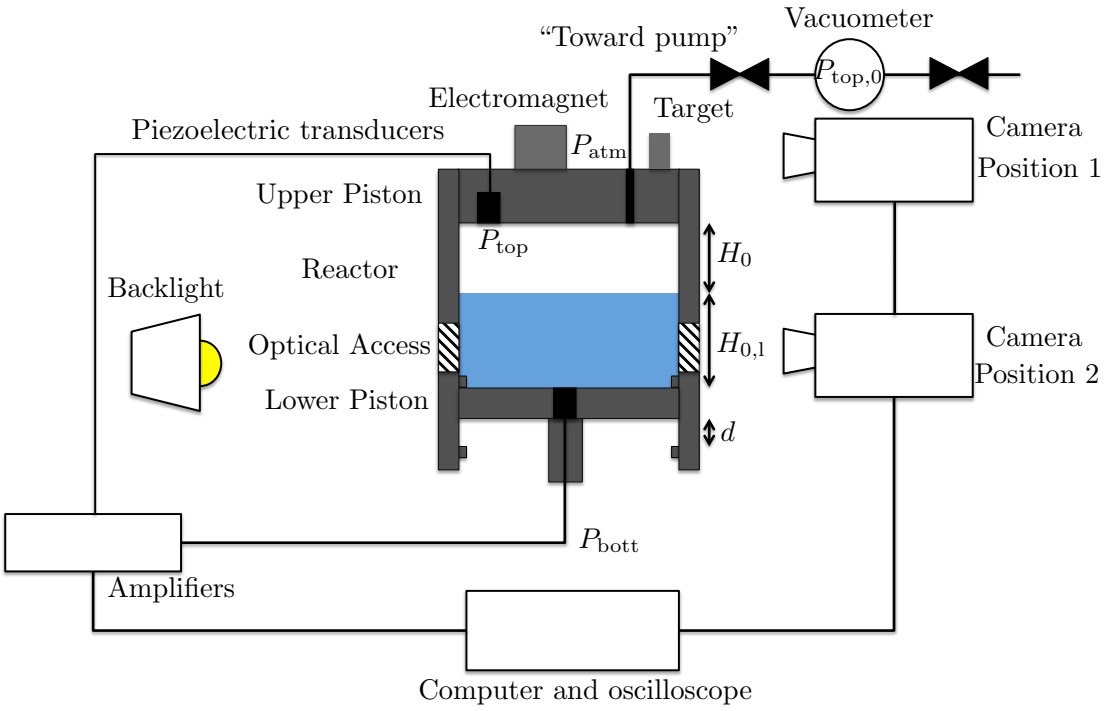

FIGURE 2.1: Sketch of the experimental apparatus used to induce cavitation with a piston and to observe the bubble dynamic response.

The apparatus consists of a cylindrical reactor (stainless steel, internal diameter 0.075 m) filled with a liquid. The initial height of the liquid level, $H_{0,l}$ is typically of the order of 30 cm. An upper piston of mass $m_p = 0.530$ kg is used to impact the liquid free surface. The side walls of the reactor are equipped with two opposed optical accesses for the purpose of visualizing the liquid's response to the impact. Note that they can be

obstructed. The bottom part of the reactor consists of another piston which displacement is restricted between two vertical positions of separation length d. Note that when $d = 0$, the reactor can be considered as a non-deformable rigid-wall vessel.

The initial height of the upper piston above the liquid free surface, H_0 is set by an electrical actuator (not presented on the sketch) which controls the displacement of an electromagnet. The attachment and release sequences of the piston by the electromagnet are controlled by a computer.

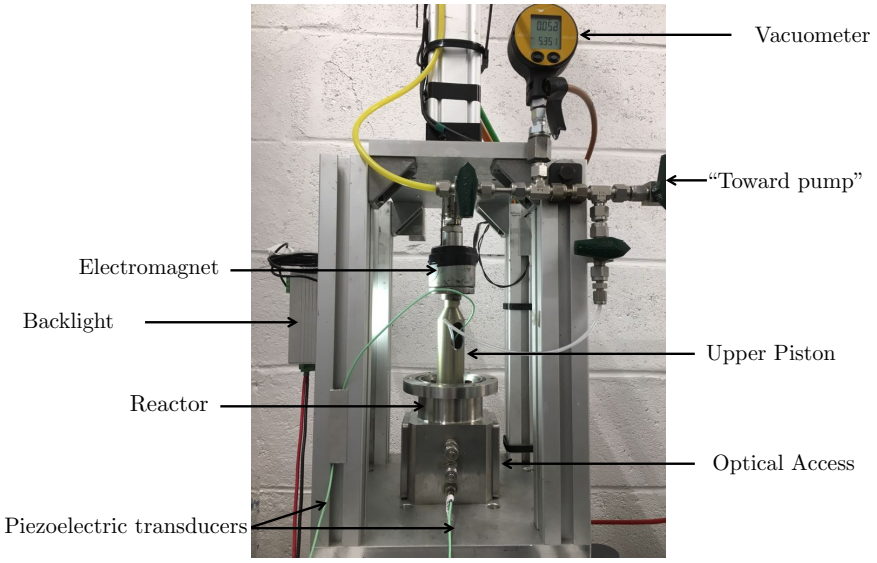

FIGURE 2.2: Photo of part of the experimental apparatus.

The initial pressure between the free surface of the liquid and the upper piston when the latter is still attached to the electromagnet, $P_{\text{top},0}$, is regulated using a vacuum pump. The minimum reachable value of $P_{\text{top},0}$ is the liquid's vapor pressure, i.e. water in the experiments herein and equal to 2.3 kPa at ambient temperature. $P_{\text{top},0}$ is measured using a digital vacuometer (LEO 2, Keller) attached to an evacuation pipe. It has a dynamic range from -0.1 to 0.3 MPa with a 100 Pa resolution. Because of the unavoidable presence of dissolved gases in the liquid, $P_{\text{top},0}$ is a measurement of the pressure of the vapor initially present between the liquid's free surface and the piston.

When the electromagnet is switched-off, the pressure difference between both sides of the piston generates a force which accelerates the latter towards the liquid's surface. The pressure above the piston is the atmospheric pressure, P_{atm}. When the piston finally impacts the liquid, rapid pressure changes are generated and used to promote fast bubble dynamic processes.

The temporal evolution of the pressure under the piston, P_{top}, and at the bottom of the reactor, P_{bott}, are both measured using two flush-mounted piezoelectric transducers (601H, Kistler) which natural and cut-off frequencies are equal to 150 to 300 kHz respectively. The pressure captors are calibrated by the manufacturer and although they are destined to record a dynamic pressure, dynamic tension can also be recorded (to a certain extent according to the manufacturer). Thus, the discussion of negative pressures (tension states) will remain only qualitative. The pressure signals are amplified (5018A, Kistler) and recorded using a high-frequency oscilloscope (InfiniiVision MSO7054A, Agilent Technologies). Note that neither digital nor hardware filtering is employed in the pressure signal recording pathways and the amplifier does not incorporate electronic filtering circuitry.

We record the successive images of the piston's position using a high-speed video camera (Phantom v711,Vision Research) when it is in Position 1 and the piston's velocity is obtained by simple derivation. An explanation of the numerical detection of the piston's position is detailed in Appendix A. The pressure signals and the image recordings are triggered by the output from one of the pressure transducers (threshold value 0.1 MPa). When we study the behavior of pre-existing bubbles in the system during and after the piston's impact, we place the camera in position 2 (see Figure 2.1). For these high speed visualizations, we use a white LED lamp (RT220-20, Gardasoft Vision) for backlighting. Part of the experimental set-up is presented and detailed in Figure 2.2.

2.1.2 The effective pressure in the reactor $\overline{P_{\text{int}}}$

The pressure recordings obtained from the piezoelectric transducers contain information about both the *background* and the local pressures. The former, generated by the piston's impact, induces nucleation followed by the collapse of bubbles. As for the latter, it is generated by the bubbles' response. For that reason in this manuscript, we compute an average effective chamber pressure using Newton's second law applied to the "piston" system. Neglecting the piston's weight and the friction forces, we express the average effective pressure below the piston, $\overline{P_{\text{int}}}$, equal to P_{top}, as:

$$\overline{P_{\text{int}}} \;=\; P_{\text{top}} \;=\; P_{\text{atm}} \;-\; \frac{m_{\text{p}}}{S_{\text{p}}}\frac{dU}{dt}, \tag{2.1}$$

where U and S_{p} are respectively the piston's velocity and surface. In the following, the reported maximal peak pressures are calculated from Equation 2.1.

2.1.3 Uncertainty measurements

The instantaneous piston position obtained from the images are detected within an error of the order of the pixel size, which is of the order of few microns.The sampling acquisition rate is 50 000 frames/s. Based on the piston's maximum velocities and impact heights presented herein, the plate velocity computed is estimated with an uncertainty lower than 1 %.

The data from the pressure transducers is acquired with an oscilloscope at a sampling rate of 1.25 MS s^{-1}. The voltage range is chosen as ±8V for all the runs of this study. The oscilloscope has an effective resolution of 8 bits at 1.25 MS s^{-1}. This gives an output resolution of 62.5 kPa.

2.2 The impact of a piston on a liquid enclosed in a *fixed-bottom* reactor

2.2.1 Characteristic stages of the process

We describe the characteristic stages of the process of the piston's descent based on a qualitative description and through the analysis of its position, velocity and the pressure signal. Figure 2.3 presents a typical example of the temporal evolution of the piston's position, H, the piston's velocity, U, and the average pressure under the piston, P_{top}, as a function of time for an initial impact height of $H_0 = 16$ mm. Time averaging is performed over five data samples. Every single sample is first shifted in time so that the origin $t = 0$ is defined as the instant when the piston's velocity is maximum, U_{max}. Based on the analysis of Figure 2.3, we propose to divide the evolution of the system into three characteristic stages described below.

The *acceleration stage* (Figure 2.3, green) begins when the piston is released and ends when the velocity U reaches its maximum value U_{max} at $t = t_{U_{max}}$. Note that as presented earlier, $t_{U_{max}}$ is equal to zero. During this stage, the pressure in the medium is lower than the ambient pressure (i.e., P_{atm}) and the piston's acceleration reaches a quasi-constant value as evidenced by the quasi- linear evolution of the piston's velocity U. The work of the external pressure force is mostly converted into the piston's kinetic energy, although during the very last instants of this stage, part of this energy is also used to increase the average temperature and pressure of the gas/vapor layer existing between the piston and the liquid's surface.

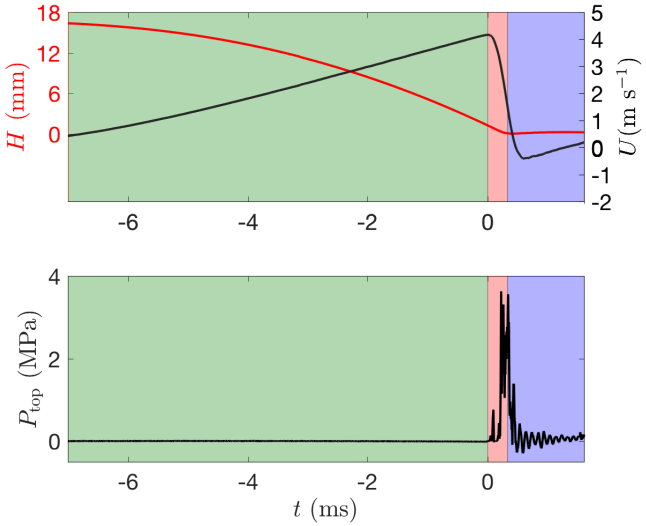

FIGURE 2.3: Top: Temporal evolution of the average position (red line) and piston velocity (black line). Bottom: Pressure under the piston for $H_0 = 16\,\text{mm}$ for a fixed bottom configuration.

The *compression stage* (Figure 2.3, orange) is defined as the time evolution of the system between $t_{U_{max}}$ and the moment when the chamber's pressure reaches its peak value, $P_{\text{top,max}}$. This instant is identified as the moment when the piston hits the liquid-gas interface. When the inner pressure forces equilibrate the outer pressure forces acting on the piston (which occurs at $t_{U_{max}}$), the piston's velocity starts decreasing, whilst the pressure of the gas/vapor layer keeps increasing. Figure 2.4a shows a typical example of the piston's position and velocity (in red and black respectively) whilst Figure 2.4b presents the experimental pressures P_{top} (in black) and P_{bott} (in red) measured using the piezoelectric transducers placed respectively at the piston's surface and at the reactor's bottom. Note that both figures are zoomed. The averaged pressure inferred from the piston's velocity data (Equation 2.1) is also presented (in blue). We can first note that there is no observed lag between the two pressure signals P_{top} and P_{bott} (see Figure 2.4b), which can be explained by the fact that the characteristic liquid height, $H_{0,\text{l}}$ (Figure 2.1) is smaller than the wavelength of the wave induced during the impact, $\lambda = c_\text{l}/f_\text{i}$, where c_l is the speed of sound in the liquid and f_i the characteristic frequency generated during the impact. This results by a uniform *background* pressure inside the chamber. We also note that the effective pressure given by Equation 2.1 is consistent with the direct pressure measurements of the transducers. In this case, the pressures are localized and it is possible to detect the high frequency fluctuations induced by the hydrodynamic pressure changes generated by the dynamics of surrounding bubbles by simple subtraction of the experimental and calculated signals. By using Equation 2.1, local pressure fluctuations are smoothed out and we obtain a filtered evolution of the average effective pressure $\overline{P_{\text{int}}}$ acting on the piston.

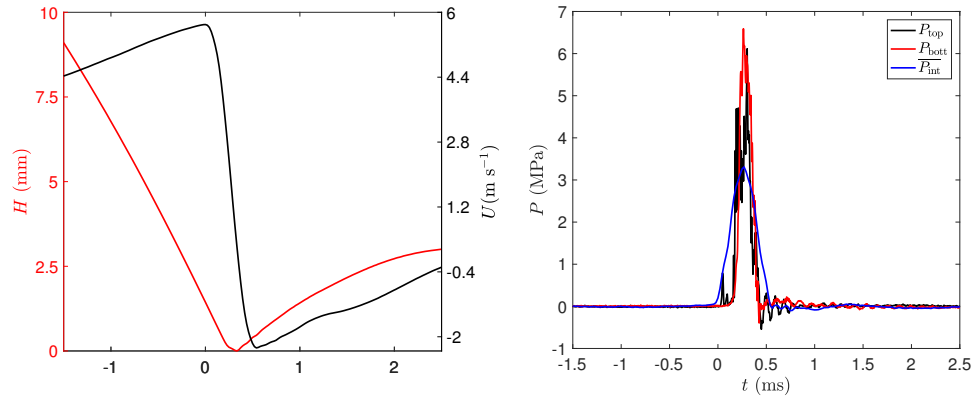

(a) (b)

FIGURE 2.4: (a): Temporal evolution of the position (red line) and the piston velocity (black line) for $H_0 = 20\,\text{mm}$ and $d = 0$. (b): Temporal evolution of the pressures experimentally measured (P_{top} and P_{bott}) and the effective pressure ($\overline{P_{\text{int}}}$).

The *rebound stage* (Figure 2.3, violet) is characterized by the minimum (negative) piston's velocity, U_{min}. When the piston impacts the liquid surface, the averaged pressure inside the chamber is greater than the outer (atmospheric) pressure and the piston rebounds on the surface. During this stage, the pressure inside the reactor decreases and it is possible to observe tension states (Figure 2.4b, $\approx 0.5\,\text{ms}$) which induce the activation of bubble nuclei present in the system. After this stage, the chamber's pressure recovers back making bubbles implode. Finally, successive impacts and rebounds of the piston occur with decreasing intensities due to the irreversible nature of the process.

2.2.2 Characteristic pressures induced by the impact of a piston on a liquid enclosed in a chamber

Figure 2.5 presents the computed maximum pressure in the reactor, $P_{\text{top,max}}$ (from Equation 2.1) as a function of the piston's maximum velocity, U_{max}, for various initial pressures $P_{\text{top,0}}/P_{\text{vap}}$.

The amplitude of $P_{\text{top,max}}$ is proportional to the peak velocity U_{max}. For the conditions tested here, pressures of the order of 0.5 to 3 MPa are obtained. A first estimation of the peak velocity U_{max} and of the maximum pressures generated during the impact are obtained from a simple model in which the gas/vapor layer is absent. In this case we obtain an estimation of U_{max} from Newton's second law considering that the friction forces are negligible and that the internal pressure is negligible compared to the

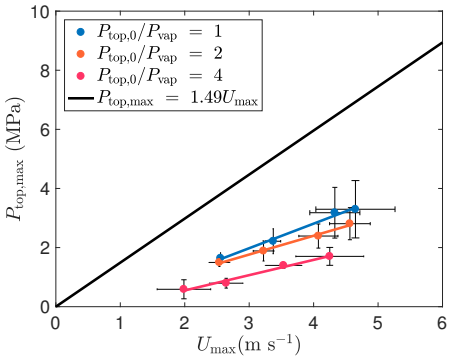

$P_{top,0}/P_{vap}$	Slopes (10^6 kg · m^{-2} · s^{-1})
1	0.8313
2	0.636
4	0.5171

FIGURE 2.5 & TABLE 2.1: Maximum pressure under the piston $P_{top,max}$ as a function of the maximum velocity U_{max} for various initial pressures $P_{top,0}/P_{vap}$ (colored data) and the theoretical solution to the water-hammer theory (in black). In the table, we show the experimental linear fits of the maximum pressure $P_{top,max}$ as a function of the maximum velocity U_{max} for various initial pressures $P_{top,0}/P_{vap}$.

external/atmospheric pressure during most of the *acceleration stage*,

$$U_{max} = \sqrt{\frac{2P_{ext}S_pH_0}{m_p}} . \tag{2.2}$$

Equation 2.2 shows that U_{max} is independent of $P_{top,0}$, although the experimental data show a *slight but systematic* dependence of the maximal velocity on the initial pressure. We emphasize that Equation 2.2 remains valid only for very low initial pressures when the simplifications adopted are acceptable. The experimental dependence of the piston's maximum velocity on the piston's initial position H_0 is presented in Figure 2.6.

A simple model to compute the peak pressures generated during the impact can be derived from the analytic solution used in the context of the water-hammer theory in which a sudden pressure change is caused when a fluid in motion is suddenly forced to stop. This theory allows the evaluation of the maximum magnitude of the water hammer pulse from the Joukowsky equation as, $P_{top,max} = \rho_l c_l U_{max}$ where ρ_l is the liquid's density. Note that c_l can be calculated[232] from the empirical Equation 2.3 in the temperature T and pressure P range of 273 to 293 K and 10^5 to 10^7 Pa respectively as:

$$c_l = c_0 + A(T - T_0) + BP, \tag{2.3}$$

where $c_0 = 1447\,\mathrm{m \cdot s^{-1}}$, $T_0 = 283.16\,\mathrm{K}$ and the constants A and B are equal to $A = 4\,\mathrm{m \cdot s^{-1} \cdot K^{-1}}$ and $B = 1.6 \times 10^{-6}\,\mathrm{m \cdot s^{-1} \cdot Pa^{-1}}$. This theoretical solution is presented in Figure 2.5 for pure water (continuous black line) for which the slope is equal to $\rho_l c_l = 1.490 \times 10^6\,\mathrm{kg \cdot m^{-2} \cdot s^{-1}}$.

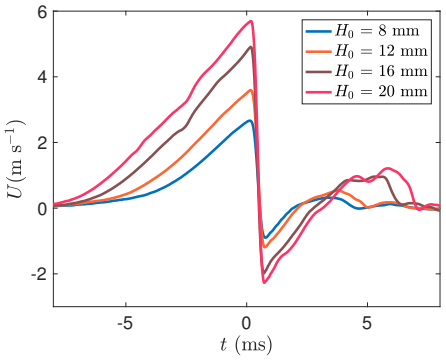

FIGURE 2.6: Temporal evolution of the piston velocity U for various H_0.

The data presented in Figure 2.5 show that the damping effect of the gas/vapor layer neglected in the theoretical approach becomes increasingly important when the initial pressure under the piston $P_{\text{top},0}$ increases. Indeed, the peak pressures and slopes determined experimentally are significantly smaller than the computed values for a sudden piston-water impact (see Table 2.5) revealing the importance of the presence of the gas/-vapor layer during the last instants before the impact. In particular, the peak pressures obtained during the *compression stage* appear to be function of the amount of vapor enclosed in the chamber. The influence of the gas/vapor layer on the peak pressures generated in the medium can be explained by the fact that during the instants before the impact the compression of the gas/vapor layer tends to decrease the piston's velocity.

The thickness of the gas/vapor layer at $t_{U_{max}}$ referred to as h_c, is an important parameter controlling the characteristics of the impact. We can measure it experimentally as the difference between the piston's position at the moment of maximum velocity and the instant at which the piston's position reaches its minimal value. Figure 2.7a presents the experimental values of h_c as a function of the impact height H_0 and for various initial pressures under the piston, $P_{\text{top},0}/P_{\text{vap}}$. The values obtained for h_c range from 0.5 to 3.5 mm. We propose a simple model to predict h_c assuming that the gas/vapor layer follows a polytropic compression law during the *acceleration stage*. From the time at which $P_{\text{top},0}$ is fixed to the instant $t_{U_{max}} = 0$ when the inner pressure forces acting on the piston balance the atmospheric pressure forces, we assume that the pressure of the gas/vapor layer can be described by an effective polytropic evolution such that

$$\frac{h_c}{H_0} = \left(\frac{P_{\text{top},0}}{P_{\text{atm}}}\right)^{1/\gamma_{\text{eff}}}, \tag{2.4}$$

where γ_{eff} is the effective polytropic coefficient of the gas/vapor mixture such that $PV^{\gamma_{\text{eff}}} = C$, C is a constant.

The evolution of the dimensionless gas/vapor layer thickness h_c/H_0 with respect to the

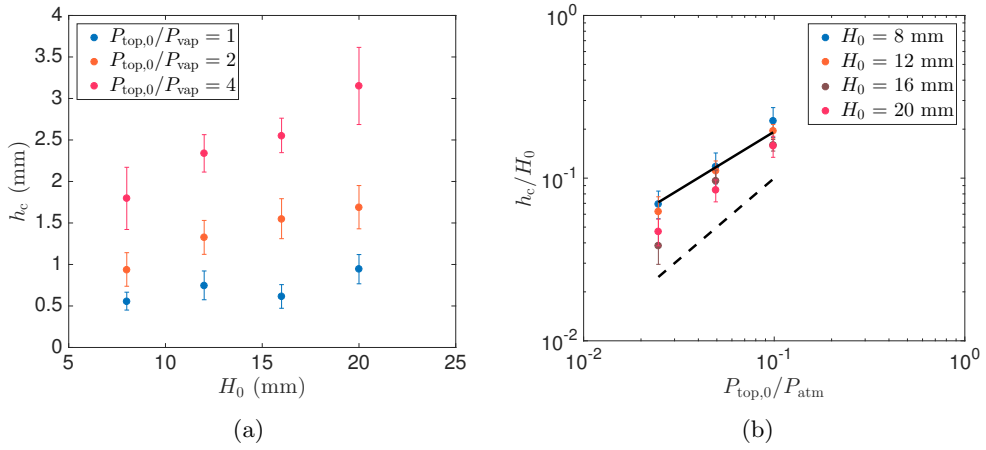

FIGURE 2.7: Left: Experimental gas/vapor layer thickness h_c at $t_{U_{max}}$ as a function of the impact height H_0 for different initial pressure under the piston $P_{top,0}$. Right: Non-dimensional gas/vapor layer thickness as a function of the dimensionless pressure $P_{top,0}/P_{atm}$. Experimental data (o), adiabatic transformation (−) and isothermal transformation (−−).

dimensionless pressure $P_{top,0}/P_{atm}$ is plotted based on the polytropic relation given by Equation 2.4 as presented in Figure 2.7b. For comparison, the isothermal (dashed line) and adiabatic (continuous line) transformations relative to the experimental conditions discussed here are superimposed to the experimental data. Globally, the compression of the gas/vapor mixture in the *acceleration stage* can be modelized as an adiabatic process of an ideal gas, the agreement being remarkably good with the experimental data especially when H_0 is small.

To explain this behavior, we can make an analogy between the response of the rapidly compressed gas/vapor layer trapped between the piston and the liquid volume and the response of gas/vapor bubbles against pressure changes in diluted bubbly liquids[1]. The influence of heat and mass transfer can be discussed as a function of the Péclet and Sherwood numbers defined as the ratio between the averaged compression velocity U_{max} and the characteristic velocity of thermal diffusion D^T/H_0 (to define the Péclet number as $Pe = U_{max}H_0/D^T$) or mass diffusion D^M/H_0 (to define the Sherwood number as $Sh = U_{max}H_0/D^M$), where D^T and D^M are the averaged thermal and mass diffusivities of the gas/vapor mixture.

For low Péclet numbers, the characteristic velocity of heat transfer is larger than the characteristic compression velocity. In this limit, the response of the system is isothermal and the limiting response for a non-condensable gas ($PV = C$) and that of a condensable vapor (where $P = P_{vap}$) is different.

At large Péclet/Sherwood numbers, there is no time to exchange neither mass nor heat with the environment and we expect to find an adiabatic response of the gas/vapor

mixture irrespective of the vapor content. In the present study, typical values of the Péclet numbers during the full compression process of the gas/vapor layer are of the order of 10^3 – 10^4 which, according to the model presented by Fuster and Montel[1], implies that the effective polytropic coefficient of the gas/ vapor mixture corresponds to that of an adiabatic compression even when the vapor content is large. That is, the compression velocity during the *acceleration stage* is larger than the characteristic heat and mass diffusion velocity in the gas/vapor layer.

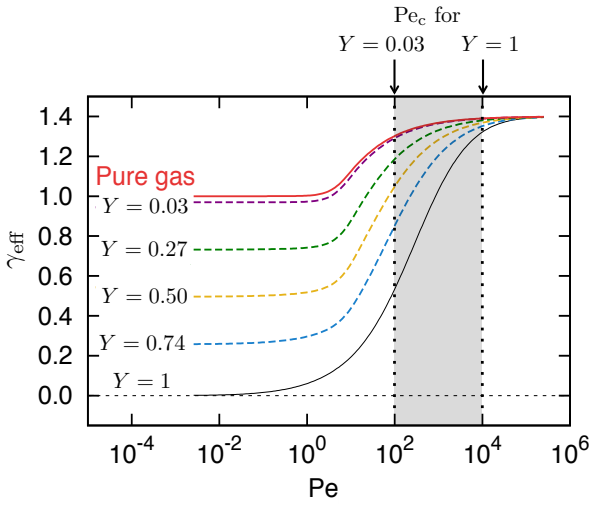

FIGURE 2.8: The evolution of the effective polytropic coefficient as a function of the Péclet number. Adapted from[1].

The situation is different during the *compression stage*. In this case, the instantaneous Péclet/Sherwood numbers, proportional to the instantaneous compression velocity and the thickness of the gas/vapor layer, become small and therefore the compression is no longer adiabatic. We can say that the assumption of an adiabatic compression breaks when

$$\mathrm{Pe} = \frac{UH}{D^{\mathrm{T}}} < \mathrm{Pe_c}, \tag{2.5}$$

where $\mathrm{Pe_c}$ is the critical Péclet number below which thermal and mass transfer effects become important. An estimation of $\mathrm{Pe_c}$ can be obtained from the results of the effective polytropic coefficient reported in Fuster and Montel[1] (see Figure 2.8).

The critical Péclet number is shown to vary between 10^4 for pure vapor mixtures to 100 for pure air. Using $\mathrm{Pe_c}$, we obtain a first estimation of the critical thickness below which the process is no longer adiabatic taking the maximum compression velocity as a characteristic velocity of the process, so that

$$H_{\mathrm{c}} = \mathrm{Pe_c}\frac{D^{\mathrm{T}}}{U_{\max}}. \tag{2.6}$$

This value is of the order of hundreds of microns (for pure gas mixtures) to few millimeters for pure vapor bubbles, showing that the evolution of the gas/vapor pressure is indeed influenced by mass and heat diffusion processes during the last instants before the impact. Due to the pressure increase, vapor condenses slowing down the rate of gas/vapor pressure increase, keeping the compression velocities high. This makes the reachable pressure peaks at the moment of impact dependent on the vapor content. As the vapor content increases (lower initial pressures), condensation processes are more important and the pressures generated at the impact are larger (see Figure 2.5).

2.2.3 Characteristic frequencies induced by the impact of a piston on a liquid enclosed in a chamber

Despite the importance of the amplitude of the pressure wave, it is also essential to characterize the frequencies generated during the impact. The pulses resulting from the impact generate a time-varying signal which requires the use of tools able to capture the appearance of a wide range of frequencies as a function of time. The choice of wavelets is then preferred compared to simple Fourier Transform analyses given that it allows us to quantify the intensity of various frequencies as a function of time. Since the Fourier Transform of the raw signal show a frequency peak at 150 kHz that corresponds to the natural frequency of the transducers, only the frequencies below 100 kHz are taken into consideration.

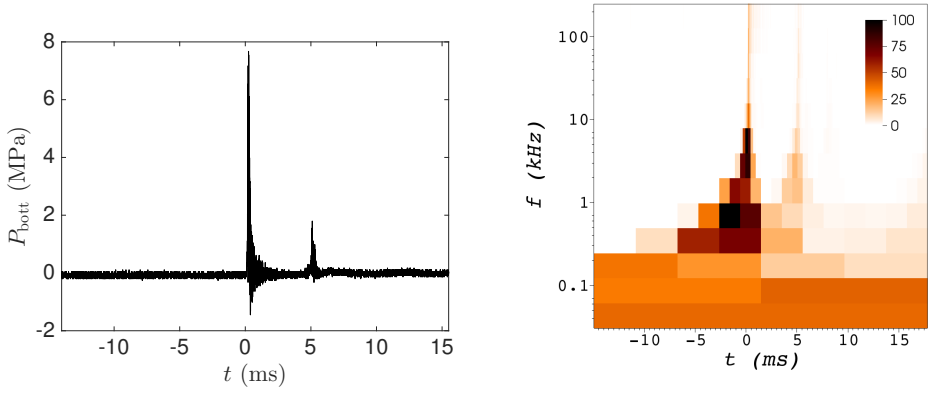

(a) (b)

FIGURE 2.9: (a): Pressure signal at the bottom of the reactor obtained for $d = 0$ and $H_0 = 16$ mm. (b): Daubechies wavelet of the pressure signal presented in (a). The color bar represents the absolute values of the wavelet coefficients, which represent a measure of the signal intensity.

Figure 2.9b presents the result of the treatment of a raw pressure signal P_{bott} (Figure 2.9a) recorded for an impact height $H_0 = 16$ mm using the Daubechies wavelet. We

see that the frequency content is rich during the impact when the peak pressure occurs. In this case, the highest values of the wavelet coefficients are found to lay in the range of 1 to 10 kHz. Figure 2.10 presents the influence on the wavelets of the initial impact height, H_0, equal to 8 and 20 mm respectively. As shown on the figures, H_0 has an impact on the frequency range and intensity generated in the medium. Indeed, the larger H_0 is, the richer the content of the generated frequency is.

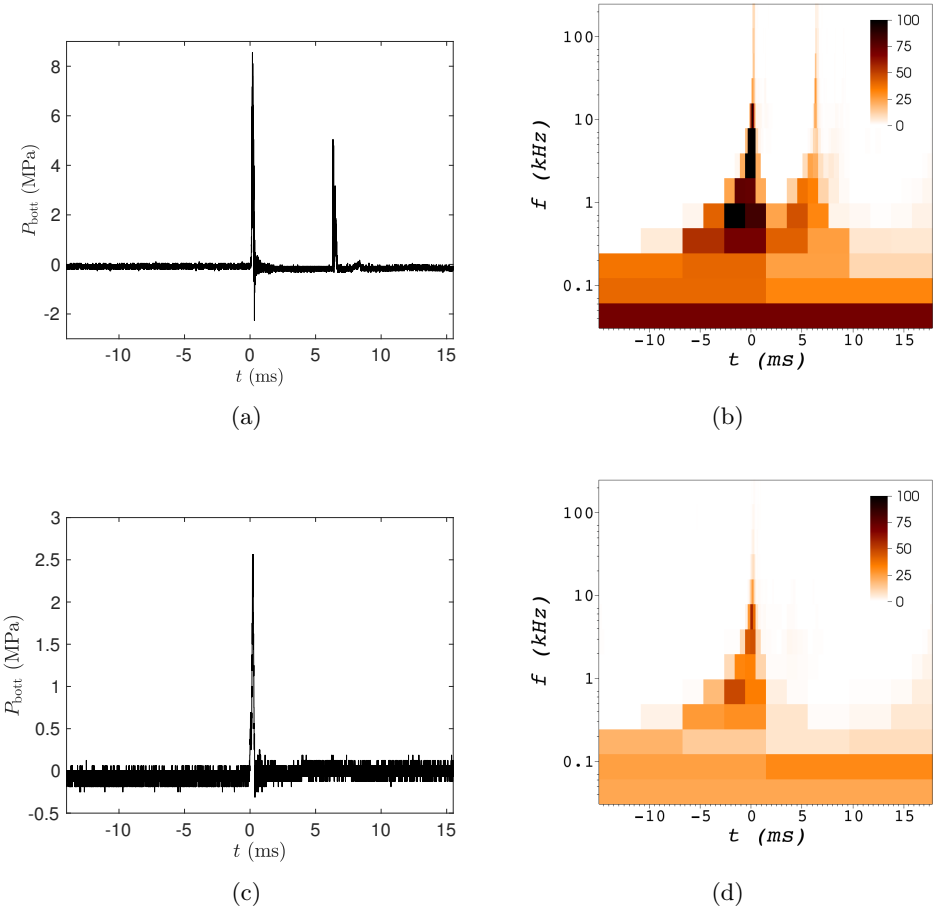

FIGURE 2.10: Left: Pressure signal at the bottom of the reactor obtained for $d = 0$. Right: Daubechies wavelet of the pressure signal presented in (a) and (c). Up: $H_0 = 20$ mm and Down: $H_0 = 8$ mm. The color bar represents the absolute values of the wavelet coefficients, which represent a measure of the signal intensity.

The frequencies generated during the impact can be made non-dimensional by defining a characteristic compression time based on the characteristic length of the gas/vapor layer and peak velocity of the process, $t_c = h_c/U_{max}$. If we replace h_c by the expression presented in Equation 2.4 the resulting formula shows that the non-dimensional frequency is expected to depend only on the initial dimensionless pressure, $\frac{P_{top,0}}{P_{atm}}$ and on the effective polytropic coefficient during the acceleration stage, γ, i.e. $\frac{t_c U_{max}}{H_0} = \left(\frac{P_{top,0}}{P_{atm}}\right)^{\frac{1}{\gamma}}$.

We experimentally obtain the characteristic compression time, t_i, as the time difference between $t_{U_{max}} = 0$ and the instant when $P_\mathrm{top} = P_\mathrm{top,max}$. Figure 2.11a presents the experimental values of t_i with respect to the impact height H_0 for various initial pressures below the piston, $P_\mathrm{top,0}/P_\mathrm{top,max}$. Typical values of the impact time are of the order of 0.2 to 1.6 ms. The amount of gas/vapor trapped between the piston and the liquid's free surface influences the time lapse over which compression occurs.

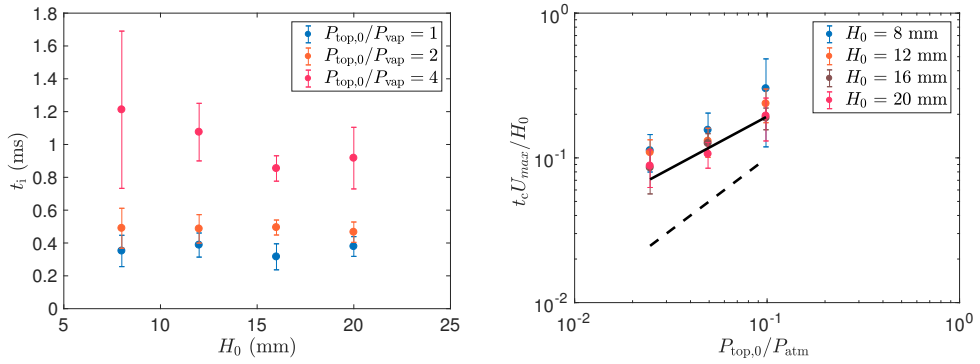

(a) (b)

FIGURE 2.11: (a): Impact time t_i as a function of the impact height H_0. (b): Non- dimensional impact time $t_\mathrm{c}U_\mathrm{max}/H_0$ as a function of the dimensionless pressures $P_\mathrm{top,0}/P_\mathrm{atm}$. Experimental data (o), adiabatic transformation (−) and isothermal transformation (−−).

In Figures 2.12a and 2.12b we represent the maximal frequencies generated in the medium from the pressure signals using the Daubechies wavelets, f_max, as a function of H_0 along with its dimensionless representation as a function of $P_\mathrm{top,0}/P_\mathrm{atm}$. The linear fit of the experimental data presented in Figure 2.12b gives: $\frac{f_\mathrm{max}H_0}{U_\mathrm{max}} = 0.013 \left(\frac{P_\mathrm{top,0}}{P_\mathrm{atm}}\right)^{-\frac{1}{0.5}}$. We can clearly see that the characteristic time H_0/U_max suffices to collapse the experimental data on a single curve. As expected, the frequencies generated during the impact decrease when increasing the amount of air given that the compression of air makes the chamber pressure to increase sooner. When fitting the obtained non-dimensional frequencies generated during the impact against the non-dimensional vapor pressure, we can obtain the effective polytropic coefficient during the compression. The value obtained $\gamma_\mathrm{eff} \approx 0.5$ is consistent with the fact that the Péclet numbers are significantly smaller during the *compression stage*, which makes heat and mass transfer effects to control the peak pressures and frequencies generated during the impact. From Figure 2.8 we can see that for a pure vapor mixture the effective polytropic coefficient is of the order of 0.5 for values of the Péclet number around 100. This is consistent with the experimentally measured values of the Péclet number and the estimations of the effective polytropic coefficient from the theoretical model.

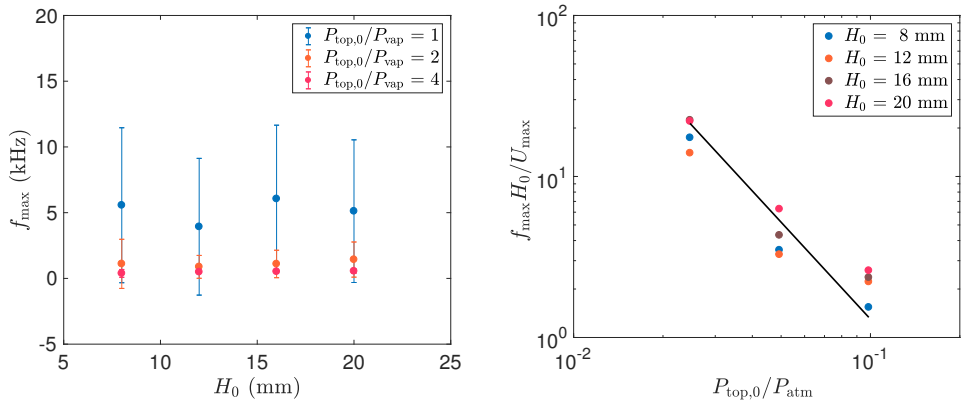

FIGURE 2.12: (a): Impact frequency determined through the wavelet analysis f_{max} as a function of the impact height H_0 and (b): Non-dimensional frequency determined through the wavelet analysis $f_{max}H_0/U_{max}$ as a function of the dimensionless pressure $P_{top,0}/P_{atm}$.

2.2.4 Summary

As a summary of the previous discussion, Figure 2.13 gives the different transformations of the gas/vapor layer upon its compression by the piston's descent. We show that the impact of the piston on the liquid's surface generates an approximately spatially uniform variation of the pressure in the system. Both the characteristic amplitude and frequency of the impact are strongly influenced by the dynamics of the gas/vapor layer trapped between the piston and the liquid's surface. In addition to this parameter, the amplitude of the pressure variation induced in the system strongly depends on the impact velocity and the medium's compressibility.

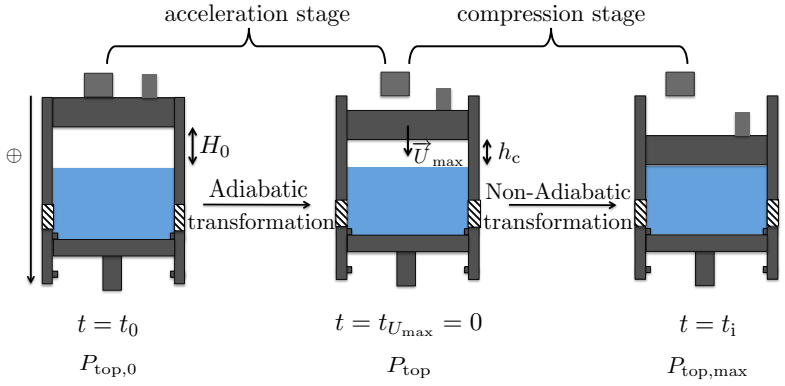

FIGURE 2.13: A sketch of the transformations of the gas/vapor layer upon its compression.

It is noteworthy that we expect to generate higher and faster pressure changes and frequencies when increasing the external pressure P_{ext} and decreasing the piston's mass per unit surface m_p/S_p (which is a measure of the inertia per unit surface). The effect

of the impact height H_0 is more intricate. In fact, if we increase H_0, the intensity of the impact could be augmented at the expense of decreasing the characteristic frequencies generated during the impact. As we will see in the next Chapter, this is going to restrict the range of bubble sizes that undergo an intense collapse.

Simple models are proposed from simple manipulation of Equations 2.2, 2.4 and the Joukowsky equation (see section 2.2.2) to predict the characteristic frequencies $f_{\max}$ generated by the impact and the pressure peaks $P_{\text{top,max}}$,

$$\frac{P_{\text{top,max}}}{\rho_l c_l U_{\max}} = C_0, \tag{2.7}$$

$$\frac{f_{\max} H_0}{U_{\max}} = C_1 \left(\frac{P_{\text{atm}}}{P_{\text{top},0}} \right)^{\frac{1}{0.5}}, \tag{2.8}$$

C_0 is experimentally found to be between 1/3 and 1/2 and C_1 is 0.013 from the linear fits of Equations 2.7 and 2.8. It must be noted that these expressions include the damping effect due to the presence of gas.

2.3 The impact of a piston on a liquid enclosed in a *mobile-bottom* reactor

2.3.1 Comparison between the fixed- and mobile-bottom configuration: the characteristic stages

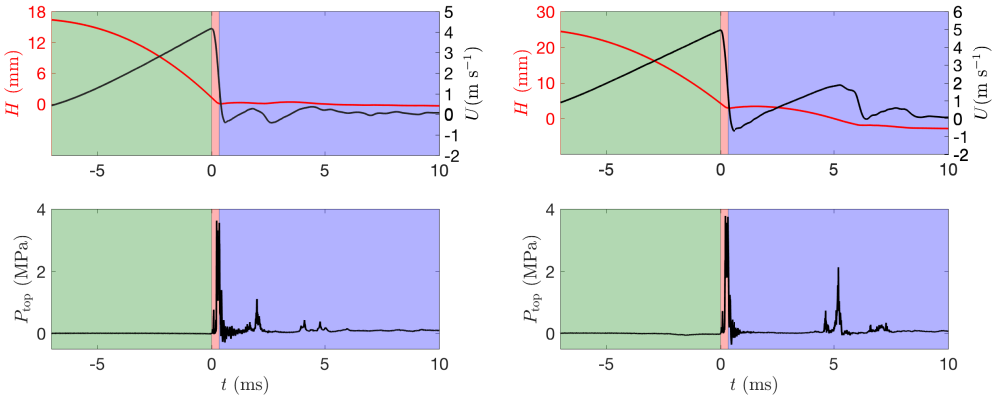

FIGURE 2.14: Top: Temporal evolution of the average position (red line) and piston velocity (black line). Bottom: Pressure under the piston for $H_0 = 16$ mm for (a): fixed bottom and (b): mobile bottom configurations.

In section 2.2.1, we determined three characteristic stages of the piston's descent towards the water column when the lower piston (see Figure 2.1) is immobile, i.e. $d = 0$. In the

following section, we briefly expose the differences observed when $d \neq 0$. Before doing so, whether the lower piston is mobile or fixed, note that no changes are brought up to the experimental set-up except for the reactor's bottom mobility. Herein, $d = 10\,\text{mm}$. As a result, to compensate for this mobility, the initial impact height value H_0 is augmented by d giving: $H_0^{d\neq 0} = H_0^{d=0} + d$.

In Figure 2.14b we present the characteristic stages determined for an impact height $H_0 = 16\,\text{mm}$ when $d \neq 0$. Like for the fixed-bottom configuration which we re-present in Figure 2.14a (the figure is zoomed-out), three characteristic stages can be defined. The most markedly difference between both configurations is the amplitude of the minimal velocities after the impact. In addition, note that after the piston rebound we observe a second impact, hence with lower magnitude than $U_{\max}$ but with a higher intensity compared to the fixed-bottom configuration.

2.3.2 Comparison between the fixed- and mobile-bottom configuration: effect on $P_{\max}$ and h_c

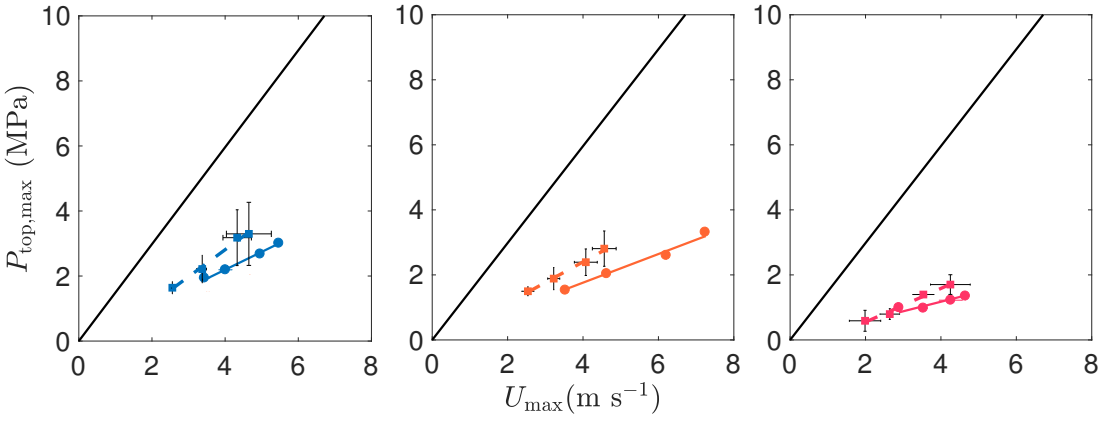

FIGURE 2.15: The evolution of the maximum pressure under the piston, $P_{\max}$ as a function of the maximum velocity $U_{\max}$ when $d \neq 0$ in dashed lines and in continuous lines for $d = 0$. From left to right: $\frac{P_{\text{top},0}}{P_{\text{atm}}} = 1$, $\frac{P_{\text{top},0}}{P_{\text{atm}}} = 2$ and $\frac{P_{\text{top},0}}{P_{\text{atm}}} = 4$.

We present in Figure 2.15 the evolution of the maximum pressure under the piston, $P_{\max}$ as a function of the maximum velocity $U_{\max}$ when $d \neq 0$ in dashed lines and in continuous lines for $d = 0$ for $\frac{P_{\text{top},0}}{P_{\text{atm}}} = 1$, 2 and 4 (from left to right). We can say that the presence of the gas/vapor layer is as much important as when $d = 0$. Indeed, the larger the gas content is, the smaller the slope relating $P_{\max}$ to $U_{\max}$ is. Again, the experimental values are smaller than the theoretical evolution expected from the water-hammer theory addressed in section 2.2.2 showing once again the importance of the role played by the gas/vapor layer.

The influence of the various parameters on the peak pressures generated during the impact is similar to the configuration of fixed-bottom chamber. Figure 2.16a presents the evolution of h_c, the thickness of the gas/vapor layer as function of H_0.

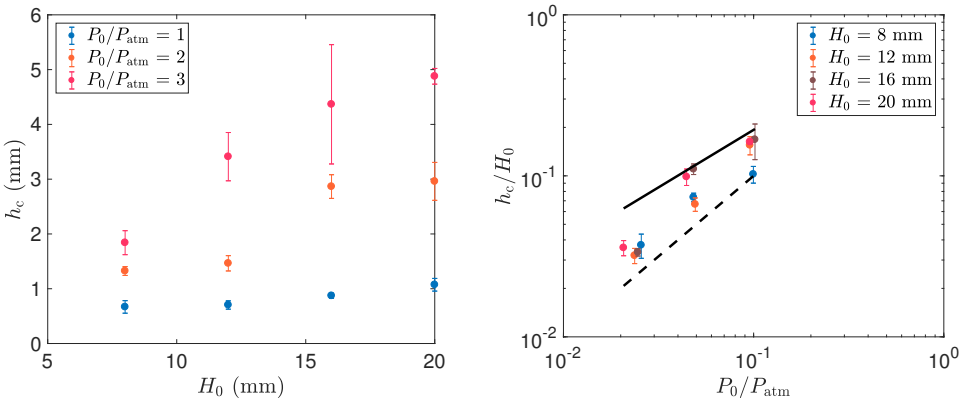

(a) (b)

FIGURE 2.16: (a): Experimental gas/vapor layer thickness h_c at $t_{U_{max}}$ as a function of the impact height H_0 for different initial pressure under the piston $P_{top,0}$. (b): Non-dimensional gas/vapor layer thickness as a function of the dimensionless pressure $P_{top,0}/P_{atm}$. Experimental data (o), adiabatic transformation (−) and isothermal transformation (−−).

The determined values of h_c in this case are between 0.5 to 5 mm, which are slightly higher than the values when $d = 0$ (see Figure 2.7a). As for the dimensionless representation of this quantity as a function of the dimensionless pressure, the experimental data presented in Figure 2.16b are less in accordance with an adiabatic compression of the gas/vapor layer than in the case of the fixed-bottom configuration (see Figure 2.7b).

2.3.3 Comparison between the fixed- and mobile-bottom configurations: effect on t_i

We can also resort to the use of wavelets for the qualitative analysis of the generated frequencies in the medium for a mobile lower piston configuration. Figures 2.17 show again that the impact height H_0 plays an important role on the resulting frequencies. Indeed, based on the same figures, a lower H_0 induces a tighter range of frequencies which are also lower in magnitude as compared to the fixed-bottom configuration.

Compared to Figure 2.11a in which we showed that the order of magnitude of the impact time t_i when $d = 0$ ranges from 0.2 to 1.6 ms, the order of magnitude of t_i when $d \neq 0$ is of 0.2 to 1.2 ms based on Figure 2.18a. We can say that the effect of the mobility of the reactor's bottom is minor on the characteristic time of the impact.

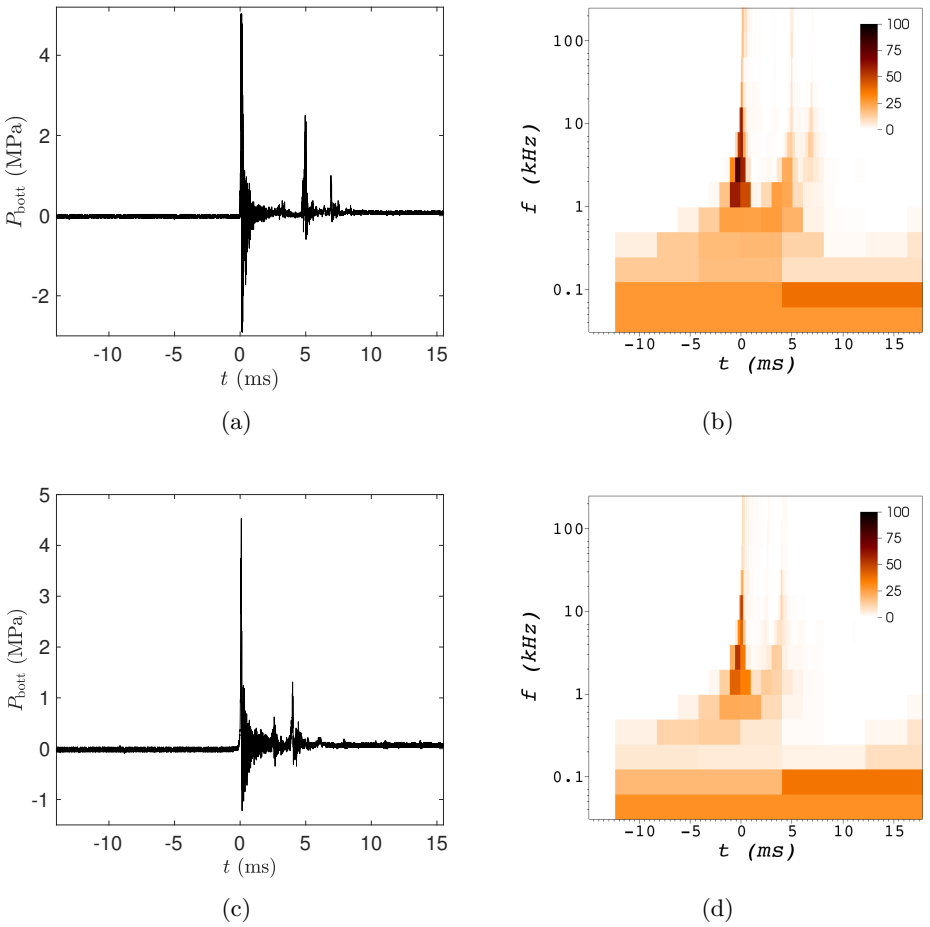

FIGURE 2.17: Left: Pressure signal at the bottom of the reactor obtained for $d = 10\,\text{mm}$ and $P_{\text{top},0}/P_{\text{atm}} = 1$. Right: Daubechies wavelet of the pressure signal presented in (a) and (c). Up: $H_0 = 20\,\text{mm}$ and Down: $H_0 = 8\,\text{mm}$. The color bar represents the absolute values of the wavelet coefficients, which represent a measure of the signal intensity.

Conclusion

Using high-speed camera visualizations and pressure measurements, three characteristic stages of the impact of a piston on the liquid free surface have been identified for both the fixed and the mobile bottom configurations: a) the *acceleration stage* defined as the time lag over which the piston is accelerated (pressure inside the chamber is lower than the reference pressure), b) the *compression stage* represented by the time lag between $t_{U_{max}}$ (end of the acceleration stage) and the instant when the pressure surge reaches its maximum value and c) the *rebound stage* characterized by a rebound of the piston after its impact on the liquid free surface due to a large excess of pressure forces acting below the piston.

We have identified two quantities of major importance to characterize the system response: the peak pressure reached during the impact and the characteristic frequency

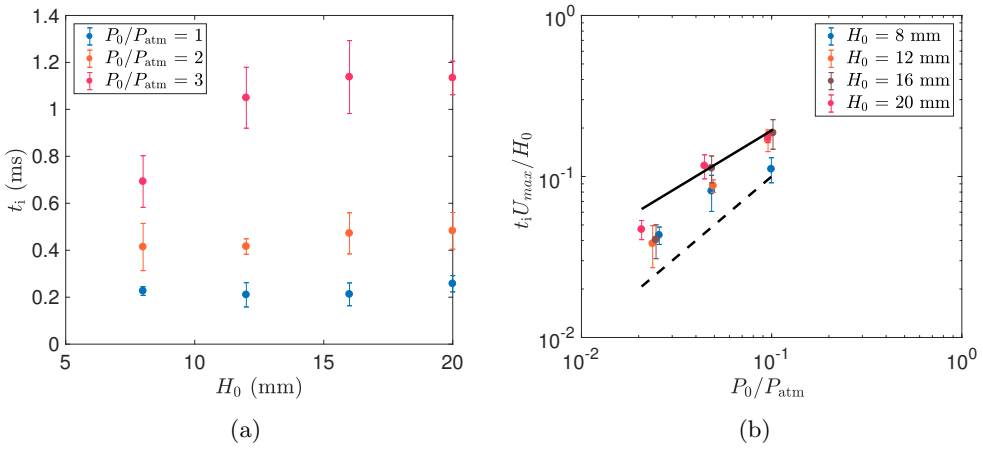

FIGURE 2.18: Left: Impact frequency f_i as a function of the impact height H_0. Right: Non-dimensional frequency $f_c H_0/U_{max}$ as a function of the dimensionless pressure $P_{top,0}/P_{atm}$. Experimental data (o), adiabatic transformation (−) and isothermal transformation (−−).

of the pressure transmitted to the liquid medium. The pressure peaks observed vary between 0.5 to 5 MPa depending on the impact velocity, the amount of water vapor trapped in a small gas/vapor layer under the piston and the mobility of the lower piston. Unlike techniques based on ultrasound, the new device efficiently transmits pressure to the liquid medium without any significant attenuation. Indeed the pressure can be assumed to be almost uniform in the liquid volume. The characteristic impact frequencies transmitted to the liquid medium have been shown to range between 0.5 to 5 kHz. These frequencies are of the same order of magnitude as the ones required to excite large pre-existing bubbles present in a volume of water. It is also worth noticing that due to the impact and subsequent bubble collapse, higher frequencies are also generated in the medium. Wavelet analyses reveal that frequencies above 100 kHz are also excited during very short instants after the impact of the piston. In this manuscript, no comparison between the tension values and literature are made since the captors are not adapted to tension measurements and therefore the analysis remains qualitative however this could be a field of future investigation.

Both the peak pressures and the impact frequencies are shown to depend on the amount of gas/water vapor trapped between the piston and the liquid free surface. As an analogy with the compression of gas/vapor bubbles in a bubbly liquid, we presented a simple model to correlate the initial internal pressure and the piston's maximum velocity based on a modified Joukowsky equation which accounts for the presence of the gas/vapor layer. The mobility of the bottom of the reactor had little influence on these parameters. Only the velocity of the rebound and the intensity of the secondary impact are significantly modified by making the bottom part of the chamber mobile.

Chapter 3

Bubble response to an impact of a piston on a liquid surface

Contents

In this chapter, we discuss the response of bubbles to the impact of a piston taking advantage of the fact that we can control the most relevant variables having a significant influence on the bubble collapse process such as the initial bubble radius distribution, the frequency of the excitation and its amplitude.

This chapter is structured as follows: in section 3.1, we introduce the definition of a bubble's critical radius which will be useful to further discussions. The behavior of bubble nuclei either bigger or smaller than the critical radius is included in sections 3.2 and 3.3 and in section 3.4, we develop the observed differences in bubble response when modifying the mobility of the reactor lower piston.

3.1 The bubble's critical radius R_c

The collapse of a bubble after a sudden increase of the surrounding/external pressure, i.e. the *background* pressure, is theoretically identified with the so-called Rayleigh collapse. Given a pressure difference between the initial bubble's internal (P_0) and external

pressures, $\Delta P = P_{\max} - P_0 \approx P_{\max}$, the time lag between the instants when the radius is maximum, $R_{\max}$ and minimum, $R_{\min}$ is given by the Rayleigh collapse time, t_{Rayleigh}. The analytic expression for t_{Rayleigh} was derived by Rayleigh in 1917[49],

$$t_{\text{Rayleigh}} = 0.915 \left(\frac{\rho_l R_{\max}^2}{P_{\max}} \right)^{1/2}. \tag{3.1}$$

Equation 3.1 can be deduced starting from the Rayleigh-Plesset equation in the absence of thermal effects, neglecting viscosity and surface tension terms and assuming that the liquid is incompressible and that the bubble remains spherical.

In a real application where the pressure increase in the system is not instantaneous, the response of the bubbles can be discussed in terms of the ratio between the characteristic time of pressure increase during the compression stage, t_c, and the bubble's characteristic collapse time t_{Rayleigh}. Thus, we define a critical bubble radius R_c as the radius for which $t_c = t_{\text{Rayleigh}}$, expressed as:

$$R_c = \frac{H_0}{1.884} \left(\frac{c_l^2 m_p}{H_0 S_p P_{\text{atm}}} \right)^{1/4} \left(\frac{P_{\text{top},0}}{P_{\text{atm}}} \right)^{1/\gamma}. \tag{3.2}$$

Typical values of the critical radius R_c are found to be of the order of 1 mm for the conditions reported in this manuscript. Accordingly, R_c is defined as a parameter to differentiate bubbles based on their size.

One of the advantages of the experimental set-up is that it gives place to bubbles of different sizes that we can analyze their response to the impact of the piston on the liquid's surface (bubbles are classified based on R_c). First, the liquid can contain micron-sized bubbles present in the bulk medium due to organic matter or impurities. These bubbles are activated when tension states occur. However, as the nuclei naturally present in the system are difficult to observe before their activation, in some of the experiments reported below, we resort to the generation of bubbles using water electrolysis to better study isolated bubbles of the size of a few microns. The response of this type of bubbles was part of the topics investigated in the PhD thesis of Elena Igualada[233] and was developed in our publication[2]. Note that as a consequence of the bubble generation technique, some changes were made to the experimental device presented in Chapter 2: a cathode and an anode are introduced inside the chamber in addition to a pulse generator which allows the control of the intensity and the number of pulses generated. For further details the reader is referred to Igualada[233]. The bubbles generated using this technique are of the order of 1 to 10 µm at the cathode[234]. Thus, the electrolysis- based experiments allows us to study the response of isolated bubbles with an initial size below the critical radius ($R_{\text{bub}} < R_c$).

Large bubbles or gas/vapor bags can also be trapped inside the liquid when the configuration of the reactor is modified to provide optical access to the bulk solution (see Figure 3.1). Thus, in this work we take advantage of this set-up modification to investigate the response of large gas/vapor bags with a characteristic size larger than R_c ($R_{bub} \geqslant R_c$).

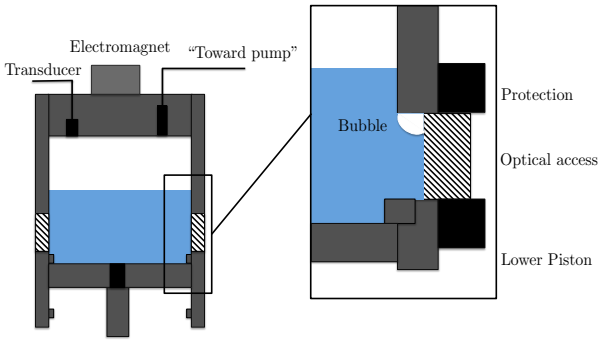

FIGURE 3.1: A sketch of a bubble trapped inside the liquid when the optical access is installed.

As a preliminary qualitative analysis of the behavior of big and small bubbles, Figures 3.2b and 3.2c present respectively the temporal evolution of small bubbles, i.e. $R_{bub} < R_c$ and of the pressure in the medium P_{top}, while Figure 3.2a presents the evolution of the radii of a bubble with an initial size larger than the critical threshold, $R_{bub} \geqslant R_c$ presented along with the pressure change under the piston.

As these figures show, bubbles with a characteristic size $R_{bub} \geqslant R_c$ implode during the first pressure peak generated during the piston impact. On the contrary, pre-existing bubbles with an initial radius smaller than R_c slowly compress during the initial *compression stage* due to the small characteristic compression time with respect to the fast bubble's response time. In this case, bubbles adapt to the pressure increase generated during the *compression stage* without undergoing any violent collapse during it. Only after the initial pressure peak, when pressure in the chamber decreases below the initial pressure ($t > 0.4\mu$s), the pre-existing bubble germs significantly expand and finally collapse. In the following sections we investigate in more detail the response of the system and the bubbles in each scenario.

3.2 The collapse of bubbles larger than the critical radius

Figure 3.3 shows a typical example of the different evolution stages of large bubbles before, during and after the piston impact where the impact height $H_0 = 14\,$mm, the

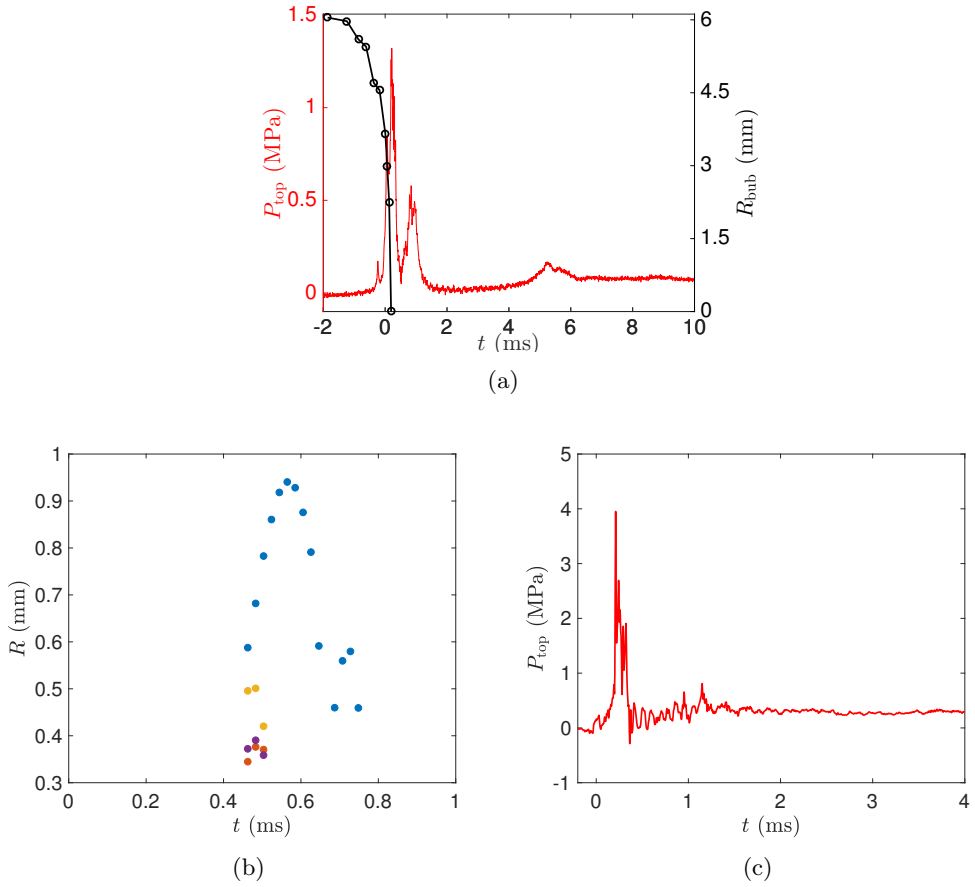

FIGURE 3.2: (a): Temporal evolution of the pressure under the piston P_{top} (in red) and the radius (in black) of a gas/vapor bubble which $R_{bub} \geqslant R_c$; (b): Temporal evolution of the radii of small bubbles detected in Figure 3.12; (c): Temporal evolution of the pressure under the piston P_{top} of the experiment presented in (b).

lower piston is fixed, i.e. $d = 0$ and the pressure under the piston at $P_{top,0}$ is equal to vapor pressure, i.e. $P_{top,0}/P_{vap} = 1$. It is noteworthy that these bubbles are typically not spherical, although we can still obtain the evolution of their size from the measurement of the projected area obtained from the images recordings, such that $S_{bub} = \pi R_{bub}^2$. The evolution of the bubble radius is determined by converting its vertical width into its characteristic size.

Based on Figure 3.3, we divide the dynamics of bubbles with $R_{bub} \geqslant R_c$ into two characteristic stages: the first stage consists of the primary collapse of the bubble due to the piston impact and the second stage includes the fragmentation of the bubble and cluster formation.

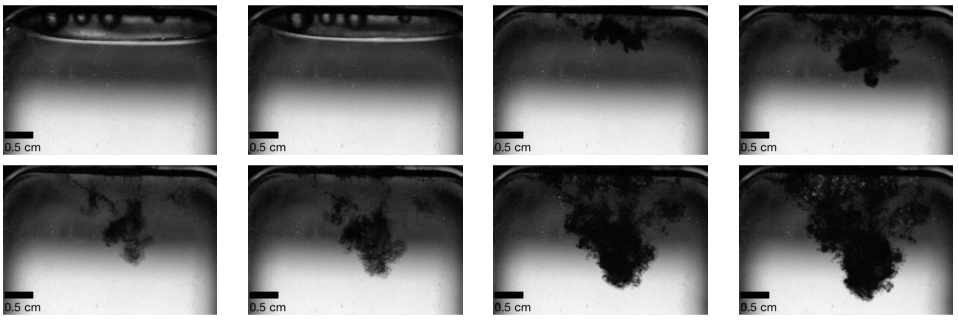

FIGURE 3.3: Example of the presence and collapse of big bubbles. $H_0 = 14\,\text{mm}$, $d = 0$ and $P_{\text{top},0}/P_{\text{vap}} = 1$. Frame rate: 16 087 fps and interframe time: 248 µs.

3.2.1 Primary collapse

We discuss herein the primary collapse of bubbles which radii are larger than the critical radius based on the typical example presented in Figure 3.3. We present different snapshots of this first stage in Figure 3.4 and Figure 3.5 presents the temporal evolution of the pressure under the piston P_{top} (in red) and the occurrence time of each image is marked by a black circle and a reference number.

We note that upon the first instances (Figure 3.4, from 1 to 4), the bubble remains unchanged ($t \lesssim 0\,\text{ms}$). Then, when the transducer starts to record a noticeable pressure increase around 0.05 ms (marker 5 in Figure 3.5), the bubble starts compressing, i.e. its radius shrinks (Figure 3.4, from 5 to 7). Recall that this pressure increase is due to the compression of the gas/vapor layer existing between the piston and the liquid's free surface. Finally, the bubble implodes and fragments forming a cluster of smaller bubbles when the piston hits the surface around 0.2 ms (Figure 3.4, snapshots 8 and 9).

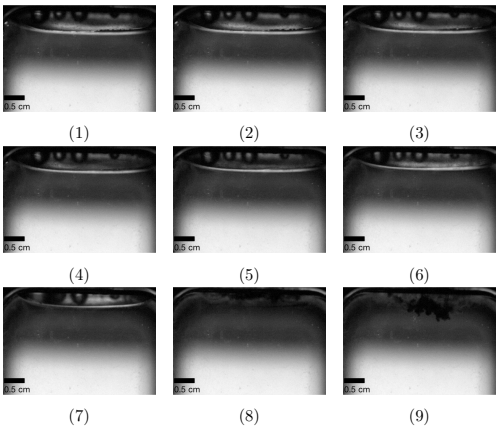

FIGURE 3.4: Primary collapse of big bubbles. $d = 0$, $H_0 = 14\,\text{mm}$ and $P_{\text{top},0}/P_{\text{vap}} = 1$. Frame rate: 16 087 fps and interframe time: 62 µs.

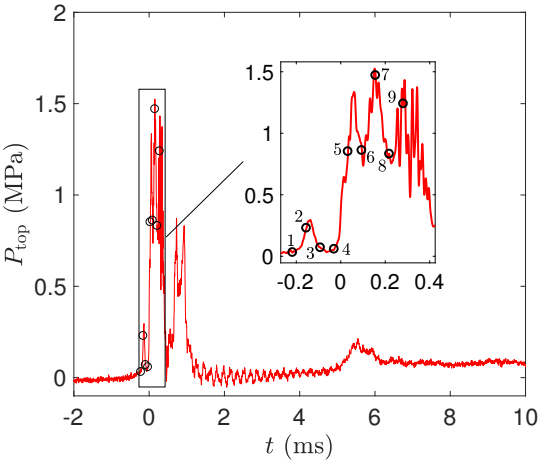

FIGURE 3.5: Temporal evolution of the pressure under the piston P_{top} for the cluster dynamic presented in Figure 3.4 on which the instants of each frame is reported in black circles.

Figure 3.6 presents the temporal evolution of the pressure under the piston, P_{top} and R_{bub} determined from the snapshots.

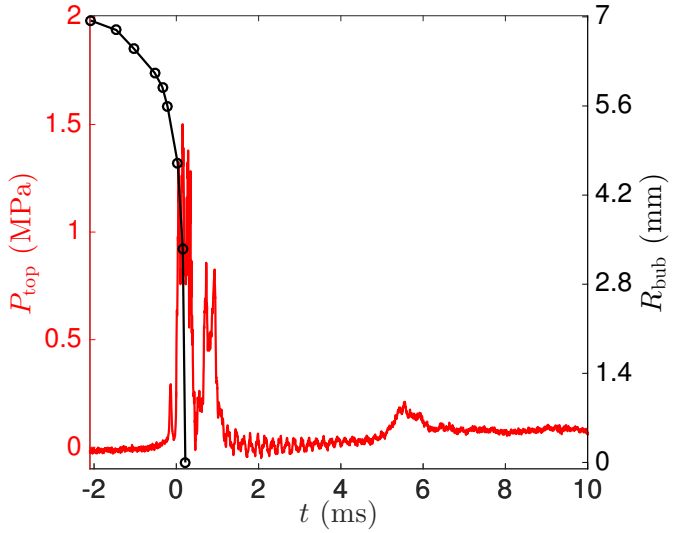

FIGURE 3.6: Temporal evolution of the pressure under the piston and the radius of the bubble presented in Figure 3.4.

As the evolution of R_{bub} shows , the compression of the bubble at its final stages (between 0 to 0.2 ms) is extremely fast due to the large pressure difference occurring between the bubble's interior and the *background* pressure generated during the impact. This is a consequence of the comparable characteristic response time of the bubble, t_{Rayleigh} and the impact time t_{i} creating an important pressure difference between the internal and external pressures of the bubble leading finally to a strong bubble collapse during the

compression stage. Further examples to show the reproducibility of these conclusions are presented in Appendix B.

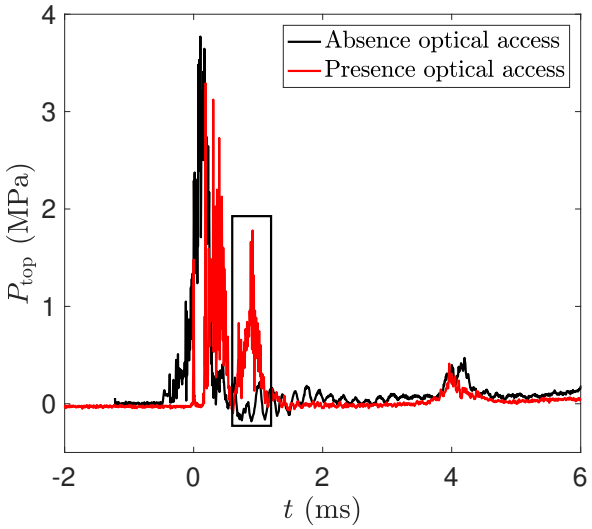

FIGURE 3.7: Temporal evolution of the pressure under the piston in the absence (in black) and the presence (in red) of the optical access for a typical example in which $H_0 = 18\,\text{mm}$ and $d = 0$. The shadowed region corresponds to a pressure peak related to the existence of big bubbles attached to the optical access.

It is also worth noticing the appearance of a secondary pressure peak of large amplitude which *systematically* appears when using the configuration in which the optical access is present (e.g. large bubbles are initially present in the system). Figure 3.7 compares the typical signals obtained for a fixed-bottom reactor in the absence (in black) and the presence (in red) of the optical access. Based on the shadowed region, when windows are absent (and also large bubbles), the appearance of the second peak is suppressed. It is then tempting to attribute the secondary pressure peak to the collapse of the large gas/vapor bags presented in the system, although the modification of the system geometry may also modify the response of the pressure evolution in the chamber. Further investigation about the correlation between the pre-existence of large gas/vapor bags and the appearance of the secondary pressure peak would be desirable.

3.2.2 Fragmentation and cluster dynamics

During the last instants of the primary collapse, two remarkable phenomena are observed in Figure 3.8: fragmentation and cluster formation. Fragmentation occurs when the bubble collapses. This phenomenon is usually identified with the development of a Rayleigh-Taylor instability[235]. The result of fragmentation is the formation of a cluster of small bubbles possessing its own dynamic response.

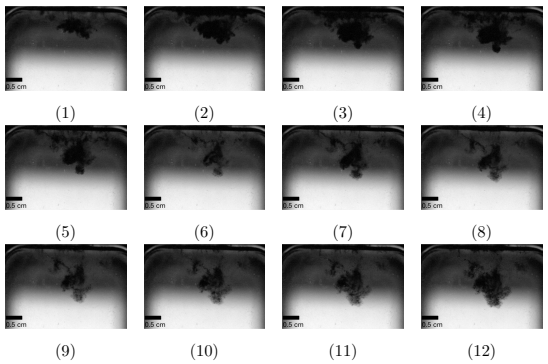

FIGURE 3.8: Fragmentation and cluster formation of big bubbles in a fixed bottom geometry. $H_0 = 14\,\text{mm}$, $d = 0$ and $P_{\text{top},0}/P_{\text{vap}} = 1$. Frame rate: 16 087 fps and interframe time: 62 µs.

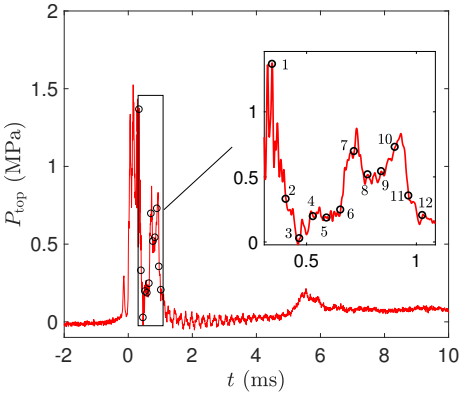

FIGURE 3.9: Temporal evolution of the pressure under the piston for the fragmentation and cluster formation presented in Figure 3.8.

Figure 3.9 shows the short-term temporal evolution of the pressure signal including references to the snapshots in Figure 3.8. Images 2 to 12 show that once the cluster is formed near the optical access, it starts a translational movement which creates micro-scale mixing and turbulence in the liquid. Indeed, the cluster detaches from its initial position and starts a descent trajectory induced by the high intensity mixing generated during the bubble collapse.

The dynamics of the cluster formed has a markedly longer response time than the single bubble. The dynamics at longer times are represented in Figure 3.10 which shows snapshots of the evolution of the bubble cluster. Figure 3.11 presents P_{top} as a function of time with the adequate snapshots references. Compared to Figure 3.8, we observe a densification of the cluster from images 1 to 5 (from $\approx$ 1.5 to 4 ms). This increase in the opacity of the cluster is due to the increase of the concentration of small bubbles. When looking at the occurrence of this volume augmentation in Figure 3.11, we see that it corresponds to a region in which the pressure is low and the frequency of pressure fluctuations is high meaning that it is possible to excite bubbles with large and high resonance frequencies (small radii). At $t \approx 5.5\,\text{ms}$, we observe another pressure peak (of lower intensity than the ones right after the impact) which we attribute to the characteristic *rebound stage* of the piston impact (see the violet highlighted region in Chapter 2, Figure 2.3). Thus, the cluster of bubbles feels an increase of the surrounding pressure which induces the collapse of very small bubbles.

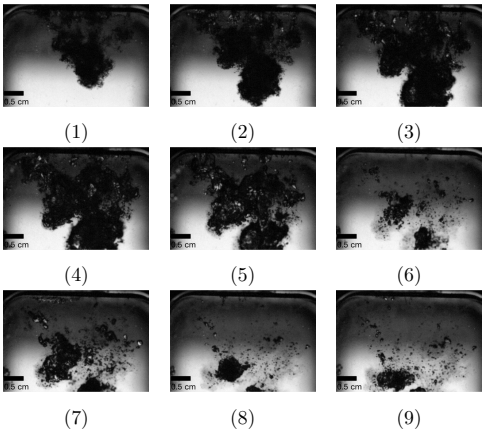

FIGURE 3.10: Cluster dynamics of big bubbles in a fixed bottom geometry. $H_0 = 14\,\text{mm}$, $d = 0$ and $P_{\text{top},0}/P_{\text{vap}} = 1$. Frame rate: 16 087 fps and interframe time: 622 µs.

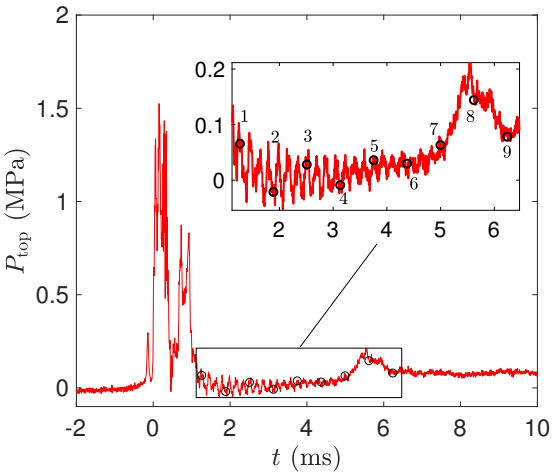

FIGURE 3.11: Temporal evolution of the pressure under the piston P_{top} for the cluster dynamic presented in Figure 3.10on which the instants of each frame is reported in black circles.

3.3 The collapse of bubbles smaller than the critical radius

Bubbles which radii R_{bub} are smaller than the critical radius R_{c} behave differently than the ones described in the preceding section. We already mentioned that small bubbles can be generated by electrolysis[2,233]. This allows us to isolate individual bubbles and follow their behavior after the piston impact. We can also study the behavior of small bubbles present naturally in the bulk solution due to the presence of nucleation sites.

We present in Figure 3.12 successive images of bubbles naturally activated in the system after the piston impact. We can see a "bigger" bubble compared to the rest. Thus, before developing further our discussion, we can note that the life-time of bubbles depends directly on the bubble radius.

Figure 3.13 presents the temporal evolution of the pressure under the piston, P_{top} for the experimental conditions presented in Figure 3.12, i.e. $H_0 = 8\,\text{mm}$, $d = 0$ and $P_{\text{top},0}/P_{\text{vap}} = 1$. We report on this figure the different instants corresponding to their respective images.

In contrast to the behavior of big bubbles, i.e. for which $R_{\text{bub}} \geqslant R_{\text{c}}$, bubbles much smaller than R_{c} (e.g. micron-sized bubbles) slowly compress during the initial *compression stage* due to the small characteristic compression time with respect to the fast bubble's response time (inversely proportional to the bubble's resonance frequency). Thus, bubbles with radii smaller than R_{c} follow and adapt to the pressure's increase

generated during the *compression stage* without undergoing any violent collapse during it.

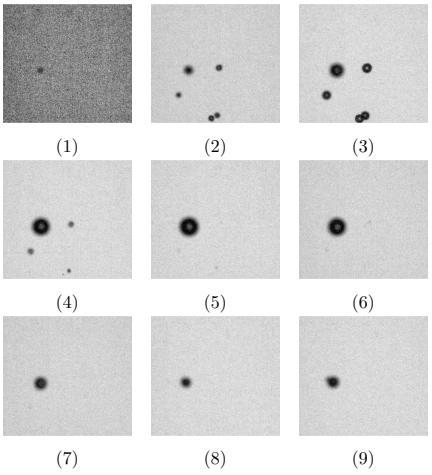

FIGURE 3.12: Example of the presence and collapse of bubbles in the medium. $H_0 = 8\,\text{mm}$, $d = 0$ and $P_{\text{top},0}/P_{\text{vap}} = 1$. Frame rate: 49 000 fps and interframe rate: 41 µs.

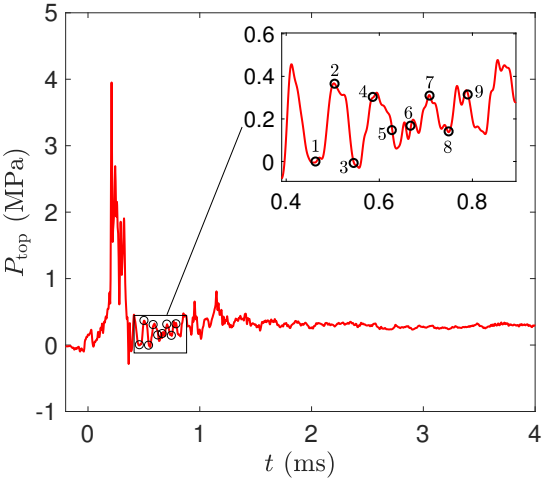

FIGURE 3.13: Temporal evolution of the pressure under the piston P_{top} for the bubbles presented in Figure 3.12 on which the instants of each frame is reported in black circles.

During the piston's *rebound stage*, negative pressures are generated in the liquid which correspond to tension states where small bubble nuclei expand significantly ($t \approx 0.3\,\text{ms}$). During this stage bubbles become large enough to be measured accurately using image processing techniques on the high-speed movie frames, which have a typical resolution of 4 microns/pixel. This makes it possible to extract the evolution of the radii of these bubbles from the recorded images (Figure 3.12). Bubble detection is carried out by applying a gray-level threshold to images once the background is removed with a rolling-ball algorithm. Subtracting the image background makes the area of the bubble images almost insensitive to the precise value of the threshold used. The bubble radii reported in this paper correspond to those of an equivalent circle with the same pixel area than the binary bubble image, S_{bub}, that is, $R_{\text{bub}} = \sqrt{S_{\text{bub}}/\pi}$. Figure 3.14 presents a representative example of the evolution of small germs. The maximum bubble radius obtained is usually between 100 µm and 1 mm. As predicted from the Rayleigh collapse time, the collapse time is directly linked to the maximum radius. Only for the largest bubble (around 1 mm) we observe a significant rebound that reveals the large pressures reached inside the bubble during the collapse. For smaller bubbles the limitations imposed by the resolution of the images impede to draw conclusions about the intensity of the impact.

In addition to the large pressures and temperatures locally reached, the collapse of bubbles can induce an important agitation at very small scales due to the formation of a liquid jet during the last instants of their collapse. Jet formation results from

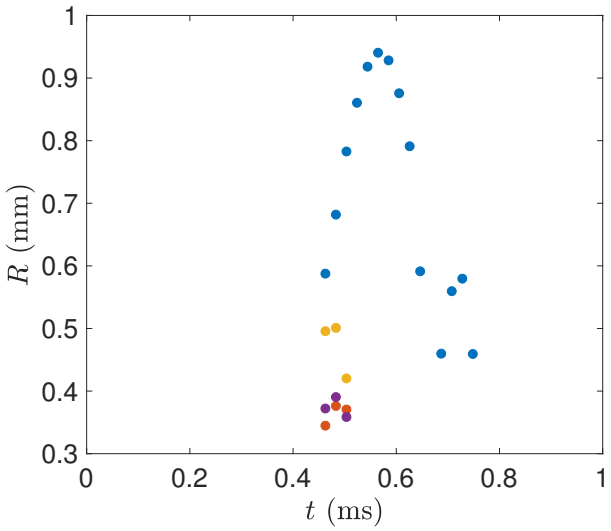

FIGURE 3.14: Temporal evolution of the radii of small bubbles detected in Figure 3.12.

asymmetries during the collapse induced by pressure differences across the cavity. Jetting is at the origin of surface damage in solid-liquid impact[92] and it is the result of an asymmetrical bubble implosion which contributes to surface damage (e.g. when the bubble collapses next to a solid boundary). Both the emission of shock waves and the high stresses induced by the liquid jet impact can damage the surface of solids. Another indirect consequence of jetting is a significant acceleration in their translational motion. It is noteworthy that not all bubbles lead to this phenomenon.

Figures 3.15, 3.16 and 3.17 show characteristic snapshots of the jet formation process during bubble collapse after the impact of the piston. This reveals the potential of the piston impact method to generate bubbles which act as small mixing sources during the last moments of the collapse. Note that the characteristic scales of the jet are below 1 mm.

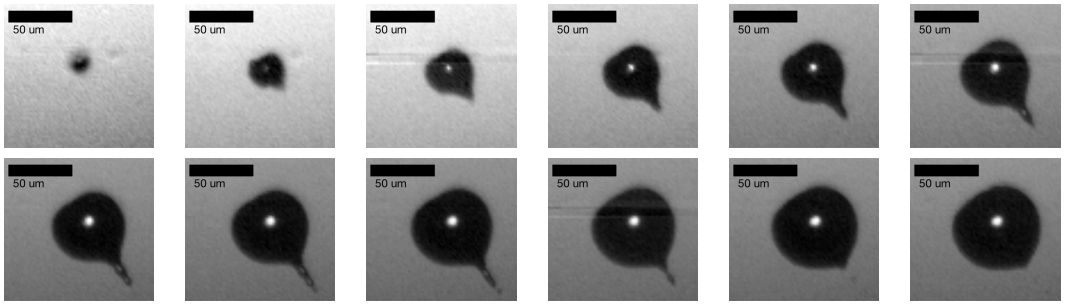

FIGURE 3.15: Snapshots during the collapse of a single bubble ($R_{max} = 79\,\mu m$) generated by electrolysis. During the strong collapse a jet is generated that induces a strong translational motion. Interframe time: 7 µs.

The average velocity of the jet can be determined from series of successive snapshots. We calculated the velocity as the ratio between the length difference of two successive images

of the jet and the inter-frame rate. Note that the jet length is the distance between the tip of the jet and the end of the bubble contour, i.e. the place of birth of the jet. The jet velocities calculated based on Figures 3.15, 3.16 and 3.17 are 0.7653, 0.5952 and 1.607 $\mathrm{m \cdot s^{-1}}$ respectively. Some previous studies in the literature investigated the effect of newtonian and non-newtonian liquids on the jet formation[236,237], showing that jets have an impact on the instability patterns of cylindrical jets[238]. Brown and Williams[237] studied the effect of the addition of the polyacrylamide (PAA) to a newtonian liquid made of syrup and water. The liquid jet velocities reported for the newtonian fluid varied from 4 to 6 $\mathrm{m \cdot s^{-1}}$. Upon the addition of 100 ppm of PAA, the jet velocities were 1.5 times smaller.

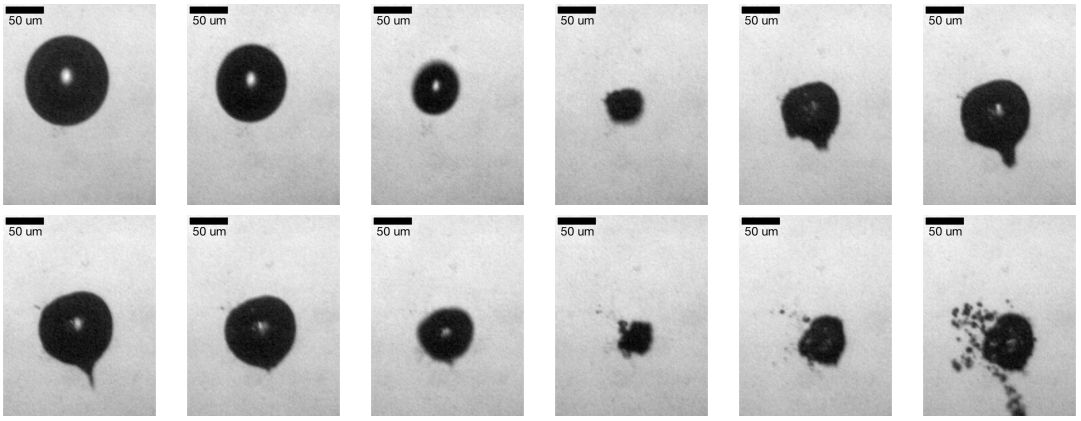

FIGURE 3.16: Snapshots during the collapse of a single bubble ($R_{\max} = 62\,\mu\mathrm{m}$) generated by electrolysis. During the strong collapse a jet is generated that induces a strong translational motion. Interframe time: 15 µs.

We can then conclude that despite the low impact velocities used in this work (of the order of 5 $\mathrm{m \cdot s^{-1}}$), the current technique is able to generate jets during the collapse of bubbles with velocities comparable in orders of magnitude to those reported by Brown and Williams[237]. In general, the presence of a source of asymmetry, as for example solid walls or the presence of surrounding bubbles, may also significantly modify the maximum jet velocities reached during the impact[239].

3.4 The impact of the lower piston mobility on the bubble dynamic response

We saw in Chapter 2 that the system response is slightly different depending on the mobility of the lower piston of the reactor. After having developed in the previous chapter the effect it has on the generated pressures and frequencies in the medium, we discuss herein some differences observed on the bubble response.

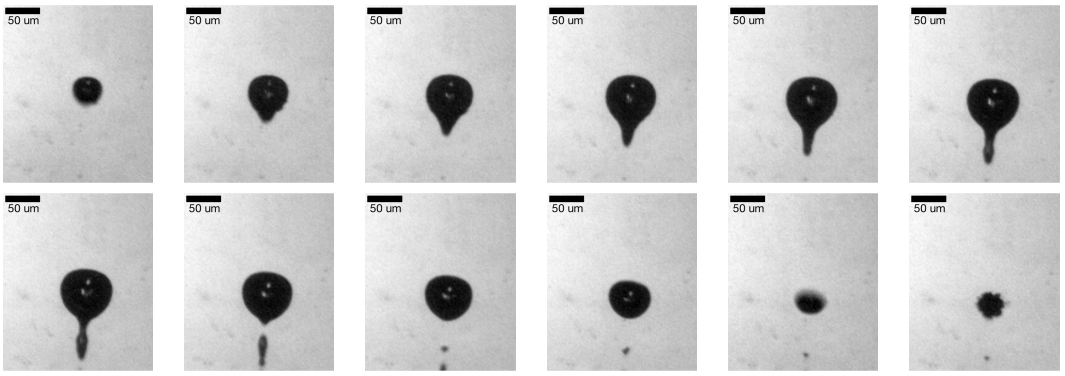

FIGURE 3.17: Snapshots during the collapse of a single bubble ($R_{max} = 154\,\mu m$) generated by electrolysis. During the strong collapse a jet is generated that induces a strong translational motion. Interframe time: 10 µs.

3.4.1 Response of bubbles with $R_{bub} \geq R_c$

In section 3.2, we described the behavior of bubbles which radii are greater or equal to the critical radius R_c. Herein, we develop the observed differences in the collapse time of these bubbles when the lower piston is mobile, i.e. $d \neq 0$.

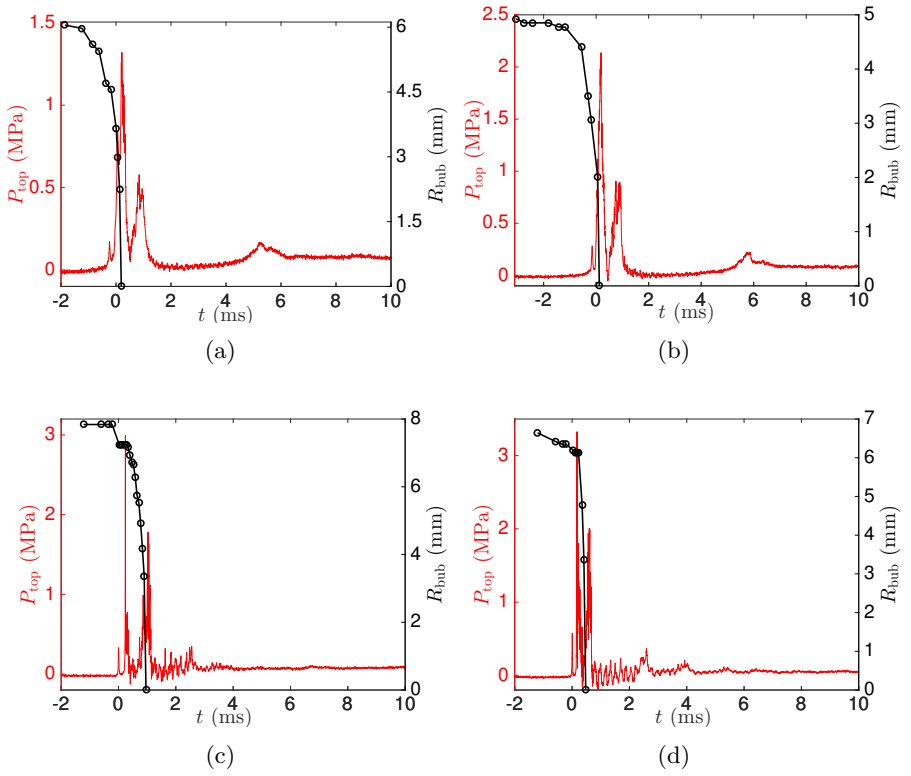

FIGURE 3.18: Temporal evolution of the pressure under the piston (red line) and the bubble's size, R_{bub} (black line) for cavities with initial radii of the order of the critical radius given by Equation 3.2 at $P_{top,0}/P_{vap} = 1$. (a) and (b): $H_0 = 10$ and 16 mm, $d = 0$; (c) and (d): $H_0 = 10$ and 18 mm, $d \neq 0$.

Figure 3.18 shows four different examples of the temporal evolution of the pressure in the reactor, P_{top} (in red) and the bubble's radius, R_{bub} (in black). Figures 3.18a and 3.18b are examples of the pressure evolution obtained for a fixed bottom ($d = 0$) and an impact height $H_0 = 10$ and 16 mm, whilst Figures 3.18c and 3.18d are obtained for $d \neq 0$ and $H_0 = 10$ and 18 mm respectively.

Independently of d, large bubbles - whatever their exact initial size is - start their compression before the impact of the piston due to the compression of the gas/vapor layer. The appearance of the second peak related to the presence of large bubbles (set-up with optical access) is confirmed for the mobile bottom configuration (see shadowed region in Figure 3.19). Remarkably, when the lower piston is mobile ($d \neq 0$), bubbles implode *during the second pressure peak* (see Figure 3.18b and 3.18d). The fact that the time difference between the two pressure peaks is variable from experiment to experiment seems to provide further evidence about the correlation between the initial size of pre-existing bubbles (which unfortunately could not be controlled) and the appearance of a secondary pressure peak of large amplitude. Further examples are given in Appendix B.

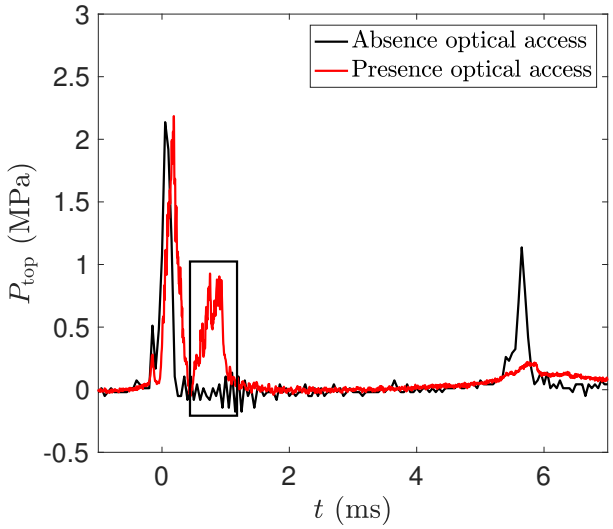

FIGURE 3.19: Temporal evolution of the pressure under the piston in the absence (in black) and the presence (in red) of the optical access for a typical example in which $H_0 = 18$ mm and $d \neq 0$. The shadowed region corresponds to a pressure peak related to the existence of big bubbles attached to the optical access.

In Figure 3.20 we present the evolution of a large bubble for a typical example in which the impact height is equal to $H_0 = 10$ mm, $P_{\text{top},0}/P_{\text{vap}} = 1$ and for $d \neq 0$. We can again divide the behavior into the two characteristic stages detailed in section 3.2. We present in Figure 3.21 the evolution of the pressure under the piston P_{top} for the experiment presented in Figure 3.20 and we report on it the instants of each frame (presented in black circles). The overall evolution of the bubble, from its primary collapse to its fragmentation and cluster response is very similar to when $d = 0$.

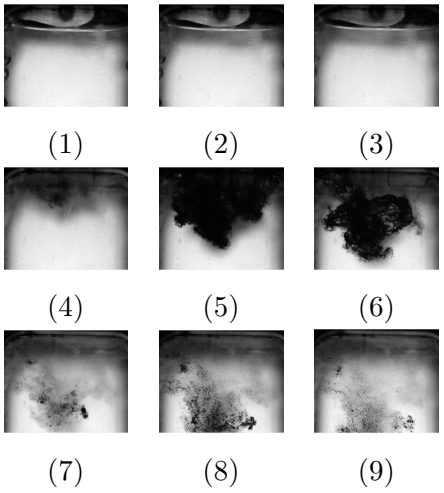

FIGURE 3.20: Cluster dynamics of large bubbles in a mobile bottom geometry. $H_0 = 10\,\text{mm}$ and $P_{\text{top},0}/P_{\text{vap}} = 1$. Frame rate: 16 087 fps and interframe time: 622 µs.

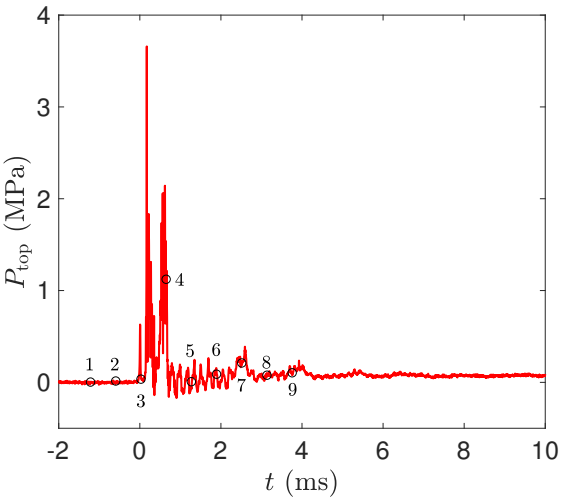

FIGURE 3.21: Temporal evolution of the pressure under the piston P_{top} for the experiment presented in Figure 3.20 on which the instants of each frame is reported in black circles.

3.4.2 Response of bubbles with $R_{\text{bub}} < R_{\text{c}}$

Herein, we compare the behavior of bubbles smaller than R_{c} when the lower piston is mobile. Note that for the series of experiments below, **no** electrolysis technique was used, so the number of bubbles activated during the impact is directly related to the presence of pre-existing nucleii.

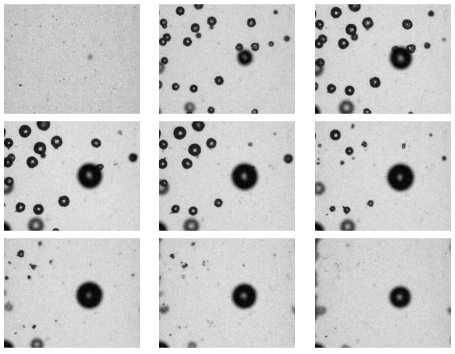

FIGURE 3.22: Example of the presence and collapse of bubbles in the medium. $H_0 = 8\,\text{mm}$, $d \neq 0$ and $P_{\text{top},0}/P_{\text{vap}} = 1$. Frame rate: 49 000 fps and interframe rate: 102 µs.

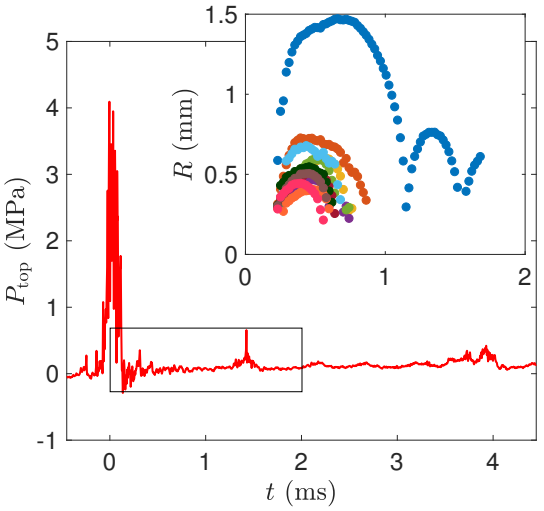

FIGURE 3.23: Temporal evolution of the pressure under the piston P_{top} for the experiment presented in Figure 3.22 on which the instants of each frame is reported in black circles.

Figure 3.22 presents snapshots of bubbles recorded for an impact height $H_0 = 8\,\text{mm}$, $d \neq 0$ and $P_{\text{top},0}/P_{\text{vap}} = 1$ while Figure 3.23 presents the evolution of the pressure P_{top}, an inset which delimits the zone of appearance of the bubbles and an inset of the evolution of the radii of the different bubbles detected in Figure 3.22. The first observation made is that for a mobile bottom configuration, we obtain more bubbles per unit volume compared to the configuration where the lower piston is fixed. Table 3.1 presents the bubble density in the medium through a typical example for which the impact height, $H_0 = 12\,\text{mm}$ and for both lower piston configurations. The bubble density is defined as the maximum number of detected bubbles per unit surface. This is estimated over sufficient number of repetitions (see Table 3.1) to ensure the statistical convergence. We show that bubbles are much more present when the bottom of the reactor is mobile than when it is fixed showing that the first configuration is more interesting to activate nuclei.

Lower Piston	**Impact height** (mm)	**Bubble density** (bubbles/mm^2)
Fixed	12	0.021
Mobile	12	0.057

TABLE 3.1: The density of bubbles in the medium for different impact heights and lower piston configurations.

When a tension state occurs, small bubbles are unable to adjust their pressure to the *background* pressure and their size increases by at least one order of magnitude. Bubbles finally collapse when the system pressure is recovered undergoing a series of rebounds until the bubble pressure re-equilibrates with the surrounding pressure. Since the intensity of the waves decays in time, the first expansion-collapse is the most violent. Unfortunately, the framerate of the high speed camera is insufficient to estimate the bubble collapse velocities immediately prior to minimum radius.

The radii evolution inset presented in Figure 3.23 shows that a bubble rebound is observed only for the largest bubble. Smaller bubbles detected between 0.5 and 1.5 ms are more difficult to follow over longer periods of time because of the frame rate conditions and the rapidity of their collapse. Indeed, the smaller the bubble the faster its oscillation frequency, which establishes a limit in size below which is no longer possible to well resolve the rebound. In any case, we can say that these bubbles which maximal radius is lower than 1 mm appear and quickly disappear after the main pressure peak around 0 ms. The largest observed bubble has a long lifetime and feels the small pressure increase observed around 1.4 ms, which is of the order of the time at which the secondary pressure peak appears. That is, bubbles with long life-times experience a significant increase of the background pressure induced by the secondary impact of

the piston. In this case, we expect the collapse of the bubbles to be stronger than for bubbles having a life-time shorter that the rebound time of the piston. It is noteworthy that the pressure-tension spike features observed in the inset in Figure 3.23 and the corresponding bubble behavior occur at approximately the same time. Furthermore, we can determine from the Rayleigh-Plesset equation an experimental pressure difference based on the radii evolution which in this case was determined to be around 0.1 MPa which is in accordance with the pressure-tension spike values.

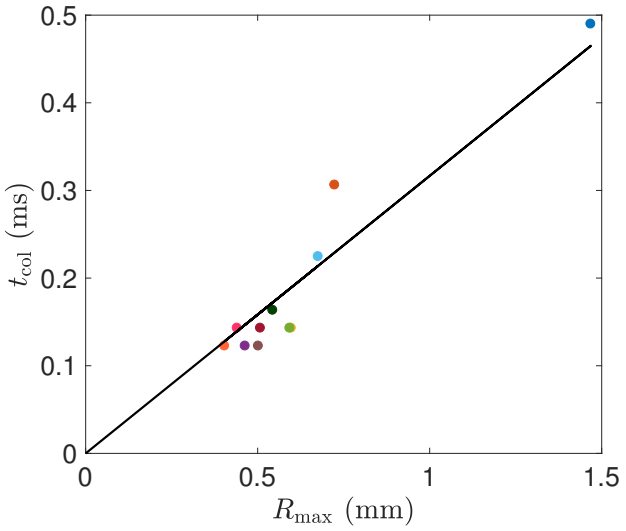

FIGURE 3.24: The collapse time t_{col} as a function of R_{max}. $H_0 = 16\,\text{mm}$ and $d \neq 0$.

In Figure 3.24, we represent the collapse time t_{col} as a function of the maximal radius R_{max}. Recall that t_{col} is defined as the difference between the moment at which the radius is maximal R_{max} and the time of the first rebound. The slope of the experimental fit presented in a black continuous line on Figure 3.24 is equal to $0.3167\,\text{s}\cdot\text{m}^{-1}$. According to Equation 3.1, t_{col} and R_{max} are related theoretically by a factor equal to $0.915\left(\frac{\rho_l}{P_{max}}\right)^{1/2}$. This allows us to calculate the effective maximal pressure felt by the bubbles which we call P_{max}^{eff}. The calculated value of P_{max}^{eff} is of the order of 10 kPa. Such rapidly growing and collapsing bubbles could, in principle, give rise to a hydrodynamic pressure wave contribution to the pressure record.

Summary

This chapter describes the dynamic response of bubbles present in a liquid after the impact of a piston on the liquid free surface. Using high-speed camera visualizations, we show that bubbles initially present in the medium behave differently depending on their size.

Based on the ratio between the characteristic compression time related to the compression of the gas/vapor layer below the piston and the Rayleigh collapse time of the bubble, we find a critical radius that depends on the impact velocity and both the initial and the reference pressures. During the initial pressure peak induced by the impact of the piston, bubbles smaller than this critical radius (of the order of millimeters in our conditions) tend to follow the system's pressure evolution and compress slowly, whereas bigger bubbles collapse violently. In the rebound stage, tension occurs and small bubbles expand and collapse at later times.

In general, the collapse of bubbles present in the medium creates an important agitation at very small scales (of the order of microns) and can generate hydrodynamic pressure waves which can contribute to pressure records.

Table 3.2 summarizes the impact of the physical parameters (noted as input) related to the experimental set-up have on the response of the medium and the variables determined in Chapters 2 and 3 (noted as output). Note that for each input variable the rest of the inputs are constant and that comparable means that the effect is negligible. This parametric study allows to better define the optimal parameter for a more developed physical and/or chemical studies.

Input \ Output	$f_{\max}$	t_{i}	$P_{\max}$	h_{c}	Bubble population
H_0	increases	increases	increases	comparable	increases
$P_{\mathrm{top},0}$	decreases	increases	decreases	increases	-
d	comparable	comparable	comparable	increases	increases

TABLE 3.2: Summary table of the impact of the physical parameters on the medium response to the piston impact.

The possibility to use this process to promote chemical and physical processes on complex systems containing two or more phases (solid/liquid/gas) is investigated in Chapter 4.

Chapter 4

An example of a chemical process induced by plate-impact cavitation: phenol oxidation

Contents

In Chapter 1, we described different applications which resort to bubbles - excited by ultrasounds - as micro-reactors. The various types of reactions studied in the context of sonochemistry can be potentially investigated using the experimental set-up presented in this manuscript. Among all of them, we chose the oxidation of phenol as a model reaction due to its direct application in waste water treatment studies and given its wide study in literature.

The objective of this chapter is twofold: a) to evaluate the potential of technologies based on piston impact to induce chemical reaction processes and b) to gain further insight into the influence of the various design parameters of the set-up on the chemical activity induced in the reactor after a series of impacts. Given that we showed that the response of the medium (and also the bubbles) in different conditions can be controlled, it is

interesting to evaluate if these changes are going to have an impact on the performance of the equipment when trying to intensify/promote a chemical reaction.

This chapter is structured as follows: we present in section 4.1 the viability of the plate-impact technology to induce radical formation in water. In sections 4.2 and 4.3 we briefly present the experimental procedure, the role the hydrogen peroxide plays in the reaction, the analysis system and some preliminary results. We finally discuss the role played by different physical parameters on the chemical reaction in a fixed-bottom geometry (section 4.4) and in the mobile configuration (section 4.5).

4.1 Viability of the current technology to induce radical formation in water

It is well-known in literature that a chemical reaction can take place in the presence of collapsing bubbles[63,65,66]. In acoustic cavitation applied to water treatment, it is accepted that the nature of the organic pollutants strongly influences their ultrasonic degradation[128]. Recall that hydrophobic and/or volatile compounds degrade mainly inside the bubble due to direct thermal decomposition whereas hydrophilic compounds like phenol tend to degrade in the bulk solution and/or at the bubble interface. This latter decomposition is generally linked to the formation of radical species, mainly hydroxyl radicals.

$HO^\bullet$ radicals are the product of the homolytic cleavage[a] of water molecules (see Equation 4.1) trapped inside the bubble[93,94]. Indeed, when the bubble grows due to medium depressurization for example, gas and vapor diffuse into it. Its collapse can generate high temperatures locally and thus lead to bond breaking.

$$H_2O \xrightarrow{\Delta} H^\bullet + HO^\bullet \tag{4.1}$$

To probe the formation of $HO^\bullet$ in pure water under cavitation conditions, we used the Weissler reaction. This quantification method is based on the oxidation of iodide I^- into iodine I_2 or triiodide I_3^- (when I^- is in excess)[98]. This method is therefore a good indicator of whether hydroxyl radicals are generated in the medium.

The oxidation of a $0.1\,\mathrm{mol}\cdot\mathrm{L}^{-1}$ iodine solution subjected to an impact height H_0 equal to 20 mm, a number of impacts $N = 500$ impacts in both fixed and mobile configurations

[a] When the two electron pair making- up a covalent bond split equally between the products, the process is qualified as homolytic, whereas in the opposite case, i.e. an unequal distribution of an electron pair is called a heterolytic cleavage which would give H^+ and HO^-.

is tested. The volume of the solution is varied from 30 to 220 mL in the presence of big and small bubbles. We referred to the color change method to detect if the reaction took place. The experimental protocol is established in Appendix C, section C.1. Note that 500 impacts take almost 2 h to be done

The experimental results (not presented here) show *a priori* no sign of triiodide formation. Indeed, no color change is observed for the different combinations of the experimental conditions. Thus, as $HO^{\bullet}$ is not evidenced in the standard impacting conditions tested in this work, the role of the parameters determined in Chapter 2 on radicals formation was not further examined and the use of external additives is hence necessary.

4.2 Experimental procedure - The role of H_2O_2

The literature review presented studies that show that the use of solid catalysts[240] or other technologies[129] such as ultraviolet irradiation is interesting for enhancing chemical reactions in the presence of cavitation bubbles. To increase the $HO^{\bullet}$ population and the efficiency of the water treatment process - especially when degrading hydrophilic compounds - the addition of oxidants is interesting. Indeed, the addition of gaseous[102] or liquid[100] additives enhance oxidation reactions. For example, the combination of hydrogen peroxide H_2O_2 to acoustic cavitation gives rise to synergistic effects which promote chemical oxidation reactions[128]. We briefly developed the role played by these molecules as well as their occurrence site in Chapter 1. Note that the dissociation energy of the O−H bond in a water molecule H_2O is equal to $498\,\mathrm{kJ \cdot mol^{-1}}$ which is twice the dissociation energy of the O−O bond in a hydrogen peroxide molecule H_2O_2. This implies that thermodynamically, H_2O_2 molecule can be more readily cleaved compared to water.

The oxidation of phenol is a complex reaction. Many intermediates can be formed depending on the reaction mechanism[241–243]. Independently of this latter, the overall reaction between phenol and hydrogen peroxide is written as:

$$C_6H_5OH + 14\,H_2O_2 \longrightarrow 6\,CO_2 + 17\,H_2O \tag{4.2}$$

Table 4.1 presents the physical parameters which include: H_0 the impact height, N the number of impacts and d the mobility of the lower piston of the reactor. Note that the temperature, equal to room temperature and the pH were not controlled.

As for the chemical parameters we define:

- $C^{reactor}_{C_6H_5OH}$ the concentration of phenol in the reactor in $\mathrm{mol \cdot L^{-1}}$;

$\boldsymbol{H_0}$ (mm)	$\boldsymbol{N}$ (impacts)	$\boldsymbol{d}$ (mm)
8, 12, 16 and 20	up-to 500	mobile or fixed

TABLE 4.1: Experimental conditions: the physical parameters.

- $V_{H_2O_2}$ the volume of hydrogen peroxide added to the solution of phenol in mL;
- $C_{H_2O_2}^{reactor}$ the concentration of hydrogen peroxide in the reactor in $mol \cdot L^{-1}$;
- V_{tot} the total volume of the mixture of the phenol and hydrogen peroxide solutions in mL.

The detailed protocol for the solution preparation is presented in Appendix C.2 and we present in Figure 4.1 a summary sketch. In brief, a mother solution of $0.01\,mol \cdot L^{-1}$ phenol is prepared and split into two unequal daughter solutions. The desired volumes of water and hydrogen peroxide are added to the first solution which we call *Mixture 0* and note in the following M_0. The total volume of this first solution is equal to $V_{tot} = 170\,mL$ and its concentration in phenol, i.e. the concentration of phenol in the reactor is equal to $C_{C_6H_5OH}^{reactor} = 0.0082\,mol \cdot L^{-1}$. To the second solution **only** water is added to obtain the same final phenol concentration. We call this solution *Phenol alone* and represent it as Ph_0.

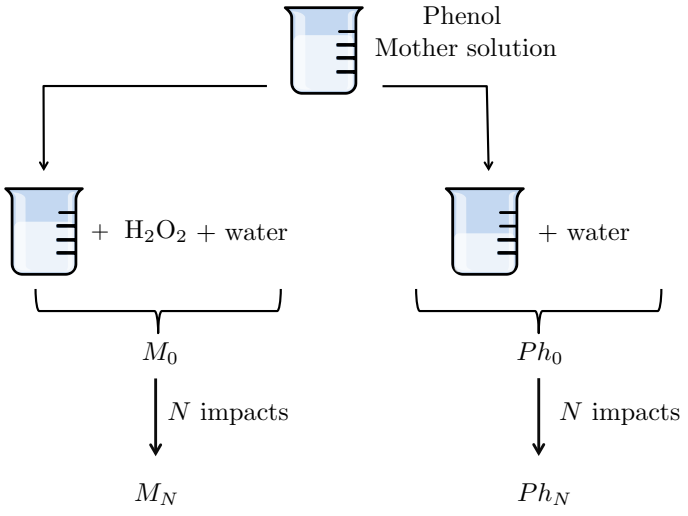

FIGURE 4.1: Sketch of the experimental solutions prepared and withdrawn before or after the impacts.

Table 4.2 presents the common quantities of the chemical parameters. According to Equation 4.2, $V_{H_2O_2}^{stoech} = 2\,mL$ however, we chose to start with a $V_{H_2O_2} = 19.5\,mL$, i.e. in a large excess compared to stoichiometry. The reason behind this choice relies on the experimental conditions presented in literature concerning the oxidation of organic

molecules which show unanimously that the oxidation of the molecule depends not only on the concentration of the oxidant, but also on the frequency of the transducer, the acoustic power, etc.[106,107] and therefore to maximize the chance of observing some chemical activity we chose to work in an excess of oxidant. Nevertheless, the role played by this parameter is investigated herein.

$\boldsymbol{C}^{\boldsymbol{reactor}}_{\mathrm{C_6H_5OH}}$ $(\mathrm{mol \cdot L^{-1}})$	$\boldsymbol{V_{H_2O_2}}$ (mL)	$\boldsymbol{C}^{reactor}_{\mathrm{H_2O_2}}$ $(\mathrm{mol \cdot L^{-1}})$	$\boldsymbol{V_{tot}}$ (mL)
0.0082	19.5	1.123	170

TABLE 4.2: Experimental conditions: the chemical parameters.

Note that after undergoing N impacts in the reactor, *Mixture 0* and *Phenol alone* are noted M_{N} and Ph_N respectively. Hence, when M_0 undergoes $N = 100$ impacts, its noted M_{100}. Table 4.3 summarizes the names and the characteristics of the different solutions.

Solution Name	**Abbreviation**	**Description**
Phenol alone	Ph_0	$\mathrm{C_6H_5OH}$ solution at $t = 0$
Phenol alone after N impacts	Ph_N	Ph_0 after N impacts
Mixture 0	M_0	$\mathrm{C_6H_5OH}$ and $\mathrm{H_2O_2}$ mixture at $t = 0$
Mixture after N impacts	M_{N}	M_0 after N impacts

TABLE 4.3: Summary table of the different types of solutions.

4.3 Analysis systems and preliminary results

4.3.1 Gas Chromatography

The principle of the Gas Chromatography (GC) technique is detailed in Appendix D, section D.1. Briefly, GC relies on the introduction of a mixture (liquid or gas) into an injector which will then be transported through a column. Depending on its affinity with the compounds, the column separates them. The separated molecules pass by a detector which generates a signal recorded in a chromatogram and representing the area of the molecule at a specific time (constant under the analysis conditions). An example of the $\mathrm{C_6H_5OH}$ chromatogram is shown in Appendix D, Figure D.2.

The peak area of a species x ($Area_{\mathrm{x}}$) is related to its concentration C_{x} in the medium according to:

$$Area_{\mathrm{x}} \;=\; k_{\mathrm{x}} C_{\mathrm{x}},$$

where k_x is the response factor. To determine k_x, an internal or external standard [b] can be added to the solution before the reaction or the injection into the column respectively. In this work, we used the method based on external calibration with a standard curve.

Following the experimental protocol presented in Figure 4.1, a fresh solution of Ph_0 of $0.0082\,\mathrm{mol}\cdot\mathrm{L}^{-1}$ was injected in the column. Then the phenol solution is left at room temperature and analyzed periodically on a period of time similar to the one used in the cavitation experiment. The evolution in time of the phenol peak area is presented in Figure 4.2 in blue. Note that the values are calculated based on four different experiments. This first result shows that Ph_0 is stable during the time of the analysis.

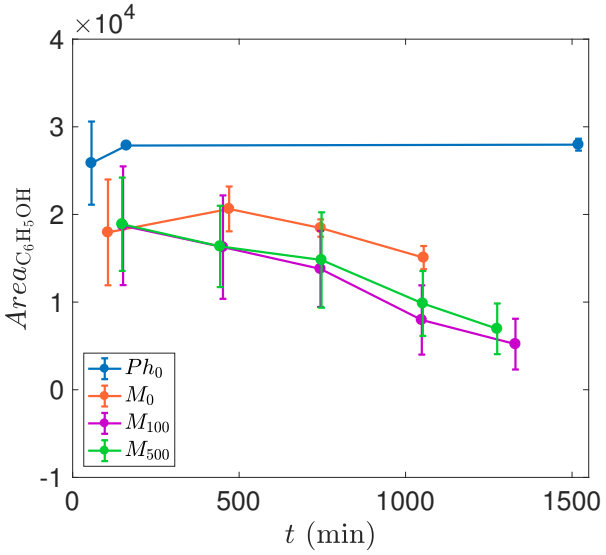

FIGURE 4.2: Phenol peak area $Area_{C_6H_5OH}$ as a function of time for the different solutions listed in Table 4.3.

To the rest of the prepared solutions, hydrogen peroxide and water are added (see Table 4.2) before doing 100 impacts followed by 400 more (total of 500 impacts) at $H_0 = 20\,\mathrm{mm}$ in a fixed bottom configuration. The average values of $Area_{C_6H_5OH}$ for the different solutions are presented in Figure 4.2. Note that when the aliquots are withdrawn from the reaction medium after finishing the impacts, they are kept in vials at room temperature and in the light.

The experimental data show a decrease of the phenol area between Ph_0 on one hand and the rest of the solutions on the other at the first injection. This is due to the fact that the mixture is introduced in the injector at 280 °C (see Appendix D, section D.1) whereas the temperature at which hydrogen peroxide decomposes ranges from 150 to 152 °C[244].

[b] This addition consists of referencing the analyte signal to a signal from another species which is added to the solution. Accordingly, this species must be different from the analyte and should not interfere in the reaction or in the retention time of the target molecule.

Accordingly, as H_2O_2 is decomposed in the injector, it is able to react with the phenol molecules before entering the separation column under the only effect of temperature. Nevertheless, the results can still be analyzed qualitatively. We can see that M_0 is stable up-to $\approx 1000\,\text{min}$ and that the impacts of the piston affect the oxidation reaction since M_{100} and M_{500} solutions show both a decrease in the phenol area compared to M_0. In addition, it seems that the number of impacts does not affect the solution. This conclusion is discussed later on and should be taken carefully due to the dissociation of the molecules in the injector.

Since the GC method is not fully satisfying for the tested experimental conditions, an alternative analytical method is used to determine the composition of the medium in phenol.

4.3.2 UV-visible spectroscopy

The ultraviolet-visible (UV-visible) technique is relatively simple. Its principle is presented in Appendix D, section D.2. The UV-visible method, allows among other to:

1. Record the absorbance spectrum of a species x resulting in a $A = \text{f}(\lambda)$ spectrogram;
2. Record the value of the absorbance at the maximal wavelength λ_{max}. For phenol, $\lambda_{\text{max}} = 270\,\text{nm}$.

UV-visible is based on the Beer-Lambert law which states that at a given wavelength λ, the absorbance A of a diluted mixture of n absorbing species is equal to the sum of the individual absorbances according to:

$$A = \sum_{i=1}^{n} A_i(\epsilon_{\lambda,i}, l, C_i), \tag{4.3}$$

where $\epsilon_{\lambda,i}$ is the molar attenuation coefficient of the species i in the medium at the wavelength λ, l the path length of the beam light through the material sample (usually equal to 1 cm) and C_i the concentration of the species i in the sample.

Calibration curves of standard solutions of C_6H_5OH and H_2O_2 are plotted at the maximal wavelength, $\lambda_{\text{max}} = 270\,\text{nm}$. Figure 4.3a presents the repetitions and average values of the absorbance of the different standard solutions of phenol $A_{C_6H_5OH}$ as a function of $C_{C_6H_5OH}$ and Figure 4.3b presents $A_{H_2O_2}$ as a function of $C_{H_2O_2}$. The linear fit of the data is also plotted on the figures.

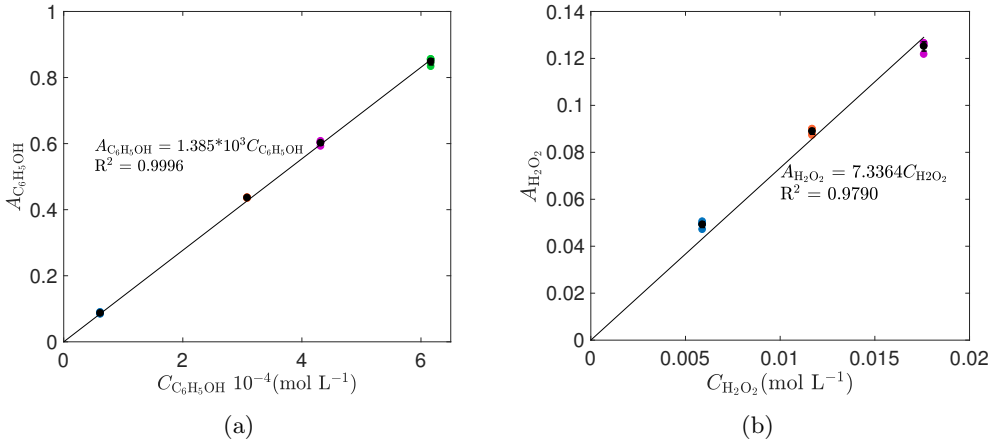

(a) (b)

FIGURE 4.3: Absorbance of standard phenol ($A_{C_6H_5OH}$) (a) or or hydrogen peroxide $A_{H_2O_2}$ (b) solutions as a function of their respective concentrations $C_{C_6H_5OH}$ and $C_{H_2O_2}$ at $\lambda_{max} = 270\,nm$.

In addition, the absorbance of experimental solutions subjected to different conditions were also determined to study their stability in time. Table 4.4 resumes the characteristics of each solution prepared following the experimental protocol presented in sections D.2.1 and D.2.3. Solution A is a *Phenol alone* solution (Ph_0) left on the bench and solution B consists of a mixture between phenol and H_2O_2 (M_0) non diluted and exposed to light (diluted just before the absorbance measurement). As for solution C, it is the same as B but diluted from the beginning and finally solution D is the same as C but kept in the dark. The absorbance of the different solutions, $A^{solution}$, in which *solution* refers to A, B, C and D, were recorded at 270 nm every hour over 5 h. The results are presented in Table 4.5. Note that the non-diluted solutions must be diluted before recording their absorbance since their direct use saturates the UV-visible spectrophotometer (in this case, $C_{C_6H_5OH} = 5.32 \times 10^{-4}\,mol \cdot L^{-1}$).

Solution	Description
A	*Phenol alone* solution exposed to light and diluted from the beginning
B	*Mixture 0* exposed to light as initially prepared. and diluted just before the absorbance measurement
C	*Mixture 0* exposed to light and diluted
D	*Mixture 0* kept in the dark and diluted

TABLE 4.4: Experimental conditions and absorbance of solutions of phenol and hydrogen peroxide under different conditions.

The absorbance of solution A (Phenol alone) corresponds well with the linear fit of the calibration curve plotted in Figure 4.3a. The absorbance of this solution is markedly different of that of solutions B, C and D. The reason behind why absorbances A and B

are different is that the addition of hydrogen peroxide to phenol increases the absorbance of the overall mixture, that is, the H_2O_2 absorbs at the same wavelength than the phenol. Thus, knowing the phenol and hydrogen peroxide concentration, the absorbance of the mixture can be calculated using the Equations in Figure 4.3a and Figure 4.3b and the value obtained is experimentally checked. However, given the absorbance of the mixture, it is not possible to obtain information about the changes in concentration of each compound separately (since the UV-visible technique is used herein without any separation coupled technique). Being aware of this limitation, in the following we use the changes on the overall absorbance to discuss the presence of chemical reactions in the system.

Solution	$A^{solution}$				
	$t = 0$	$t = 2\,\mathrm{h}$	$t = 3\,\mathrm{h}$	$t = 4\,\mathrm{h}$	$t = 5\,\mathrm{h}$
A	0.73	0.74	0.75	0.75	0.77
B	1.15	1.17	1.18	1.18	1.21
C	1.15	1.18	1.22	1.19	1.21
D	1.15	1.18	1.28	1.21	1.20

TABLE 4.5: Absorbance of the phenol solution and mixtures over a period of 5 h.

Another important observation is that the absorbance of mixtures B, C and D (all of them hydrogen peroxide/ phenol mixtures without treatment) are similar and therefore the dilution/exposition to light do not alter the medium. It is also noteworthy that in the absence of cavitation bubbles, when the mixture of phenol and hydrogen peroxide is left on the bench at room temperature and exposed to natural light over 48 h, a very slow reaction occurs between the molecules as a color change attests (from colorless to light yellow) which is disregarded in the following discussion in view of the duration of the degradation experiments using the piston impacts.

4.4 Correlation between the chemical activity and the physical parameters in a *fixed-bottom* geometry

We identified in Chapter 2 several physical parameters which influence the response of the system to the piston impact. We examine herein the effect of some of these parameters on the oxidation of phenol in the presence of H_2O_2. Furthermore, the effect of the parameters on a *Hydrogen Peroxide alone*, i.e. in the absence of the organic molecule and *Phenol alone* solutions is also investigated.

The discussion is primarily based on the absorbance of the solutions. In addition, when relevant, the increase of the pressure $P_{\text{top},0}$ under the piston is commented provided that gaseous products can be formed when degrading phenol (such as carbon dioxide).

4.4.1 Experimental protocol and absorbance determination

We proceed by doing a series of impacts using the same experimental protocol presented in Appendix C, section C.4. We briefly detail it in the following for a better comprehension of the results.

After each batch, we bring-up the piston to H_0, read the value of $P_{\text{top},0}$ displayed by the vacuometer before putting the reactor under atmospheric pressure. We then remove the piston and withdraw an aliquot of 2 mL from the bulk of the solution before setting the upper piston in place, vacuuming and doing a new series of impacts. The impact number varies as follows: at first only 1 impact is made. It is then followed by 9 other thus making a total of 10 impacts. A total of 100 is achieved afterwards before stopping at 500 impacts with a 100-impacts step. At this stage, four impacted solutions are available for the absorbance recording. Recall that the withdrawn aliquots are diluted before recording the absorbances. We detail the protocol established for the preparation of the solutions to record their absorbance in Appendix D, section D.2.4. Note that the absorbances are recorded 24 h after finishing the impacts.

4.4.2 Stability of hydrogen peroxide after impacts

This section focuses on the stability of hydrogen peroxide solutions after impacts. This step is important in order to quantify whether the changes of absorbance of a hydrogen peroxide/phenol mixture can be partially attributed to the degradation of the oxidant molecule.

There exists in literature studies about H_2O_2 stability. Drijvers et al.[240] determined by iodometric titration, i.e. using iodide, the degradation of 100 mmol of H_2O_2 in an aqueous solution subjected to sonication at a frequency equal to 520 kHz. The effective sonication power was equal to 12 W and the experiments were carried out at 29.5 °C. They observed the degradation of 2 % of H_2O_2 after 1 h and concluded that under the tested conditions, H_2O_2 is slowly degraded. They explained their result by relating it to the volatility of the molecule. Indeed, since H_2O_2 is hydrophilic and has a low volatility, it remains in the bulk solution and cavitation bubbles are unable to degrade it easily. Note that the authors used very little concentration of H_2O_2 which reduce the possibility of this latter to accumulate at the bubble interface to be more easily

degraded. On the other hand, Jiang et al.[245] noted an increase in the concentration of the hydrogen peroxide in the medium in the absence of organic molecules after 60 min. The authors examined the evolution of H_2O_2 concentration as a function of sonication time in the presence of a phosphate buffer (to vary the solution pH), at 610 kHz and an ultrasonic power of 25 W at 15 °C temperature. They showed an increase of H_2O_2 concentration as a function of sonication time and determined an optimum pH range ($2.8 < \text{pH} < 4.5$) in which hydrogen peroxide generation is maximized. Based on these two examples, we note that the formation and degradation mechanisms of hydrogen peroxide are very complex and strongly depend on the experimental parameters.

We therefore chose to study the effect the piston impacts have on a hydrogen peroxide solution to see if these molecules are destroyed by cavitation bubbles formed in the medium (in this case the concentration of H_2O_2 in the medium should decrease). We analyzed a solution containing 19.5 mL of hydrogen peroxide ($V_{\text{tot}} = 170$ mL) subjected to typical experimental conditions in which the impact height $H_0 = 20$ mm, the number of impacts N is equal to 10, 100 and 500 impacts in both fixed and mobile bottom configurations. Note that the impacts are successive and therefore the solution is not renewed before the end of the 500 impacts. The experimental protocol is detailed in Appendix C, section C.3.

A simple way to dose hydrogen peroxide is by titration in the presence of an acid with a standard solution of potassium permanganate. The overall reaction is written as:

$$2\,MnO_4^- + 5\,H_2O_2 + 6\,H^+ \longrightarrow 2\,Mn^{2+} + 5\,O_2 + 8\,H_2O$$

Figure 4.4a shows that in the absence of organic molecules, H_2O_2 is degraded to up-to 15 % after 500 impacts at $H_0 = 20$ mm in both configurations. The clear dependence of the mixture of the absorbance as a function of the the number of impacts shows that the process of degradation is continuous. Note that in these experiments, an increase in the initial pressure under the piston is recorded to up-to 100 impacts before stabilizing (see Figure 4.4b). This pressure evolution can be attributed to the formation of gaseous oxygen.

In order to verify that the changes in absorbance are directly linked to the degradation of the hydrogen peroxide added to water, we titrate a solution of water deprived of H_2O_2 subjected to the same experimental conditions. This also allows us to determine whether the oxidant molecule is formed in noticeable amounts starting from the combination of two $HO^\bullet$ radicals according to:

$$2\,HO^\bullet \longrightarrow H_2O_2. \tag{4.4}$$

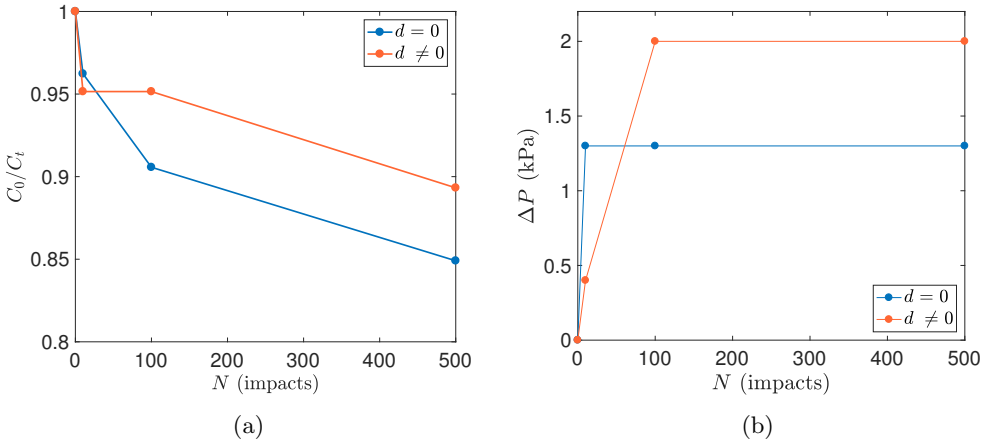

FIGURE 4.4: Evolution of the concentration of a hydrogen peroxide solution and the pressure in the reactor when impacted at $H_0 = 20\,\text{mm}$ in a fixed-bottom (blue) and mobile-bottom (orange) geometry.

In this case, the H_2O_2 concentration remained negligible (not shown on figure) compared to the amount added in our experiments (of the order of 2 %). This is consistent with the lack of hydroxyl radicals formation when impacting water. Note that no pressure increase is recorded.

Thus, we can conclude that for mixtures containing hydrogen peroxide, there is a consumption of hydrogen peroxide which will tend to decrease the overall absorbance of mixture at the wavelength chosen.

4.4.3 Effect of the impact height H_0 and the number of impacts on the oxidation of phenol/hydrogen-peroxide mixtures

We showed that when the impact height, H_0, is varied we modulate the maximal impact velocity $U_{\max}$ (Equation 2.2 in Chapter 2), the kinetic energy of the piston hitting the surface of the liquid and also the peak pressures generated during the impact. We expect that the higher the value of H_0 is, the more violent of the collapse of the bubbles and therefore the more intense the chemical activity of the mixture will be.

We present in Figure 4.5a the relative absorbance $\frac{(A - A_{t_0})}{A_{t_0}}$ as a function of the impact height H_0, A_{t_0} being the absorbance of M_0. The chemical experimental conditions of these results are presented in Table 4.2. Note that the following data are for an impact number $N = 100\,\text{impacts}$. Figure 4.5b shows the evolution of the difference of the pressure under the piston $P_{\text{top},0}$ before and after the impacts. Recall that the pressure augmentation recorded can be attributed to the possible formation of some of

the gaseous products such as CO and CO_2 and/or to the decomposition of H_2O_2 in the medium.

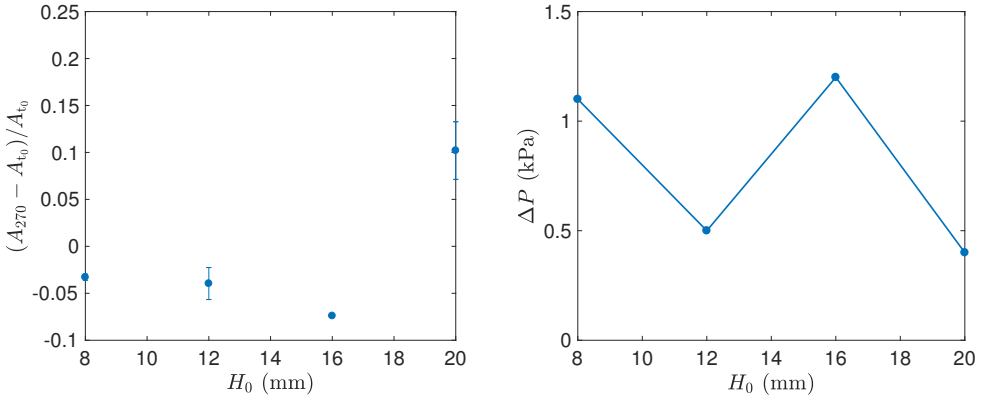

FIGURE 4.5: The evolution of $\frac{(A - A_{t_0})}{A_{t_0}}$ in (a) and $P_{\text{top},0}$ in (b) as a function of H_0 after $N = 100$ impacts and for $d = 0$.

Based on Figure 4.5a, we see that for an impact height smaller than $H_0 = 16\,\text{mm}$, the relative absorbance decreases with respect to the non-treated mixture. In general we observe a small decrease of the absorbance which can be attributed to H_2O_2/phenol degradation and intermediates formation which do not interfere in the absorbance. In this case, the change of pressure $P_{\text{top},0}$ inside the chamber is not significant and stays within the fluctuations of pressure typically observed in the experimental setup due to leakages or gas exsolution.

For $H_0 = 20\,\text{mm}$ (see Figure 4.5a), the results are markedly different. The concentration decrease of phenol and H_2O_2 are counterbalanced by intermediates absorbing at λ_{max} observing a significant net increase of the overall mixture absorption. This is consistent with the direct visualization of the mixture, where we can see a clear change of color (from colorless to light brown) due to some intermediates (such as *ortho-* and *para-*benzoquinone derivatives) showing that a significant chemical activity was triggered by the treatment of the mixture. The coloring of the medium due to phenol degradation has been previously reported in the literature[246].

To gain further insight into the process, we also plot the relative absorbance as a function of the number of impacts N for various impact heights H_0. The experimental parameters are presented in Tables 4.1 and 4.2.

We chose three common impact numbers for all impact heights, i.e. 1, 10 and 100 impacts. For further comparison, we proceeded by doing 500 impacts for only $H_0 = 8$ and 20 mm. We observed that $N = 1$ impact has no effect on the mixture (the absorbance of the

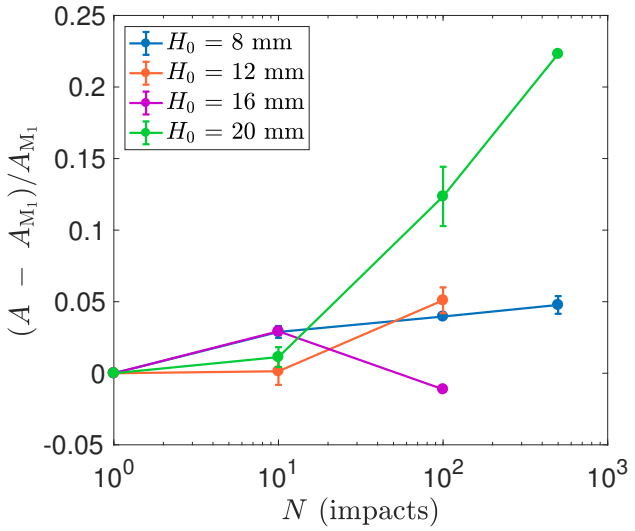

FIGURE 4.6: Evolution of $\frac{(A - A_{M_1})}{A_{M_1}}$ for various impact heights H_0 as a function of N in logarithmic scale for $d = 0$.

solution is of the same order of magnitude of M_0). Hence, the relative absorbance of this impact height is set to zero. Figure 4.6a presents the evolution of $\frac{(A - A_{M_1})}{A_{M_1}}$ as a function of N in logarithmic scale for various impact heightsH_0.

Increasing N gives an increase of the relative absorbance of the medium even for small values of H_0. For the highest impact height, the absorbance increases significantly after 500 impacts implying the formation of reaction intermediates. In general, we can set an impact number equal to $N = 100$ impacts as a minimal value to observe significant changes on the absorbance of the mixture. Thus, the experimental data prove that the number of impacts N plays an important role on the oxidation of phenol which experiences a continuous degradation. UV-visible spectrophotometry shows an increase of more than 50 % of the relative absorbance when N increases from 100 to 500 impacts.

We can say that in general, for the conditions tested the impact of the piston on a liquid's free surface can trigger a significant degradation of phenol in the presence of hydrogen peroxide for impact velocities equal or larger than $5\,\mathrm{m}\cdot\mathrm{s}^{-1}$. Unfortunately, the present analytic techniques does not allow us to differentiate the absorbance decrease linked to the disappearance of the reactants and the increase linked to the formation of the products. The use of HPLC technique seems more suitable for the extension of these preliminary analyses and the work is left for future investigations.

4.4.4 Effect of the concentration of hydrogen peroxide H_2O_2 on the oxidation of phenol/hydrogen-peroxide mixtures

In this section we focus on the effect of hydrogen peroxide concentration on the overall performance of the process. Due to the role played on the reaction enhancement, its use is inevitable especially when it comes to hydrophilic compounds such as phenol. However, from an industrial point of view and based on economical aspects, it is interesting to try to reduce the quantities of H_2O_2 used[200]. In addition, H_2O_2 can act as a radical scavenger[109] thus the importance of determining its optimum concentration.

In this work H_2O_2 is always withdrawn from the same bottle and the final solution volume is maintained equal to 170 mL. We chose to vary the amount of H_2O_2 as follows: at first, $C_{H_2O_2}$ is set to $1.123\,\text{mol}\cdot\text{L}^{-1}$ (see Figure 4.7a, green). Then, it was divide it by ~2 ($C_{H_2O_2} = 0.5644\,\text{mol}\cdot\text{L}^{-1}$) and by ~4 ($C_{H_2O_2} = 0.2822\,\text{mol}\cdot\text{L}^{-1}$). Finally, we want to test the response of the solution of *Phenol alone* subjected to the impacts. Table 4.6 resumes the different number of moles of hydrogen peroxide and their respective volumes. Note that the stoichiometric amounts are presented in red color.

Solution	$V_{H_2O_2}$ (mL)	$C_{H_2O_2}$ ($\text{mol}\cdot\text{L}^{-1}$)
1	0	0
-	2	0.115
2	4.9	0.282
3	9.8	0.564
4	19.5	1.123

TABLE 4.6: Summary of the experimental and stoichiometric volumes and concentrations of hydrogen peroxide.

Figure 4.7a presents the evolution of $\frac{(A - A_{t_0})}{A_{t_0}}$ for several mixtures of phenol and hydrogen peroxide as a function of the number of impacts N. The experiments reported are for an impact height $H_0 = 20\,\text{mm}$ and fixed bottom reactor. Figure 4.7b shows the pressure difference recorded in this case.

All the mixtures contain a quantity of hydrogen peroxide superior to its stoichiometric value. According to the results presented in Figure 4.7a, we can see that the absorbance evolution does not change significantly for solutions containing an amount of hydrogen peroxide below a critical threshold (solutions 1 and 2, blue and orange data respectively). Above a critical hydrogen peroxide concentration value (between 0.282 and $0.564\,\text{mol}\cdot\text{L}^{-1}$ for the conditions tested here) the absorbance increases exponentially with the number of impacts, showing that the chemical activity of the system is

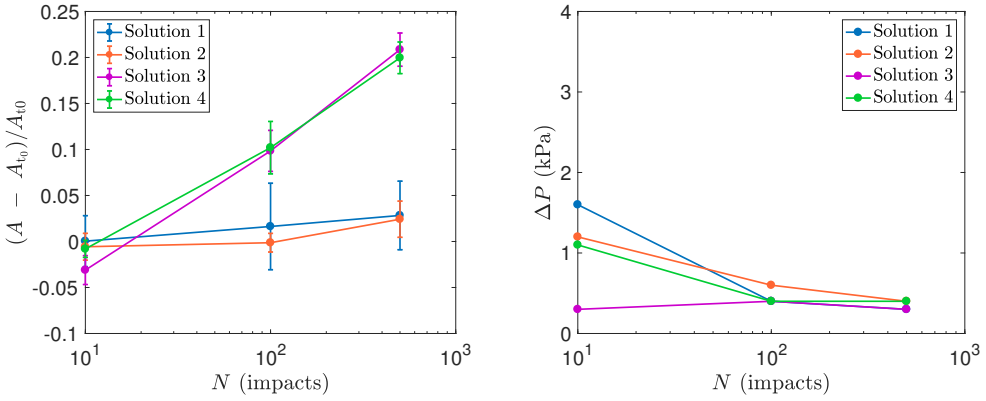

(a) (b)

FIGURE 4.7: (a): Variation of the relative absorbance $\frac{(A - A_{t_0})}{A_{t_0}}$ and (b): pressure difference for the mixtures of phenol and hydrogen peroxide solutions as a function of the number of impact N in semi- logarithmic scale. Fixed bottom configuration, $d = 0$ and $H_0 = 20\,\text{mm}$.

markedly more intense above a certain critical value of the hydrogen peroxide concentration (solutions 3 and 4, violet and green data respectively). Note that the concentration in H_2O_2 modifies the reaction kinetics and even at low values, the reaction probably takes place since the absorbance does not decrease as in the case of H_2O_2 alone but the analytic method does not allow us to go further. We therefore conclude that the reaction occurring between the organic molecule and the oxidant is linked to the generation of a significant amount of $HO^{\bullet}$ radicals in the mixture. For the impact intensities studied here, the addition of a sufficient amount of H_2O_2 is critical in order to be able to generate radicals during the bubble implosion.

The existence of a critical concentration value of H_2O_2 has been already reported in sonochemical applications. Lim et al.[109] studied the effect of the H_2O_2 concentration on the degradation of phenol and bisphenol A (BPA), two organic molecules differing among others in their volatility, BPA being more volatile than phenol. In a 1000 mL double-walled Pyrex reactor, the authors vary the concentration of hydrogen peroxide in a 500 mL solution containing initially $0.044\,\text{mmol} \cdot \text{L}^{-1}$ of phenol. They use a 10 cm cup-horn piezoelectric transducer operating at 35 kHz and the acoustic energy is around 40 W. The authors show that in the absence of target molecules, H_2O_2 is formed from a complex mechanism initiated by the water pyrolysis presented in Equation 4.1. They also tested four different concentrations of H_2O_2 ranging from 0.01 to $10\,\text{mmol} \cdot \text{L}^{-1}$ added at the beginning of the reaction and 30 min afterwards making an overall concentration ranging from 0.02 to $20\,\text{mmol} \cdot \text{L}^{-1}$. The authors show that in presence of H_2O_2, the degradation of both molecules was enhanced although the oxidant's concentration is an irrelevant parameter for the BPA degradation rate when the H_2O_2 concentration

exceeds the critical value whereas in the case of phenol, the reaction rate is shown to be dependent on the oxidant concentration. This observation is justified based on the properties of the molecules since H_2O_2 influences the degradation of non-volatile and hydrophilic compounds like C_6H_5OH rather than volatile molecules such as BPA [128,240]. If we assume that the $HO^{\bullet}$ radicals originate from H_2O_2 dissociation, we can say that at a critical concentration, the oxidant molecules are sufficiently concentrated at the bubble interface which, during its collapse stage will break the O−O bond and the formed radicals will react with the organic molecules in the bulk medium instead of those found in the bubble vicinity.

It is worth mentioning that the critical hydrogen peroxide value beyond which intense phenol degradation occurs is expected to be a strong function of the impact intensity. Indeed, the parametric study reported in Figure 4.6 for solution 4 shows that phenol degradation is not significant for $H_0 < 20\,\text{mm}$, which may require higher concentration of hydrogen peroxide for a substantial reaction to occur. These results seem to point out that the amount of H_2O_2 which one needs to add into the system in order to trigger a substantial phenol degradation can be significantly reduced by increasing the intensity of the impact. The maximum intensity of the impact being set by design parameters, it was not possible to explore regimes of more violent collapses. The dependence of the critical amount of hydrogen peroxide as a function of the impact intensity should be clarified in future works in order to evaluate the real potential of the technology for this application. Generally speaking, the results reported herein show that the plate-impact technology allows the intensification of chemical reactions in the presence of oxidants.

4.5 Correlation between the chemical activity and the physical parameters in a *mobile-bottom* geometry

The mobility d of the lower piston of the reactor influences the system response to the piston impact (recall that it enhances the activation of nuclei). In this section we test this configuration to enhance phenol degradation.

We present in Figure 4.8a the evolution of the relative absorbance $\frac{(A - A_{t_0})}{A_{t_0}}$ as a function of the impact height H_0 for $d = 0$ (blue experimental data, same as Figure 4.5a) and $d \neq 0$ (orange experimental data) for $N = 100$ impacts. Both configurations share similar features: the highest relative absorbance is recorded at $H_0 = 20\,\text{mm}$, which is consistent with the fact that we expect to degrade phenol molecules more intensively when increasing the impact intensity. The degradation observed when using the mobile bottom set-up is larger although the differences are not significant. In both configurations the increase of the absorbance is larger for $H_0 = 20\,\text{mm}$. For low intensities, small

differences between the two setups are observed. The recorded absorbance increase when $d \neq 0$ implying the formation of intermediates absorbing at $\lambda_{\max}$, while in the mobile bottom set-up it seems that the presence of products absorbing at the wavelength chosen is sufficiently important to induce a net increase of the overall mixture absorbance.

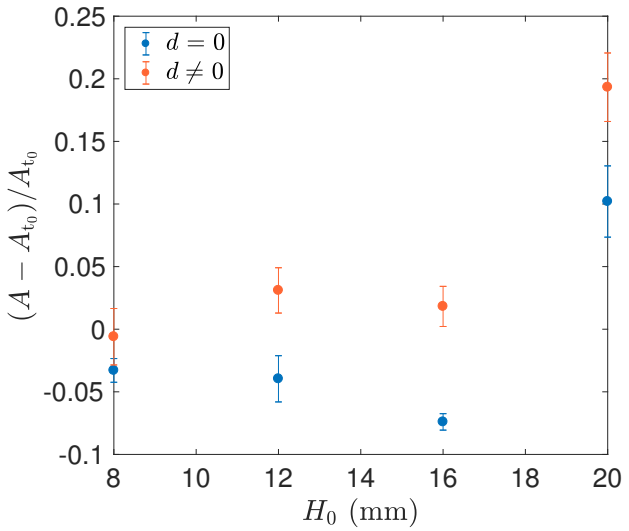

FIGURE 4.8: Evolution of $\frac{(A - A_{M_1})}{A_{M_1}}$ as a function of H_0 after $N = 100$ impacts in the case of the fixed ($d = 0$, blue dots) and mobile ($d \neq 0$, orange dots) bottom configurations.

As in the fixed-bottom configuration, we investigate the role played by the number of impacts on the reaction when the bottom of the reactor is mobile. Figure 4.9a presents the evolution of the relative absorbance (compared to A_{M_1}) as a function of N for various H_0. The interpretation of the results is more difficult than what was observed when $d = 0$ (see Figure 4.6a). Indeed for the highest H_0, the relative absorbance of the medium oscillates between positive and negative values of the relative absorbance. We recall that this situation is indeed possible given that reactants, intermediate products and final products can each of them either increase or decrease the overall absorbance of the mixture. Clearly, more sophisticated analytical techniques should be used to clarify and quantify the degradation of phenol in the mixture. Although the changes on the absorbance are an indicator of chemical activity in the medium, it is not possible to quantify if the degradation of phenol is intensified by the mobile bottom setup, which has been shown to activate a larger number of nuclei per unit volume.

As an alternative indirect measurement of the chemical activity, we plot in Figure 4.9b the pressure difference of $P_{\text{top},0}$ recorded in the reactor before and after the impacts (see also Figure 4.8a). As the initial pressure at $H_0 = 20\,\text{mm}$ seems to indicate the generation of gaseous products in a significant quantity, we can say that the reaction occurs in the medium at a significant rate.

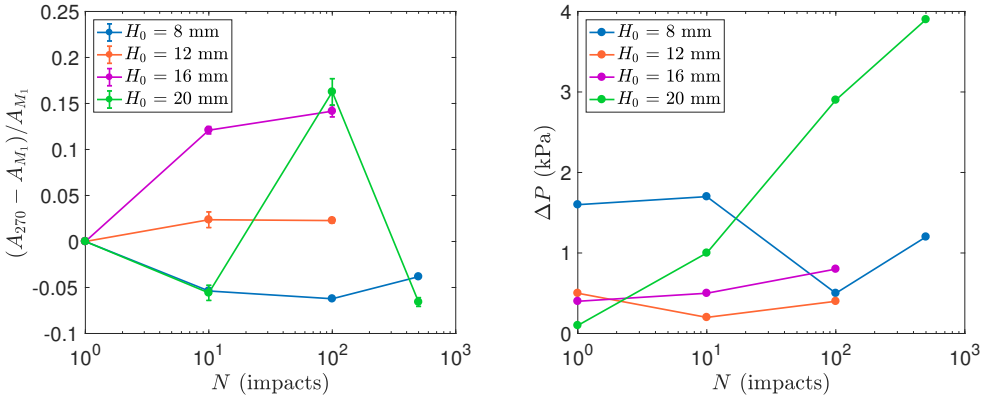

(a) (b)

FIGURE 4.9: (a): Evolution of $\frac{(A - A_{t_0})}{A_{t_0}}$ and (b): difference of $P_{\text{top},0}$ before and after the impacts for various impact heights H_0 as a function of N in logarithmic scale for $d \neq 0$.

Finally, Figure 4.10a presents the role played by the concentration of hydrogen peroxide in the medium in a mobile bottom configuration. Recall that the H_2O_2 concentration increases from Solution 1 to 4. As previously, the interpretation of the results is more difficult due to the large changes of different size between positive and negative relative absorbance variations. Still we can conclude that there exists a critical concentration threshold beyond which a significant reaction activity is observed. The two mixtures in which the concentration in H_2O_2 is higher than $\approx 0.5\,\text{mol}\cdot\text{L}^{-1}$ behave differently than when the hydrogen peroxide concentration is lower than this value, where the relative absorbance does not change significantly and therefore, we can conclude that no significant chemical activity occurs.

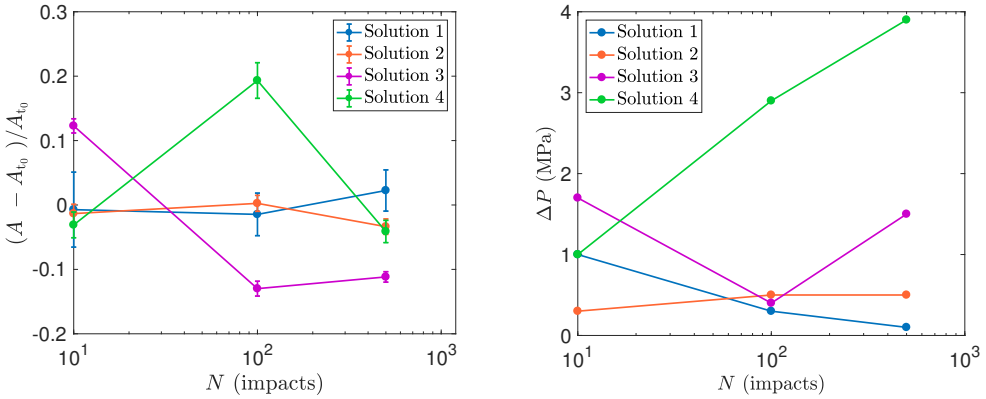

(a) (b)

FIGURE 4.10: (a): Variation of the relative absorbance $\frac{(A - A_{t_0})}{A_{t_0}}$ and (b): pressure difference for the mixtures of phenol and hydrogen peroxide solutions as a function of the number of impact N in semi- logarithmic scale for $d \neq 0$.

We can also relate the results to the pressure evolution in the medium presented in Figure 4.10b and note that for the two highest impacts, gaseous products are formed significantly. We speculate with the fact that the oxidation of phenol is more intense than under fixed bottom experimental conditions. These experimental studies should be taken carefully in the sense that a more detailed analytic examination of the medium's composition is necessary.

Conclusion

In this chapter, we examined the effect of various parameters on the oxidation of phenol in the presence and the absence of hydrogen peroxide. We showed that:

1. Hydroxyl radicals are *not* formed by simple impact of the piston on water;
2. The use of H_2O_2 as an oxidant is necessary when investigating the oxidation of phenol;
3. A critical concentration of hydrogen peroxide is needed to trigger the oxidation reaction;
4. Under the piston impacts, H_2O_2 is degraded;
5. The most suitable conditions to degrade phenol under the tested conditions are a high impact height and number of impacts in a mobile bottom configuration;

Despite the recent studies concerning cavitation-based technologies applied to wastewater treatment, researchers continue to investigate the parameters affecting the degradation of organic compounds in the presence of H_2O_2, proving that the field of study is far from being completely understood. In particular, the oxidation reaction of recalcitrant molecules is highly dependent on acoustic parameters such as the frequency used and chemical parameters like the pH of the solution, the temperature of the medium, the concentration of the substrates, etc.[245], many parameters that are awaiting us to explore.

Perspectives

We identified that the impact intensity plays a major role on the process of phenol degradation and the amount of hydrogen peroxide which needs to be added. Further evolution of the experimental set-up allowing more intense impacts may be interesting

in real applications in order to decrease the amount of oxidant which one needs to add to carry out the reactions.

It is also important to note that we could not explore the chemical activity in conditions where bubbles of the order of the critical bubble radius identified in Chapter 2 are present in the system. The impact of the collapse of large bubbles on the chemical processes taking place in the system is interesting to be further developed given that we measured the peak pressures during the collapse of these bubbles to be of the order of tens of MPa. The modification of the reactor geometry or the artificial injection of gas/vapor bubbles coupled with chemical reactions is an interesting research line that should be explored in the future. The use of an oscilloscope of a higher resolution would also be interesting since it is capable of resolving higher pressure transients and therefore record more accurately the peak pressures induced in the medium.

In addition to the above discussed parameters, one can inevitably say that there are still lots of other variables which can be studied, some of which we investigated but did not present the obtained results (for they were not conclusive) and some others which we identified earlier (such as pH, temperature control, etc.).

Like for any other chemical reaction, we can propose to study the role played by the liquid height $H_{0,l}$ presented in Figure 2.1 in Chapter 2. Lim et al.[101] investigated the effect of liquid height in a sonochemical reactor. The authors studied the oxidation of iodide I^- into triiodide ion I_3^-. They showed that the formation yield of I_3^- was less efficient when the volume of the solution was increased up-to 1 L and that for different input power conditions. Accordingly, they were able to determine the optimum liquid height/volume for different experimental conditions. The current setup should perform well for large liquid volumes, but definite conclusions would require the design of a large capacity experimental setup which was out of the scope of this work.

We also mentioned earlier the role that some chemical parameters can play on the oxidation of phenol. For example, Kidak and Ince[113] studied the impact of the pH of the solution on the degradation of C_6H_5OH. This parameter will influence the nature of the molecule. Indeed, for the phenol molecule, basic pH will favor the presence of the phenolate ion ($C_6H_5O^-$) rather than its molecular form (C_6H_5OH). This will affect the behavior of the molecule since with the repulsive forces that it acquires under basic (high) pH, phenol will stay away from the cavitation bubbles in which hydroxyl radicals are mostly present, whereas at lower pH, molecular phenol will more easily approach the bubble surface. This discussion is supported by the results presented in[113].

Furthermore, the initial concentration of the target molecule also plays an important role on the efficiency of the technology[101,113]. The reason why we chose an initial concentration of phenol equal to $0.0106\,\mathrm{mol}\cdot\mathrm{L}^{-1}$ is because we wanted to be close from the concentrations of the recalcitrant molecule present in discharge waters, and hence to be able to study a possible and realistic application of our technology to water treatments.

We can also imagine many other parameters such as the solution temperature, the saturation of the liquid by an oxidant like O_2 or even O_3, the reactor type, etc. and this make the study of the piston impact/ oxidation reaction very promising. Finally, other reaction types can also be investigated such as hydrolysis or transesterification.

Chapter 5

General conclusion and perspectives

In this research, we characterize a new device aimed at generating cavitation by a piston impact under controlled conditions. In particular, we clarified fundamental aspects of the interaction between processes induced by the collapse of bubbles and small-scale processes such as chemical reactions.

The experiments consist of the impact of a flyer on a liquid surface. The interaction between the falling plate and the liquid bulk generates a significant pressure variation with a multi-frequency content which is transmitted throughout the liquid. The overall analysis is based on quantitative measurements of the plate's position and velocity through high-speed camera visualizations and pressure recordings, which are possible using transducers attached to the plate and the bottom of the reactor. Direct visualizations of the liquid bulk are also used to clarify the response of bubbles after the impact.

A characterization of the interaction between the falling plate and the liquid is first proposed based on simple physical arguments:

- Three characteristic stages of the piston descent are defined based on the velocity measurements : (i) the first stage, called the *acceleration stage* between the instant at which the piston is released by the electro-magnet and the moment at which the velocity reaches its maximum ; (ii) the second stage ranges from the moment of maximal velocity until the moment of impact at which the pressure is maximal and the gas/ vapor layer is compressed thus the name *compression stage* ; (iii) the third and last stage called the *rebound stage* and characterized by the minimal velocity during which the piston bounces back on the liquid surface.

- The description of the piston descent is correlated to the pressure signals obtained. It is shown that the thicker the layer existing between the piston and the liquid column is, the lower the peak pressures are. This reveals the damping role of the gas/vapor layer trapped between the free surface and the piston on the generated pressures. It is evidenced through the determination of the effective polytropic coefficient that the compression of the gas/vapor layer is adiabatic in the *acceleration stage*, while heat and mass transfer processes become relevant in the *compression stage*. The results are consistent with theoretical predictions of the response of gas/vapor mixtures as a function of the Péclet number.

- The impact time is defined as the difference between the instants when the velocity and the pressure reach their maxima. It is also correlated to the effective polytropic coefficient.

- It is demonstrated through the Daubechies wavelets analysis that the whole process generates a wide range of frequencies (up-to a hundred kilo hertz) making the technology of the plate impact very interesting to excite bubbles with various sizes (e.g. resonances frequencies). It is also shown that the frequency of excitation is strongly influenced by the dynamics of the gas/vapor layer and the initial amount of vapor.

- We derive simple models that allows relating the maximal pressures generated in the medium to the impact velocities and the characteristic frequencies to the medium's compressibility.

- The mobility of the piston has no significant effects on the above conclusions despite its role played on the intensity of the rebound of the piston.

The second part of this manuscript discussed the bubble dynamic effects induced by the impact of the piston:

- A critical radius based on the Rayleigh collapse time and the characteristic time of pressure increase on the system is determined (around a millimeter) to differentiate the response of bubbles according to their initial size.

- The collapse of bubbles which radii are greater than the critical radius is typically described by two characteristic stages: (i) the primary collapse (i.e. bubble implosion) and (ii) the fragmentation followed by the dynamic cluster response. This process is shown to induce an intense turbulence that intensifies mixing.

- Small bubbles, i.e. bubbles which radii are smaller than the critical radius, are shown to expand when tension states occur in the medium. The evolution of their radii shows that they collapse and oscillate very rapidly.

- Jet formation is evidenced when small bubbles collapse asymmetrically both, close to the walls and also in the bulk liquid where the presence of surrounding bubbles act as a source of asymmetry.
- The mobility of the bottom of the reactor is shown to play a crucial role on the dynamic response of bubbles. Generally, bubbles larger than the critical size implode at a different times compared to the fixed- bottom geometry. For bubbles smaller than the critical radius, the mobility of the piston tends to increase the strength of tension states enhancing the activation of small bubbles.

The last part of the manuscript investigates the application of the plate impact technique to the intensification of a chemical process: the oxidation of phenol in the presence of an oxidant molecule, hydrogen peroxide:

- Simple impacts on pure water are shown to be incapable of generating radical species such as hydroxyl radicals responsible of the attack of organic molecules.
- The study of the stability of hydrogen peroxide solutions to piston impacts shows that the oxidant molecule is degraded by cavitation bubbles.
- The parametric study of phenol degradation shows that in general, the higher the impact intensity is, the higher the reaction rate and the lesser the hydrogen threshold quantity needed to trigger the reaction are.

Although this work represents a significant advance in the investigation of the plate-impact method as a precursor of physical phenomena and chemical processes, more work remains to be done to thoroughly explain and extend it to practical applications. Some possibilities are given below:

- Increasing the pressure surrounding the piston is a possibility to make the impact more intense on the liquid just like decreasing the piston's mass per unit surface.
- Further parametric studies can help to better understand the improvements needed for the reactor design to better synchronize the appearance of bubbles and the occurrence of the maximal pressure peak in order to optimize the performance of this technology.
- The behavior of the asymmetrical bubbles should be further studied to clarify the role of jetting and their related damaging/cleaning effects of solid surfaces.
- The effect of the nature and the design of the lower piston on the impact should be also investigated in further detail.

- The influence of either fresh or used water on the number of bubbles naturally activated should be investigated as well as the optimal method to artificially inject bubbles in the system.
- The role of the impact height on bubble population would inevitably affect the chemical reaction and therefore it should be further clarified.
- Simpler oxidation reactions can be interesting to investigate to acquire a better comprehension of the phenomena occurring when bubbles implode.
- To improve the analytical methods used and/or to use new methods is critical to clearly distinguish the evolution on concentration of the various compounds generated during the reaction process. This step is critical for a better comprehension between the presence of bubbles and the chemical activity.
- The coupling of heterogeneous catalysis is also a promising field. The addition of a solid catalyst is considered to be very interesting since it is shown to increase bubble population (increase nucleation sites). It might also affect the pressure transmission to the medium.
- Other types of reactions such as hydrogenation or transesterification can also be considered.

All of the mentioned parameters and even more can only elicit the curiosity of a researcher. The work presented in this manuscript is just a beginning.

Appendix A

Piston position determination

A.1 Piston position determination

The experimental device is designed in order to record the piston's motion and the bubble response to its impact. Accordingly, through the images recordings of the piston, we can determine its instantaneous position, and therefore calculate its temporal velocity and acceleration through simple derivation. Herein, we detail the steps followed to determine the position H through a typical example for which the impact height $H_0 = 16\,\text{mm}$ and the lower piston is fixed. Note that the recordings are of a small target attached to the upper piston and which diameter is equal to $2.09 \times 10^{-3}\,\text{mm}$.

Figure A.1 presents three representations of the piston position detection. In the upper part of the figure, we present images of the target on which we annotate the position of its lower limit (in a red circle) using the indices determined from the figures in the middle. Indeed, these figures present the evolution of the gray level of the images as a function of the position in pixels. Using these indices, we determine the position of the piston which we present in the lower part of the figure. We detail the method in the following.

We start by determining the average values of the color of the image in the y-axis which we will call *imcol*. We then calculate a threshold, *thresh* based on the minimal and maximal values of *imcol*. Then, we determine the index for which $imcol > thresh$. To have a sub-millimetric resolution of the threshold value, we refer to the use of a correction factor based on the ratio of the difference between the threshold and the grey scale for which the index was calculated, and the grey scale at the index plus one and index. For each image of the video recording, we define the index of the lower limit

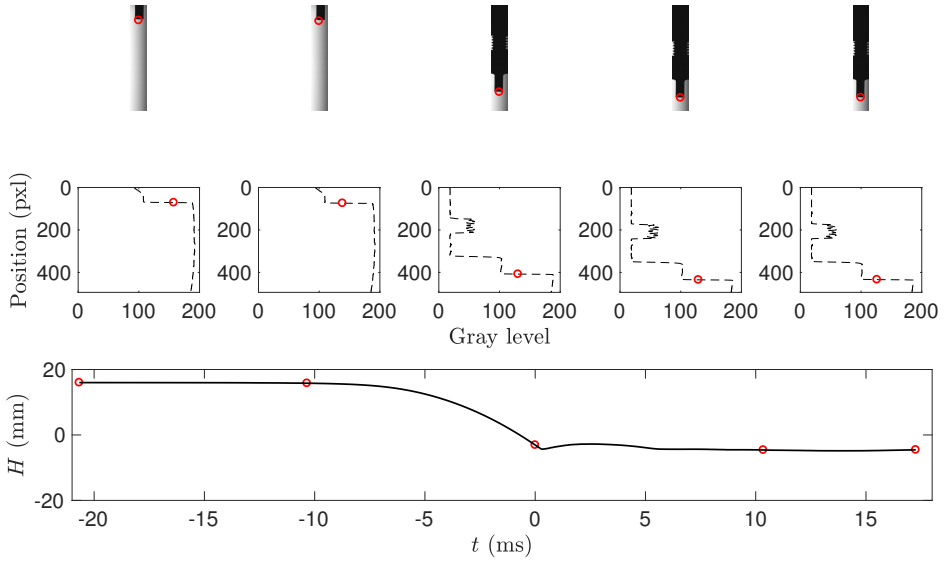

FIGURE A.1: Piston position detection method explained using a typical example for which$H_0 = 16\,\text{mm}$, $d = 0$, $P_{\text{top},0}/P_{\text{vap}} = 1$ and frame rate: 56 000 fps. (left): image of the target, (middle): detection of the target based on its gray level, (right): position of the piston.

of the target based on the threshold value calculated previously. Again, to get a sub-millimetric resolution of the piston position, we resort to the use of the correction factor introduced previously.

The last step of the position determination consists of the passage from pixels to the characteristic size of the position. By calculating the width of the target in pixel from the average values in the x-axis, we determine the correlation coefficient between pixels and millimeters. Accordingly, the position is determined as the ratio between the determined index and the coefficient.

Finally, the time is determined as the ratio between the difference between the image number and the number of images before the trigger and the frame rate of the image recording.

Appendix B

Examples of the evolution of bubbles' radii larger than the critical radius

We present the radii evolution of various bubbles larger than the critical one in both configurations of the experimental set-up, i.e. fixed and mobile lower piston and the pressure variation in the medium. Note that in some cases, two bubbles appear next to the optical access and therefore the presence in the following of two figures for a set of experimental conditions. In addition, in some other cases several repetitions of the same experimental conditions are presented. The figures captions resume the details.

B.1 In a fixed-bottom configuration

Comments Figures B.1 and B.2 present the evolution of the radius of large bubbles in black as a function of time and the temporal evolution of the pressure under the piston P_{top} in red in a fixed-bottom geometry for various impact heights H_0. As presented in Chapter 3, in a fixed-bottom geometry, bubbles attached to the optical access tend to collapse during the first pressure peak. These figures show further examples.

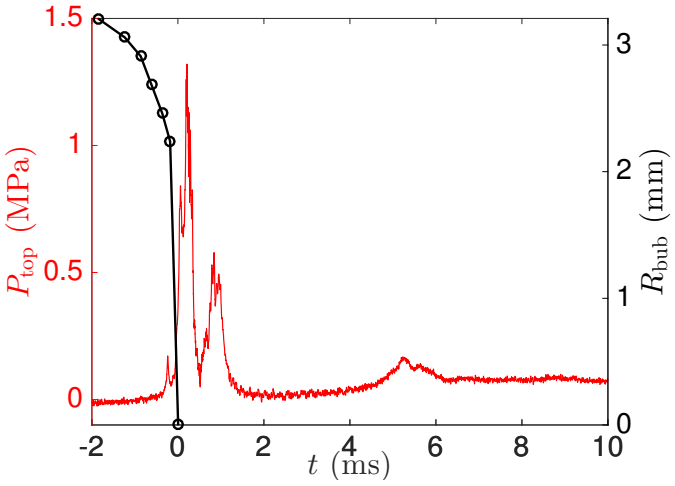

FIGURE B.1: Temporal evolution of the pressure under the piston P_{top} and the radius of the recorded bubble for the following experimental conditions: $d = 0$, $H_0 = 10\,\text{mm}$.

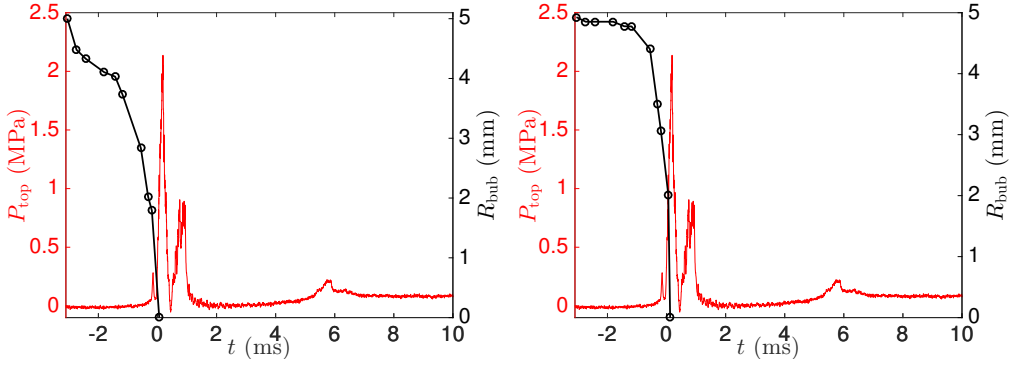

(a) (b)

FIGURE B.2: Temporal evolution of the pressure under the piston P_{top} and the radius of the recorded bubble for the following experimental conditions: $d = 0$, $H_0 = 16\,\text{mm}$. (a): first bubble; (b): second bubble.

B.2 In a mobile-bottom configuration

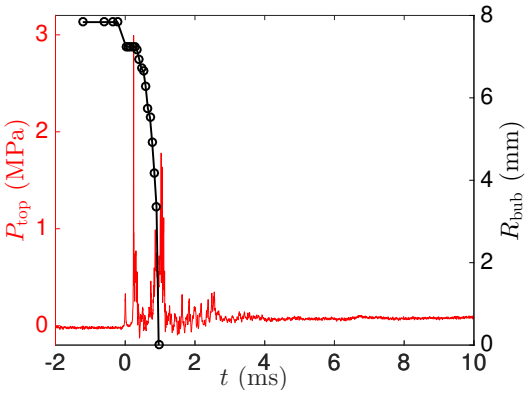

FIGURE B.3: Temporal evolution of the pressure under the piston P_{top} and the radius of the recorded bubble for the following experimental conditions: $d \neq 0$, $H_0 = 10\,\text{mm}$.

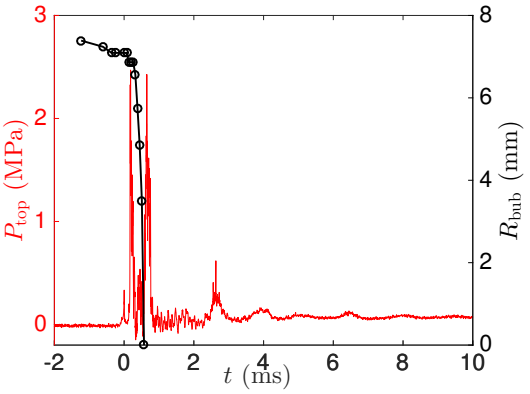

FIGURE B.4: Temporal evolution of the pressure under the piston P_{top} and the radius of the recorded bubble for the following experimental conditions: $d \neq 0$, $H_0 = 15\,\text{mm}$.

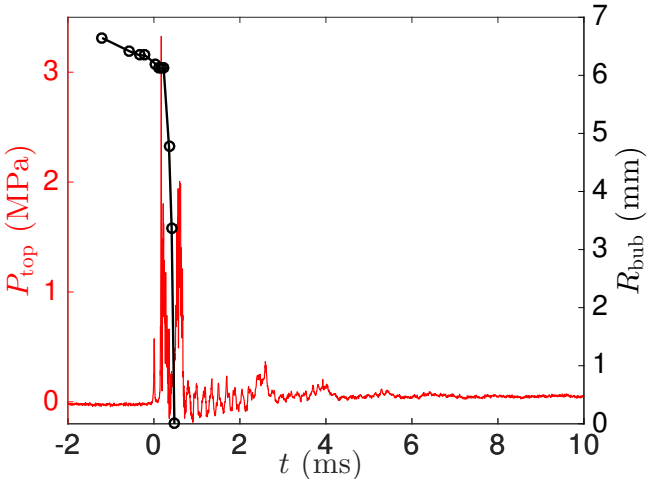

FIGURE B.5: Temporal evolution of the pressure under the piston P_{top} and the radius of the recorded bubble for the following experimental conditions: $d \neq 0$, $H_0 = 18\,\text{mm}$.

Comments Figures B.3, B.4 and B.5 present some examples of the collapse of bubbles which radii (presented in black) are larger than the critical radius. We also show the pressure evolution under the piston P_{top}. We showed in Chapter 3 through through image recordings that in a mobile-bottom geometry, bubbles attached to the optical access collapse during the second pressure peak which is also observable through the examples herein.

Appendix C

Experimental procedures

C.1 Iodine solution titration

1. Prepare 250 mL of a $0.1\,\mathrm{mol}\cdot\mathrm{L}^{-1}$ of potassium iodide;
2. Withdraw an aliquot of 2 mL of the mixture after the desired number of impacts N;
3. Put the aliquot into an erlenmeyer flask;
4. Add slowly using a burette a solution of sodium sulfate of concentration $0.1\,\mathrm{mol}\cdot\mathrm{L}^{-1}$ prepared in a 100 mL volumetric flask;
5. When the solution starts to decolorize, add a spatula of Iotec: the solution turns into blue;
6. Continue by adding slowly sodium sulfate until decolorization.

C.2 Phenol solution preparation before the piston impacts

The experimental protocol established to prepare the phenol-based solutions is as follows:

1. In a 200 mL volumetric flask, prepare a phenol solution with a concentration equal to $C^{prepared}_{\mathrm{C_6H_5OH}} = 0.011\,\mathrm{mol}\cdot\mathrm{L}^{-1}$;
2. Using 20 and 50 mL volumetric pipettes and a 10 mL graduated pipette, mix 131 mL of the phenol solution with 19.5 mL of distilled water in a 200 mL beaker;
3. Using a 10 mL graduated pipette, take the desired volume of hydrogen peroxide directly from the bottle (mother solution) and put it in a 25 mL beaker;

4. Mix both solutions just before putting them in the reactor. The total reaction volume, V_{tot} is equal to 170 mL. Therefore, the concentration of phenol in the final mixture and thus in the reactor $C^{reactor}_{C_6H_5OH}$ is equal to

$$C^{reactor}_{C_6H_5OH} = 0.0082\,\text{mol} \cdot \text{L}^{-1}; \tag{C.1}$$

5. To the remaining phenol solution, i.e. $V = 69$ mL, add 20.5 mL of distilled water in a 150 mL beaker in order to obtain the same dilution as in the reactant mixture and to give a blank solution.

C.3 Hydrogen peroxide stability to piston impacts

1. In a 200 mL volumetric flask, prepare a potassium permanganate solution with a concentration equal to $0.18\,\text{mol} \cdot \text{L}^{-1}$. This will serve to titrate the aliquots;
2. In a 200 mL beaker, prepare an aqueous solution of hydrogen peroxide of $1.123\,\text{mol} \cdot \text{L}^{-1}$ with a total volume equal to 170 mL;
3. Proceed by doing the desired number of impacts N at an impact height H_0 equal to 20 mm after putting the reactor under vacuum;
4. Withdraw a 2 mL aliquot;
5. Add 10 mL of sulfuric acid of concentration equal to $0.25\,\text{mol} \cdot \text{L}^{-1}$;
6. Proceed by titrating it using the prepared permanganate solution. The equivalence point is reached once the violet color of permanganate persists in the medium. Note that oxygen is formed during the reaction between permanganate and hydrogen peroxide.

C.4 Experimental procedure for the piston impacts

C.4.1 Part One – Vacuuming the system

Once the solution *Mixture 0* is prepared, the first part of the experimental protocol is as follows:

1. Transfer the solution *Mixture 0* to the reactor;
2. Set the upper piston in place after lubrification;

3. Once the piston is attached to the electro-magnet, bring it above the liquid's surface at a certain distance H and start the pump;

4. Open the adequate valves (not shown on Figure 2.1): the pressure starts to decrease inside the reactor chamber. The vacuometer displays a decreasing value of $P_{\text{top},0}$. This first vacuum duration is about 5 s;

5. Close the valves and set the piston to the desired value of H_0;

6. Re-open the valve sand continue the vacuum for around 10 s;

7. Close the valves and stop the pump: the vacuometer displays a $P_{\text{top},0}$ value close to P_{vap}.

C.4.2 Part Two – Sampling after the impacts

Now that the experimental set-up is ready, the second part of the experimental protocol is as follows:

1. Start by doing N impacts at the desired impact height H_0, N being the number of impacts;

2. Bring back the piston's position to H_0 and open the valve to read $P_{\text{top},0}$ after N impacts;

3. Put the reactor under atmospheric pressure and remove the piston;

4. Withdraw an aliquot of 2 mL from the bulk of the solution, set the upper piston in place and repeat steps 3 to 7 of Part One.

5. If desired, proceed by doing another set of N impacts and repeat steps 2 to 5 as many times as it is necessary.

Appendix D

Characterization techniques

D.1 Gas Chromatography

This analytical technique is based on the injection of a sample in a gas or liquid phase into the instrument, i.e. gas chromatograph. The apparatus consists mainly of an injector, a column and a detector. Figure D.1 presents a picture of the apparatus used in the laboratory. In brief:

- The injector is used to vaporize the liquid injected mixture. In the injector, the solution is transported by an inert gas stream called the mobile phase which passes it into a separation tube, i.e. the column;
- The column separates the constituents of the injected mixture. It is composed of a stationary phase with which the molecules will interact based on their affinities. Most often, capillary columns are used in which the stationary phase coats the walls of a small-diameter tube. Accordingly, the separation of the compounds is based on the different strengths of interaction of the compounds with the stationary phase.
- The detector measures the quantity of the components that exit the column and transforms the signal into a peak with a certain height and area related to the concentration of each molecule. To analyze a sample with an unknown concentration, a standard sample of known concentration is injected into the instrument. The standard sample peak retention time (appearance time) and area are compared to the test sample to calculate the concentration.

In this manuscript, the samples were analyzed using a Shimadzu GC-2025 equipped by a Zebron ZB-5MSi column from Phenomenex. The stationary phase of the column is

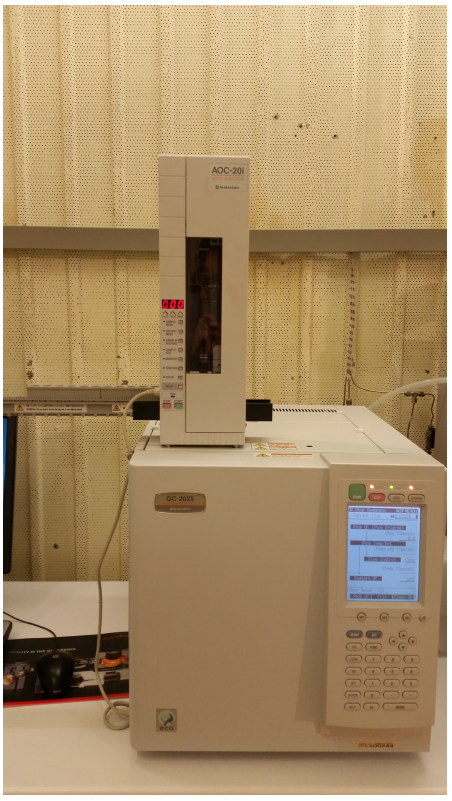

FIGURE D.1: A picture of the Gas Ghromatograph used for sample analysis.

composed of 5 % of phenyl and 95 % of dimethylpolysiloxane which makes the column of low polarity. Helium was used as the so-called carrier gas at a flow rate equal to 70.7 mL/ min. The volume of the samples injected was equal to 0.2 µL and the temperature of the injector was equal to 280 °C which was the same as the temperature of the detector. The detector was a Flame Ionization Detector (FID). Figure D.1 presents the chromatograph used in the laboratory.

Figure D.2 shows an example of the peak of phenol resulting from its injection. This latter is done automatically using an auto-injector AOC-20i purchased from Shimadzu (see Figure D.1).

As Figure D.2 shows, the retention time of phenol is equal to 3.11 min under the experimental conditions. The temperature program of the column is presented in Figure D.3.

D.2 UV-visible spectroscopy

Ultraviolet and Visible absorption spectroscopy (UV-visible spectroscopy) is based on the measurement of the amount of light absorbed after passing through the sample, i.e. the interaction of light with matter. The absorption measurement can be of two types,

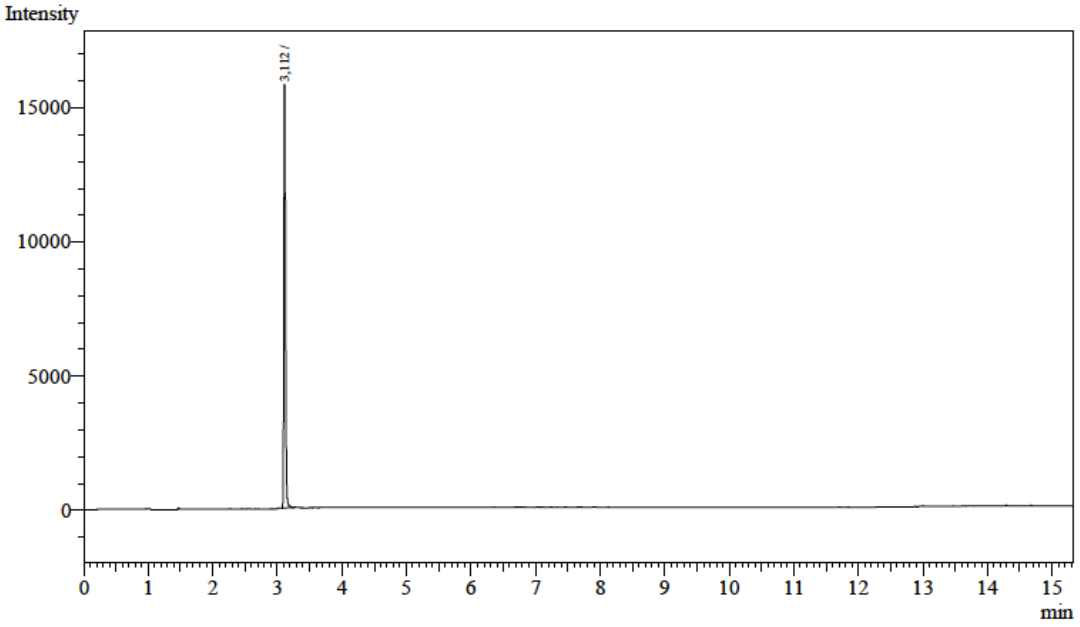

FIGURE D.2: An example of the obtained phenol peak using the GC.

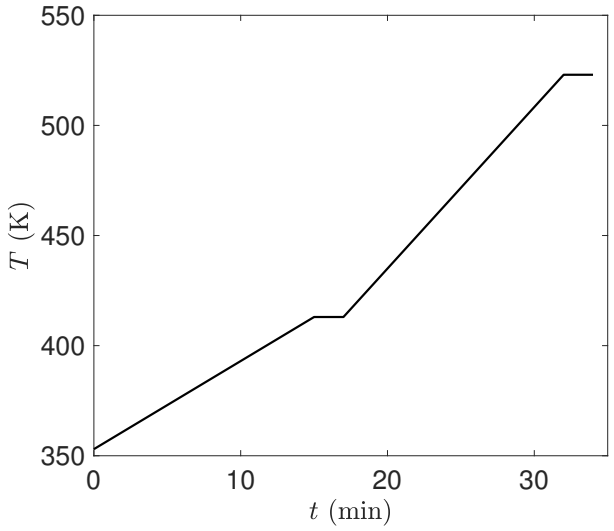

FIGURE D.3: The temperature program used for the GC analysis.

at a particular wavelength λ or extended over the UV- Visible spectral range (200 to 800 nm). The UV-Visible light is quite energetic which is sufficient to enable electronic transitions from lower to higher energy levels within molecules or inorganic complexes in solution. There are single and double beam spectrophotometers.

Figure D.4 presents the apparatus used to measure the absorbance of the samples. The apparatus is a Cary 50 UV-Vis purchased from Varian. It is a single beam spectrophotometer and consists of a light source, a monochromator (holographic grating), sample/reference cell, detector (two silicone diode tubes) and recorder (usually a computer,

FIGURE D.4: The UV-visible spectrophotometer.

not shown here). It has a wavelength range between 190 and 1100 nm and the cell was made of quartz with a characteristic length l equal to 1 cm.

Two key measures commonly used to define or characterize absorption peaks in UV-Visible spectra are: lambda max $\lambda_{\max}$ and epsilon max $\epsilon_{\max}$ which are respective to each compound. $\lambda_{\max}$ corresponds to the wavelength at which the absorbance is maximal ($A_{\max}$) and $\epsilon_{\max}$, the molar extinction coefficient is determined starting from standard solutions of known concentration C for which A was recorded.

D.2.1 Standard phenol solution preparation

- In a 50 mL volumetric flask, dilute a mass of phenol equal to 0.0025 g and make up to the mark with distilled water. This is the mother solution containing $C_{C_6H_5OH} = 6.17 \times 10^{-4}\,\text{mol} \cdot \text{L}^{-1}$;
- Using this solution prepare 3 solutions of C_6H_5OH with concentrations equal to 0.617×10^{-4}, 3.085×10^{-4} and $4.319 \times 10^{-4}\,\text{mol} \cdot \text{L}^{-1}$ in 25 mL volumetric flasks (see Table D.1 for the withdrawn volumes V_{solution} of the mother solution);

- Record their absorbance spectra and their respective absorbance $A_{C_6H_5OH}$ at the wavelength $\lambda_{max} = 270\,\text{nm}$. The absorbance spectrum is repeated three times and the average absorbance at λ_{max} is calculated based on five repetitions.

$\boldsymbol{C}_{C_6H_5OH}$ $(10^{-4}\ \text{mol}\cdot\text{L}^{-1})$	$\boldsymbol{V}_{\textbf{solution}}$ (mL)
0.617	2.5
3.085	12.5
4.319	17.5
6.17	-

TABLE D.1: Withdrawn volumes and absorbance of standard phenol solutions.

Figure D.5 presents a typical example of the absorbance spectra ($Area_{C_6H_5OH} = f(\lambda)$) for a phenol solution which has been impacted 10 times at $H_0 = 16\,\text{mm}$ and $d = 0$.

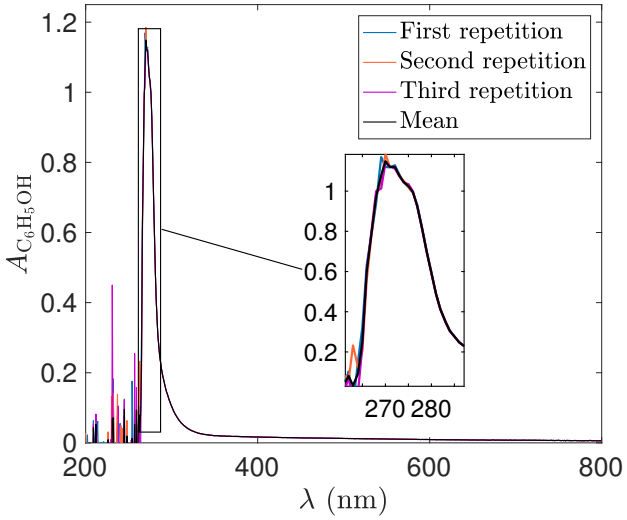

FIGURE D.5: An absorbance spectrum of a $0.01\,\text{mol}\cdot\text{L}^{-1}$ phenol solution impacted 10 times at $H_0 = 16\,\text{mm}$ and $d = 0$.

D.2.2 Concentration of hydrogen peroxide in the commerical solution

It is noted on the bottle that the content in hydrogen peroxide is of 30 %H_2O_2 by weight. This implies that there are 30 g of H_2O_2, denoted m, per 100 g of solution.

The density is equal to $\rho_{H_2O_2}^{mother\ sol} = 1.11\,\mathrm{g}\cdot\mathrm{mL}^{-1}$ therefore:

$$\begin{aligned}
\rho_{H_2O_2}^{mother\ sol} &= \frac{m}{V} \\
V &= \frac{m}{\rho_{H_2O_2}^{mother\ sol}} = \frac{100}{1.11} \\
V &= 90.09\,\mathrm{mL}
\end{aligned}$$

The mass concentration C_m is

$$\begin{aligned}
C_\mathrm{m} &= 100 \cdot \frac{m}{V} \\
C_\mathrm{m} &= 100 \cdot \frac{30}{90.09} \\
C_\mathrm{m} &= 33.3\,\mathrm{g\ of\ H_2O_2\ per\ 100\,mL\ solution}
\end{aligned}$$

100 mL contain 0.979 mol of H_2O_2 meaning that the concentration of hydrogen peroxide in the bottle $C_{H_2O_2}^{bottle}$ is equal to:

$$\begin{aligned}
n_{H_2O_2} &= C \cdot V \\
C_{H_2O_2}^{bottle} &= \frac{n_{H_2O_2}}{V} \\
C_{H_2O_2}^{bottle} &= \frac{0.979}{0.1} \\
C_{H_2O_2}^{bottle} &= 9.79\,\mathrm{mol}\cdot\mathrm{L}^{-1}
\end{aligned}$$

Note that in general, the concentration of a specie x after dilution is calculated according to: $C_\mathrm{i}V_\mathrm{i} = C_\mathrm{f}V_\mathrm{f}$.

D.2.3 Hydrogen peroxide standard solution preparation

- In a 250 mL volumetric flask, add 5 mL of H_2O_2 withdrawn directly from the commercial solution using a 5 mL graduated pipette and make up to the mark with distilled water: $C_{H_2O_2} = 0.1958\,\mathrm{mol}\cdot\mathrm{L}^{-1}$;
- Prepare 3 solutions of H_2O_2 with concentrations equal to 0.006, 0.089 and 0.125 $\mathrm{mol}\cdot\mathrm{L}^{-1}$ in 25 mL volumetric flasks (see Table D.2 for the withdrawn volumes V_solution of the mother solution);
- Record their absorbance spectra and their respective absorbance $A_{H_2O_2}$ at 270 nm. The absorbance spectrum is repeated three times and the average absorbance at λ_max is calculated based on five repetitions.

$C_{H_2O_2}$ $(mol \cdot L^{-1})$	$V_{solution}$ (mL)
0.006	0.751
0.089	1.502
0.125	2.253

TABLE D.2: Experimental conditions and absorbance of the standard hydrogen peroxide solutions.

D.2.4 The determination of the absorbance A

The experimental protocol to determine the absorbance of an aliquot is as follows:

1. In a 25 mL volumetric flask, put 1.6 mL of the 2 mL-aliquot using a 2 mL graduated pipette;
2. Complete with distilled water until few drops below the volume mark;
3. Swirl to homogenize the solution;
4. Complete to the meniscus and place the stopper on the top of the flask;
5. Invert the flask three times to homogenize the solution;
6. Using a disposable pipette, withdraw couple of milliliters of the solution and put them in the UV- visible cell;
7. Record the absorbance of the phenol molecule at 270 nm that we will call $\boldsymbol{A}$.

Bibliography

1. Fuster D, Montel F. Mass transfer effects on linear wave propagation in diluted bubbly liquids. *Journal of Fluid Mechanics* . 2015;779:598–621.

2. Daou MM, Igualada E, Dutilleul H, Citerne JM, Rodríguez-Rodríguez J, Zaleski S, Fuster D. Investigation of the collapse of bubbles after the impact of a piston on a liquid free surface. *AIChE Journal* . 2017;.

3. Donny F. Sur la cohésion des liquides, et sur leur adhérence aux corps solides. *Annales de chimie et de physique* . 1846;16:167–190.

4. Berthelot M. Sur quelques phénomènes de dilatation forcée des liquides. *Annales de chimie et de physique* . 1850;:1–6.

5. Reynolds O. Papers on mechanical and physical subjects, vol. III.The sub-mechanics of the universe. Cambridge: University Press. 1903.

6. Trevena DH. Cavitation and the generation of tension in liquids. *Journal of Physics D: Applied Physics* . 1984;17(11):2139.

7. Cook SS. Erosion by water-hammer. *Proceedings of the Royal Society of London Series A, Containing Papers of a Mathematical and Physical Character* . 1928;119(783):481–488. .

8. van Wijngaarden L. Mechanics of collapsing cavitation bubbles. *Ultrasonics Sonochemistry* . 2016;29:524–527.

9. Rayleigh L. VIII. On the pressure developed in a liquid during the collapse of a spherical cavity. *Philosophical Magazine Series 6* . 1917;34:94–98. .

10. Neppiras E. Macrosonics in industry 1. Introduction. *Ultrasonics* . 1972;10(1):9–13.

11. Moholkar VS, Warmoeskerken MMCG, Ohl CD, Prosperetti A. Mechanism of mass-transfer enhancement in textiles by ultrasound. *AIChE Journal* . 2004;50(1):58–64.

12. Mason TJ. Ultrasonic cleaning: An historical perspective. *Ultrasonics sonochemistry* . 2016;29:519–523.

13. Dular M, Griessler-Bulc T, Gutierrez-Aguirre I, Heath E, Kosjek T, Klemenčič AK, Oder M, Petkovšek M, Rački N, Ravnikar M, Šarc A, Širok B, Zupanc M, Žitnik M, Kompare B. Use of hydrodynamic cavitation in (waste)water treatment. *Ultrasonics Sonochemistry* . 2016;29:577–588.

14. Braeutigam P, Franke M, Schneider RJ, Lehmann A, Stolle A, Ondruschka B. Degradation of carbamazepine in environmentally relevant concentrations in water by Hydrodynamic-Acoustic-Cavitation (HAC). *Water Research* . 2012;46(7):2469–2477.

15. Debenedetti PG. Metastable liquids: concepts and principles. Princeton University Press. 1996.

16. Caupin F, Herbert E. Cavitation in water: a review. *Comptes Rendus Physique* . 2006;7(9–10):1000–1017. Nucleation/Nucléation.

17. Temperley HNV, Chambers LG. The behaviour of water under hydrostatic tension: I. *Proceedings of the Physical Society* . 1946;58(4):420.

18. Chapman P, Richards B, Trevena D. Monitoring the growth of tension in a liquid contained in a Berthelot tube. *Journal of Physics E: Scientific Instruments* . 1975;8(9):731.

19. Richards B, Trevena D. The measurement of positive and negative pressures in a liquid contained in a Berthelot tube. *Journal of Physics D: Applied Physics* . 1976;9(11):L123.

20. Jones W, Overton G, Trevena D. Tensile strength experiments with water using a new type of Berthelot tube. *Journal of Physics D: Applied Physics* . 1981;14(7):1283.

21. Vincent R, Simmonds G. Examination of the Berthelot method of measuring tension in liquids. *Proceedings of the Physical Society* . 1943;55(5):376.

22. Williams TL, Trevena DH. Improved and extended theory of the Berthelot tube method of studying liquids under tensile stress. *Nature* . 1977;265(5595):612–613.

23. Jones W, Trevena D. A thermomechanical study of a water-steel Berthelot tube system. *Journal of Physics D: Applied Physics* . 1980;13(10):1871.

24. Fisher JC. The fracture of liquids. *Journal of Applied Physics* . 1948;19(11):1062–1067. .

25. Caupin F. Liquid-vapor interface, cavitation, and the phase diagram of water. *Physical Reviews E* . 2005;71:051605.

26. Alvarenga AD, Grimsditch M, Bodnar RJ. Elastic properties of water under negative pressures. *The Journal of Chemical Physics* . 1993;98:8392–8396.

27. Shmulovich KI, Mercury L, Thiéry R, Ramboz C, Mekki ME. Experimental superheating of water and aqueous solutions. *Geochimica et Cosmochimica Acta* . 2009;73(9):2457–2470.

28. Azouzi MEM, Ramboz C, Lenain JF, Caupin F. A coherent picture of water at extreme negative pressure. *Nature Physics* . 2013;9(1):38–41.

29. Caupin F. Escaping the no man's land: Recent experiments on metastable liquid water. *Journal of Non-Crystalline Solids* . 2015;407:441–448. 7th IDMRCS: Relaxation in Complex Systems.

30. Worthington AM. On the mechanical stretching of liquids: An experimental determination of the volume-extensibility of ethyl-alcohol. *Philosophical Transactions of the Royal Society of London A: Mathematical, Physical and Engineering Sciences* . 1892;183:355–370. .

31. Briggs LJ. Limiting negative pressure of water. *Journal of Applied Physics* . 1950;21(7):721–722. .

32. Winnick J, Cho SJ. PVT behavior of water at negative pressures. *The Journal of Chemical Physics* . 1971;55(5):2092–2097. .

33. Ando K, Liu AQ, Ohl CD. Homogeneous nucleation in water in microfluidic channels. *Phys Rev Lett* . 2012;109:044501.

34. Cole RH. Underwater explosions. Princeton University Press. 1948.

35. Wilson DA, Hoyt JW, Mckune JW. Measurement of tensile strength of liquids by an explosion technique. *Nature* . 1975;253(5494):723–725.

36. Sedgewick S, Trevena D. Limiting negative pressure of water under dynamic stressing. *Journal of Physics D: Applied Physics* . 1976;9(14):1983.

37. Temperley HNV, Trevena DH. Metastable effects associated with the reflection of a pressure pulse at the free surface of water. *Journal of Physics D: Applied Physics* . 1979;12(11):1887.

38. Williams PR, Williams RL. On anomalously low values of the tensile strength of water. *Proceedings of the Royal Society of London A: Mathematical, Physical and Engineering Sciences* . 2000;456(1998):1321–1332. .

39. Couzens DCF, Trevena DH. Critical tension in a liquid under dynamic conditions of stressing. *Nature* . 1969;222(5192):473–474.

40. Sedgewick S, Trevena D. Limiting negative pressure of water under dynamic stressing. *Journal of Physics D: Applied Physics* . 1976;9(14):1983–1990.

41. Overton G, Trevena D. Cavitation phenomena and the occurrence of pressure-tension cycles under dynamic stressing. *Journal of Physics D: Applied Physics* . 1981;14(2):241–250.

42. Carlson GA, Henry KW. Technique for studying dynamic tensile failure in liquids: application to glycerol. *Journal of Applied Physics* . 1973;44(5):2201–2206. .

43. Chesterman W. The dynamics of small transient cavities. *Proceedings of the Physical Society Section B* . 1952;65(11):846.

44. Fujikawa S, Akamatsu T. Experimental investigations of cavitation bubble collapse by a water shock tube. *Bulletin of JSME* . 1978;21(152):223–230.

45. Richards BE, Trevena DH, Edwards DH. Cavitation experiments using a water shock tube. *Journal of Physics D: Applied Physics* . 1980;13(7):1315–1323.

46. Thomas GO, Oakley GL. An experimental investigation of the coupling between gaseous explosion pressures and a water volume in a closed vessel. *Process Safety and Environmental Protection* . 2010;88(1):20–23.

47. Harvey EN, Barnes DK, McElroy WD, Whiteley AH, Pease DC, Cooper KW. Bubble formation in animals. I. Physical factors. *Journal of Cellular and Comparative Physiology* . 1944;24(1):1–22.

48. Iyengar KS, Richardson EG. Measurements on the air-nuclei in natural water which give rise to cavitation. *British Journal of Applied Physics* . 1958;9(4):154.

49. Brennen CE. Cavitation and bubble dynamics. Oxford engineering science series 44, Cambridge University Press. 1995. ISBN 9780195094091,0195094093.

50. Field J. The physics of liquid impact, shock wave interactions with cavities, and the implications to shock wave lithotripsy. *Physics in medicine and biology* . 1991;36(11):1475.

51. Lauterborn W, Bolle H. Experimental investigations of cavitation-bubble collapse in the neighbourhood of a solid boundary. *Journal of Fluid Mechanics* . 1975;72(2):391–399.

52. Tauber A, Mark G, Schuchmann HP, von Sonntag C. Sonolysis of tert–butyl alcohol in aqueous solution. *Journal of the Chemical Society, Perkin Transactions 2* . 1999;:1129–1136.

53. Henglein A. Sonochemistry: Historical developments and modern aspects. *Ultrasonics* . 1987;25(1):6–16.

54. Ashokkumar M. The characterization of acoustic cavitation bubbles: An overview. *Ultrasonics Sonochemistry* . 2011;18(4):864–872. European Society of Sonochemistry (ESS12).

55. Flint EB, Suslick KS. The temperature of cavitation. *Science* . 1991;253(5026):1397–1399. .

56. Suslick KS, Flint EB. Sonoluminescence from non-aqueous liquids. *Nature* . 1987;330(6148):553–555.

57. Jarman P. Sonoluminescence: A discussion. *The Journal of the Acoustical Society of America* . 1960;32(11):1459–1462. .

58. Beckett MA, Hua I. Impact of ultrasonic frequency on aqueous sonoluminescence and sonochemistry. *The Journal of Physical Chemistry A* . 2001;105(15):3796–3802. .

59. Jarman P, Taylor K. Light emission from cavitating water. *British Journal of Applied Physics* . 1964;15(3):321.

60. Hart EJ, Fischer CH, Henglein A. Sonolysis of hydrocarbons in aqueous solution. *International Journal of Radiation Applications and Instrumentation Part C Radiation Physics and Chemistry* . 1990;36(4):511–516.

61. Rae J, Ashokkumar M, Eulaerts O, von Sonntag C, Reisse J, Grieser F. Estimation of ultrasound induced cavitation bubble temperatures in aqueous solutions. *Ultrasonics Sonochemistry* . 2005;12(5):325–329.

62. Hauke G, Fuster D, Dopazo C. Dynamics of a single cavitating and reacting bubble. *Physical Review E* . 2007;75(066310):1–14.

63. Gogate PR, Sutkar VS, Pandit AB. Sonochemical reactors: Important design and scale up considerations with a special emphasis on heterogeneous systems. *Chemical Engineering Journal* . 2011;166(3):1066–1082.

64. Gogate PR, Pandit AB. Engineering design methods for cavitation reactors II: Hydrodynamic cavitation. *AIChE Journal* . 2000;46(8):1641–1649.

65. Kumar PS, Pandit AB. Modeling hydrodynamic cavitation. *Chemical Engineering and Technology* . 1999;22(12):1017–1027.

66. Yan Y, Thorpe R. Flow regime transitions due to cavitation in the flow through an orifice. *International Journal of Multiphase Flow* . 1990;16(6):1023–1045.

67. Gogate PR, Pandit AB. Hydrodynamic cavitation reactors: a state of the art review. *Reviews in Chemical Engineering* . 2001;17(1):1–85.

68. Moholkar V, Kumar PS, Pandit A. Hydrodynamic cavitation for sonochemical effects. *Ultrasonics Sonochemistry* . 1999;6(1 - 2):53–65.

69. Gogate PR, Shirgaonkar IZ, Sivakumar M, Senthilkumar P, Vichare NP, Pandit AB. Cavitation reactors: Efficiency assessment using a model reaction. *AIChE Journal* . 2001;47(11):2526–2538.

70. Lesser M, Field J. The impact of compressible liquids. *Annual review of fluid mechanics* . 1983;15(1):97–122.

71. Gent AN, Lindley PB. Internal rupture of bonded rubber cylinders in tension. *Proceedings of the Royal Society of London A: Mathematical, Physical and Engineering Sciences* . 1959;249(1257):195–205. .

72. Ball JM. Discontinuous equilibrium solutions and cavitation in nonlinear elasticity. *Philosophical Transactions of The Royal Society of London Series A-Mathematical Physical and Engineering Sciences* . 1982;306(1496):557–611.

73. Meyers MA. Dynamic Behavior of Materials. Wiley. 1994. ISBN 047158262X,9780471582625.

74. Hopkinson B. A method of measuring the pressure produced in the detonation of high explosives or by the impact of bullets. *Philosophical Transactions of The Royal Society of London Series A-Mathematical Physical and Engineering Sciences* . 1914;213(497-508):437–456.

75. Blake Jr F. Onset of cavitation in liquids. Ph.d. thesis, Harvard University. 1949.

76. Mørch KA. Cavitation nuclei and bubble formation–A dynamic liquid-solid interface problem. *Journal of Fluids Engineering* . 2000;122(3):494–498.

77. Ando K, Liu AQ, Ohl CD. Homogeneous nucleation in water in microfluidic channels. *Physical Review Letters* . 2012;109:044501.

78. Quinto-Su PA, Ando K. Nucleating bubble clouds with a pair of laser-induced shocks and bubbles. *Journal of Fluid Mechanics* . 2013;733.

79. Fuster D, Pham K, Zaleski S. Stability of bubbly liquids and its connection to the process of cavitation inception. *Physics of Fluids* . 2014;26(4):042002.

80. Andersen A, Mørch KA. Cavitation nuclei in water exposed to transient pressures. *Journal of Fluid Mechanics* . 2015;771:424–448.

81. Fourest T, Laurens JM, Deletombe E, Dupas J, Arrigoni M. Analysis of bubbles dynamics created by Hydrodynamic Ram in confined geometries using the Rayleigh–Plesset equation. *International Journal of Impact Engineering* . 2014;73:66–74.

82. Dear J, Field J. A study of the collapse of arrays of cavities. *Journal of Fluid Mechanics* . 1988;190:409–425.

83. Chesterman W. The dynamics of small transient cavities. *Proceedings of the Physical Society Section B* . 1952;65(11):846.

84. Field J, Lesser MB, Dear J. Studies of two-dimensional liquid-wedge impact and their relevance to liquid-drop impact problems. In: *Proceedings of the Royal Society of London A: Mathematical, Physical and Engineering Sciences*, vol. 401. The Royal Society. 1985:225–249. .

85. Daily J, Pendlebury J, Langley K, Hurd R, Thomson S, Truscott T. Catastrophic cracking courtesy of quiescent cavitation. *Physics of Fluids* . 2014;26(9):091107. .

86. Rodríguez-Rodríguez J, Casado-Chacón A, Fuster D. Physics of beer tapping. *Physical Review Letters* . 2014;113(21):214501.

87. Dular M, Coutier-Delgosha O. Thermodynamic effects during growth and collapse of a single cavitation bubble. *Journal of Fluid Mechanics* . 2013;736:44–66.

88. Glenn LA. On the dynamics of hypervelocity liquid jet impact on a flat rigid surface. *Zeitschrift für angewandte Mathematik und Physik ZAMP* . 1974;25(3):383–398.

89. Ghidaoui MS, Zhao M, McInnis DA, Axworthy DH. A review of water hammer theory and practice. *Applied Mechanics Reviews* . 2005;58(1/6):49.

90. Bergant A, Simpson AR, Tijsseling AS. Water hammer with column separation: A historical review. *Journal of Fluids and Structures* . 2006;22(2):135–171.

91. Kornfeld M, Suvorov L. On the destructive action of cavitation. *Journal of Applied Physics* . 1944;15(6):495–506. .

92. Field J. ELSI conference: invited lecture: liquid impact: theory, experiment, applications. *Wear* . 1999;233:1–12.

93. Makino K, Mossoba MM, Riesz P. Chemical effects of ultrasound on aqueous solutions. Formation of hydroxyl radicals and hydrogen atoms. *The Journal of Physical Chemistry* . 1983;87(8):1369–1377. .

94. Makino K, Mossoba MM, Riesz P. Chemical effects of ultrasound on aqueous solutions. Evidence for hydroxyl and hydrogen free radicals ($O^{\bullet}$ and $H^{\bullet}$) by spin trapping. *Journal of the American Chemical Society* . 1982;104(12):3537–3539. .

95. Warnatz J. Hydrocarbon oxidation at high temperatures. *Berichte der Bunsengesellschaft für physikalische Chemie* . 1983;87(11):1008–1022.

96. Entezari MH, Kruus P. Effect of frequency on sonochemical reactions. I: Oxidation of iodide. *Ultrasonics Sonochemistry* . 1994;1(2):S75–S79.

97. Iida Y, Yasui K, Tuziuti T, Sivakumar M. Sonochemistry and its dosimetry. *Microchemical Journal* . 2005;80(2):159–164. Papers presented at the 2nd Changwon Symposium on Advanced Science and Technology, Changwon, Korea, 5-7 December 2003.

98. Koda S, Kimura T, Kondo T, Mitome H. A standard method to calibrate sonochemical efficiency of an individual reaction system. *Ultrasonics Sonochemistry* . 2003;10(3):149–156.

99. Morison K, Hutchinson C. Limitations of the Weissler reaction as a model reaction for measuring the efficiency of hydrodynamic cavitation. *Ultrasonics Sonochemistry* . 2009;16(1):176–183.

100. Suslick KS, Mdleleni MM, , Ries JT. Chemistry induced by Hydrodynamic Cavitation. *Journal of the American Chemical Society* . 1997;119(39):9303–9304. .

101. Lim M, Ashokkumar M, Son Y. The effects of liquid height/volume, initial concentration of reactant and acoustic power on sonochemical oxidation. *Ultrasonics Sonochemistry* . 2014;21(6):1988 – 1993. {AOSS} 2013.

102. Gogate P, Shaha S, Csoka L. Intensification of cavitational activity in the sonochemical reactors using gaseous additives. *Chemical Engineering Journal* . 2014;239:364–372.

103. Hoffmann MR, Hua I, Höchemer R. Application of ultrasonic irradiation for the degradation of chemical contaminants in water. *Ultrasonics Sonochemistry* . 1996;3(3):S163–S172. Proceedings of the Symposium on the Chemical Effects of Ultrasound in the 1995 International Chemical Congress of Pacific Basin Societies.

104. Rooze J, Rebrov EV, Schouten JC, Keurentjes JT. Dissolved gas and ultrasonic cavitation : A review. *Ultrasonics Sonochemistry* . 2013;20(1):1–11.

105. Luche J, Einhorn C, Einhorn J, Sinisterra-Gago J. Organic sonochenistry : A new interpretation and its consequences. *Tetrahedron Letters* . 1990;31(29):4125–4128.

106. Wood RJ, Lee J, Bussemaker MJ. A parametric review of sonochemistry: Control and augmentation of sonochemical activity in aqueous solutions. *Ultrasonics Sonochemistry* . 2017;38:351–370.

107. González-García J, Sáez V, Tudela I, Díez-Garcia MI, Deseada Esclapez M, Louisnard O. Sonochemical treatment of water polluted by chlorinated organocompounds. A review. *Water* . 2010;2(1):28–74.

108. Mohod AV, Gogate PR, Viel G, Firmino P, Giudici R. Intensification of biodiesel production using hydrodynamic cavitation based on high speed homogenizer. *Chemical Engineering Journal* . 2017;316:751–757.

109. Lim M, Son Y, Khim J. The effects of hydrogen peroxide on the sonochemical degradation of phenol and bisphenol A. *Ultrasonics Sonochemistry* . 2014;21(6):1976–1981. {AOSS} 2013.

110. Randolph TW, Schiltz E, Sederstrom D, Steinmann D, Mozziconacci O, Schöneich C, Freund E, Ricci MS, Carpenter JF, Lengsfeld CS. Do Not Drop: Mechanical shock in vials causes cavitation, protein aggregation, and particle formation. *Journal of Pharmaceutical Sciences* . 2015;104(2):602 – 611.

111. Borah AJ, Agarwal M, Poudyal M, Goyal A, Moholkar VS. Mechanistic investigation in ultrasound induced enhancement of enzymatic hydrolysis of invasive biomass species. *Bioresource Technology* . 2016;213:342–349.

112. Suslick KS. The site of sonochemical reactions. {*IEEE*} *Transactions on Ultrasonics, Ferroelectrics, and Frequency Control* . 1986;33(2):143–147.

113. Kidak R, Ince N. Effects of operating parameters on sonochemical decomposition of phenol. *Journal of Hazardous Materials* . 2006;137(3):1453–1457.

114. Storey BD, Szeri AJ. Water vapour, sonoluminescence and sonochemistry. *Proceedings of the Royal Society of London A: Mathematical, Physical and Engineering Sciences* . 2000;456(1999):1685–1709. .

115. Lohse D, Hilgenfeldt S. Inert gas accumulation in sonoluminescing bubbles. *The Journal of Chemical Physics* . 1997;107(17):6986–6997. .

116. Colarusso P, Serpone N. Sonochemistry II.–Effects of ultrasounds on homogeneous chemical reactions and in environmental detoxification. *Research on Chemical Intermediates* . 1996;22(1):61–89.

117. Sivasankar T, Moholkar VS. Mechanistic approach to intensification of sonochemical degradation of phenol. *Chemical Engineering Journal* . 2009;149(1 - 3):57–69.

118. Fischer CH, Hart EJ, Henglein A. Ultrasonic irradiation of water in the presence of oxygen 18,18O_2: isotope exchange and isotopic distribution of H_2O_2. *The Journal of Physical Chemistry* . 1986;90(9):1954–1956. .

119. Weavers LK, Ling FH, Hoffmann MR. Aromatic compound degradation in water using a combination of sonolysis and ozonolysis. *Environmental Science & Technology* . 1998;32(18):2727–2733. .

120. Kanthale P, Ashokkumar M, Grieser F. Sonoluminescence, sonochemistry (H_2O_2 yield) and bubble dynamics: Frequency and power effects. *Ultrasonics Sonochemistry* . 2008;15(2):143–150.

121. Suslick KS. Sonoluminescence and sonochemistry. In: {*IEEE*} *Ultrasonics Symposium Proceedings. An International Symposium (Cat. No.97CH36118)*, vol. 1. 1997:523–532.

122. Leighton T. The principles of cavitation, vol. 12. London: Blackie Academic & Professional. 1998.

123. Kang JW, Hoffmann MR. Kinetics and mechanism of the sonolytic destruction of methyl tert-butyl ether by ultrasonic irradiation in the presence of ozone. *Environmental Science & Technology* . 1998;32(20):3194–3199. .

124. Nagata Y, Nakagawa M, Okuno H, Mizukoshi Y, Yim B, Maeda Y. Sonochemical degradation of chlorophenols in water. *Ultrasonics Sonochemistry* . 2000;7(3):115–120.

125. Nagata Y, Hirai K, Bandow H, Maeda Y. Decomposition of hydroxybenzoic and humic acids in water by ultrasonic irradiation. *Environmental Science & Technology* . 1996;30(4):1133–1138. .

126. Kidak R, Ince N. Catalysis of advanced oxidation reactions by ultrasound: A case study with phenol. *Journal of Hazardous Materials* . 2007;146(3):630–635. Environmental Applications of Advanced Oxidation Processes.

127. Gogate PR, Pandit AB. A review of imperative technologies for wastewater treatment I: oxidation technologies at ambient conditions. *Advances in Environmental Research* . 2004;8(3):501–551.

128. Visscher AD, Langenhove HV. Sonochemistry of organic compounds in homogeneous aqueous oxidising systems. *Ultrasonics Sonochemistry* . 1998;5(3):87–92.

129. Gogate PR, Pandit AB. A review of imperative technologies for wastewater treatment II: hybrid methods. *Advances in Environmental Research* . 2004;8(3–4):553–597.

130. Dutilleul H, Partaloglu A, Costa PD, Gálvez ME. Shock-induced cavitation as a way of accelerating phenol oxidation in aqueous media. *Chemical Engineering and Processing: Process Intensification* . 2017;112:47–55.

131. Etat de l'Environnement Industriel PACA 2011–2013. . [Online; accessed 2016-11-16].

132. Pisarevsky AM, Polozova IP, Hockridge PM. Chemical oxygen demand. *Russian Journal of Applied Chemistry* . 2005;78(1):101–107.

133. Busca G, Berardinelli S, Resini C, Arrighi L. Technologies for the removal of phenol from fluid streams: A short review of recent developments. *Journal of Hazardous Materials* . 2008;160(2 - 3):265–288.

134. Phenol; MSDS No.15 [Online]; INRS. . [Online; accessed 2016-11-16].

135. Babich H, Davis D. Phenol: A review of environmental and health risks. *Regulatory Toxicology and Pharmacology* . 1981;1(1):90–109.

136. Pan G, Kurumada KI. Hybrid gel reinforced with coating layer for removal of phenol from aqueous solution. *Chemical Engineering Journal* . 2008;138(1 - 3):194–199.

137. Huang J, Wang X, Jin Q, Liu Y, Wang Y. Removal of phenol from aqueous solution by adsorption onto OTMAC-modified attapulgite. *Journal of Environmental Management* . 2007;84(2):229–236.

138. Mohanty K, Das D, Biswas MN. Treatment of phenolic wastewater in a novel multi-stage external loop airlift reactor using activated carbon. *Separation and Purification Technology* . 2008;58(3):311–319.

139. Andreozzi R, Insola A, Caprio V, Marotta R, Tufano V. The use of manganese dioxide as a heterogeneous catalyst for oxalic acid ozonation in aqueous solution. *Applied Catalysis A: General* . 1996;138(1):75–81.

140. Adak A, Pal A. Removal of phenol from aquatic environment by SDS-modified alumina: Batch and fixed bed studies. *Separation and Purification Technology* . 2006;50(2):256–262.

141. Mukherjee S, Kumar S, Misra AK, Fan M. Removal of phenols from water environment by activated carbon, bagasse ash and wood charcoal. *Chemical Engineering Journal* . 2007;129(1 - 3):133 – 142.

142. Kujawski W, Warszawski A, Ratajczak W, Porebski T, Capala W, Ostrowska I. Removal of phenol from wastewater by different separation techniques. *Desalination* . 2004;163(1):287–296.

143. Lipnizki F, Hausmanns S, Ten PK, Field RW, Laufenberg G. Organophilic pervaporation: prospects and performance. *Chemical Engineering Journal* . 1999;73(2):113–129.

144. Hao X, Pritzker M, Feng X. Use of pervaporation for the separation of phenol from dilute aqueous solutions. *Journal of Membrane Science* . 2009;335(1–2):96–102.

145. Lazarova Z, Boyadzhieva S. Treatment of phenol–containing aqueous solutions by membrane–based solvent extraction in coupled ultrafiltration modules. *Chemical Engineering Journal* . 2004;100(1 - 3):129–138.

146. Zheng H, Wang B, Wu Y, Ren Q. Instability mechanisms of supported liquid membrane for phenol transport. *Chinese Journal of Chemical Engineering* . 2009;17(5):750–755.

147. Juang R, Huang W. Use of membrane contactors as two–phase bioreactors for the removal of phenol in saline and acidic solutions. *Journal of Membrane Science* . 2008;313(1–2):207–216.

148. Das K, Praveen P, Loh K. Importance of uniform distribution of impregnated trioctylphosphine oxide in hollow fiber membranes for simultaneous extraction/stripping of phenol. *Chemical Engineering Journal* . 2017;308:727–737.

149. Moussavi G, Mahmoudi M, Barikbin B. Biological removal of phenol from strong wastewaters using a novel {MSBR}. *Water Research* . 2009;43(5):1295–1302.

150. Balaji S, Chung SJ, Thiruvenkatachari R, Moon IS. Mediated electrochemical oxidation process: Electro-oxidation of cerium(III) to cerium(IV) in nitric acid medium and a study on phenol degradation by cerium(iv) oxidant. *Chemical Engineering Journal* . 2007;126(1):51–57.

151. Matta R, Hanna K, Chiron S. Oxidation of phenol by green rust and hydrogen peroxide at neutral pH. *Separation and Purification Technology* . 2008;61(3):442–446.

152. Melero J, Calleja G, Martínez F, Molina R, Pariente M. Nanocomposite Fe_2O_3/SBA-15: an efficient and stable catalyst for the catalytic wet peroxidation of phenolic aqueous solutions. *Chemical Engineering Journal* . 2007;131(1):245–256.

153. Aguiar A, Ferraz A. Fe_3^+- and Cu_2^+-reduction by phenol derivatives associated with Azure B degradation in fenton-like reactions. *Chemosphere* . 2007;66(5):947 – 954.

154. Vasu AE. Removal of phenol and o-cresol by adsorption onto activated carbon. *E-Journal of Chemistry* . 2008;5(2):224–232.

155. for Toxic Substances A, Registry D. Priority List of Hazardous Substances. . 2016. [Online; accessed 2017-01-05].

156. for Toxic Substances A, Registry D. Toxicological profile for Phenol. . 2008. [Online; accessed 2017-01-05].

157. Mathieu JM. Phenol. Acetone. alpha-Methylstyrène. *Techniques de l'ingénieur: Fabrication des grands produits industriels en chimie et pétrochimie* . 2002;(J6490 V1).

158. Barrios-Martinez A, Barbot E, Marrot B, Moulin P, Roche N. Degradation of synthetic phenol-containing wastewaters by {MBR}. *Journal of Membrane Science* . 2006;281(1 – 2):288 – 296.

159. for Toxic Substances A, Registry D. Medical Management Guidelines for Phenol. . 2003. [Online; accessed 2017-01-05].

160. des Substances Chimiques ET. Seuils de Toxicité aigue - Phénol. . 2008. [Online; accessed 2017-01-05].

161. for Toxic Substances A, Registry D. Priority Data Needs for Phenol. . 2016. [Online; accessed 2016-11-16].

162. Huang Y, Ma X, Liang G, Yan H. Adsorption of phenol with modified rectorite from aqueous solution. *Chemical Engineering Journal* . 2008;141(1 - 3):1–8.

163. Mohanty K, Das D, Biswas M. Adsorption of phenol from aqueous solutions using activated carbons prepared from Tectona grandis sawdust by $ZnCl_2$ activation. *Chemical Engineering Journal* . 2005;115(1 - 2):121–131.

164. Jiang H, Fang Y, Fu Y, Guo QX. Studies on the extraction of phenol in wastewater. *Journal of Hazardous Materials* . 2003;101(2):179–190.

165. de la Diffusion du Droit LSP. Décret n.2001-1220 du 20 décembre 2001 relatif aux eaux destinées à la consommation humaine, à l'exclusion des eaux minérales naturelles. . 2001. [Online; accessed 2017-01-05].

166. Lin SH, Juang RS. Adsorption of phenol and its derivatives from water using synthetic resins and low-cost natural adsorbents: A review. *Journal of Environmental Management* . 2009;90(3):1336–1349.

167. Alshehri SM, Naushad M, Ahamad T, Alothman ZA, Aldalbahi A. Synthesis, characterization of curcumin based ecofriendly antimicrobial bio-adsorbent for the removal of phenol from aqueous medium. *Chemical Engineering Journal* . 2014;254:181–189.

168. Jia Q, Lua AC. Effects of pyrolysis conditions on the physical characteristics of oil–palm–shell activated carbons used in aqueous phase phenol adsorption. *Journal of Analytical and Applied Pyrolysis* . 2008;83(2):175–179.

169. Aksu Z, Yener J. A comparative adsorption/biosorption study of mono-chlorinated phenols onto various sorbents. *Waste management* . 2001;21(8):695–702.

170. Lua AC, Jia Q. Adsorption of phenol by oil–palm-shell activated carbons in a fixed bed. *Chemical Engineering Journal* . 2009;150(2):455–461.

171. Kadirvelu K, Kavipriya M, Karthika C, Radhika M, Vennilamani N, Pattabhi S. Utilization of various agricultural wastes for activated carbon preparation and application for the removal of dyes and metal ions from aqueous solutions. *Bioresource Technology* . 2003;87(1):129–132.

172. Mohanty K, Jha M, Meikap BC, Biswas MN. Preparation and characterization of activated carbons from terminalia arjuna nut with zinc chloride activation for the removal of phenol from wastewater. *Industrial & Engineering Chemistry Research* . 2005;44(11):4128–4138. .

173. Ahmadpour A, Do D. The preparation of activated carbon from macadamia nutshell by chemical activation. *Carbon* . 1997;35(12):1723 –1732.

174. Goud VV, Mohanty K, Rao MS, Jayakumar NS. Phenol removal from aqueous solutions by tamarind nutshell activated carbon: Batch and column studies. *Chemical Engineering and Technology* . 2005;28(7):814–821.

175. Lussier MG, Shull JC, Miller DJ. Activated carbon from cherry stones. *Carbon* . 1994;32(8):1493–1498.

176. Smets K, De Jong M, Lupul I, Gryglewicz G, Schreurs S, Carleer R, Yperman J. Rapeseed and raspberry seed cakes as inexpensive raw materials in the production of activated carbon by physical activation: Effect of activation conditions on textural and phenol adsorption characteristics. *Materials* . 2016;9(7):565.

177. Banat F, Al-Bashir B, Al-Asheh S, Hayajneh O. Adsorption of phenol by bentonite. *Environmental Pollution* . 2000;107(3):391–398.

178. Hebatpuria VM, Arafat HA, Rho HS, Bishop PL, Pinto NG, Buchanan RC. Immobilization of phenol in cement-based solidified/stabilized hazardous wastes using regenerated activated carbon: leaching studies. *Journal of Hazardous Materials* . 1999;70(3):117–138.

179. Mollah AH, Robinson CW. Pentachlorophenol adsorption and desorption characteristics of granular activated carbon–I. Isotherms. *Water Research* . 1996;30(12):2901–2906.

180. SRengaraj, Moon SH, Sivabalan R, Arabindoo B, Murugesan V. Removal of phenol from aqueous solution and resin manufacturing industry wastewater using an agricultural waste: rubber seed coat. *Journal of Hazardous Materials* . 2002;89(2 - 3):185–196.

181. Nayak PS, Singh BK. Removal of phenol from aqueous solutions by sorption on low cost clay. *Desalination* . 2007;207(1):71–79.

182. Cote G. Extraction liquide-liquide. Présentation générale. *Techniques de l'ingénieur Opérations unitaires : extractions fluide/fluide et fluide/solide* . 1998;(j2760).

183. Kentish S, Stevens G. Innovations in separations technology for the recycling and re-use of liquid waste streams. *Chemical Engineering Journal* . 2001;84(2):149–159. Environmental Chemical Engineering.

184. Palma M, Paiva J, Zilli M, Converti A. Batch phenol removal from methyl isobutyl ketone by liquid–liquid extraction with chemical reaction. *Chemical Engineering and Processing: Process Intensification* . 2007;46(8):764–768.

185. Kiezyk PR, Mackay D. Waste water treatment by solvent extraction. *The Canadian Journal of Chemical Engineering* . 1971;49(6):747–752.

186. Li Z, Wu M, Jiao Z, Bao B, Lu S. Extraction of phenol from wastewater by N-octanoylpyrrolidine. *Journal of Hazardous Materials* . 2004;114(1 - 3):111–114.

187. Garrido-Baserba M, Molinos-Senante M, Abelleira-Pereira J, Fdez-Guelfo L, Poch M, Hernandez-Sancho F. Selecting sewage sludge treatment alternatives in modern wastewater treatment plants using environmental decision support systems. *Journal of Cleaner Production* . 2015;107:410–419.

188. Huang C, Dong C, Tang Z. Advanced chemical oxidation: Its present role and potential future in hazardous waste treatment. *Waste Management* . 1993;13(5):361–377.

189. Imamura S. Catalytic and noncatalytic wet oxidation. *Industrial & Engineering Chemistry Research* . 1999;38(5):1743–1753. .

190. Eiroa M, Vilar A, Kennes C, Veiga M. Effect of phenol on the biological treatment of wastewaters from a resin producing industry. *Bioresource Technology* . 2008;99(9):3507–3512.

191. Chan YJ, Chong MF, Law CL, Hassell D. A review on anaerobic–aerobic treatment of industrial and municipal wastewater. *Chemical Engineering Journal* . 2009;155(1–2):1–18.

192. Perrin R, Scharff JP. Chimie Industrielle, Volumes 1 and 2. *Journal of Chemical Education* . 1994;71(2):A54. .

193. Tziotzios G, Economou C, Lyberatos G, Vayenas D. Effect of the specific surface area and operating mode on biological phenol removal using packed bed reactors. *Desalination* . 2007;211(1):128–137.

194. Zainudin NF, Abdullah AZ, Mohamed AR. Characteristics of supported nano-TiO_2/ZSM-5/silica gel (SNTZS): Photocatalytic degradation of phenol. *Journal of Hazardous Materials* . 2010;174(1 - 3):299–306.

195. Luo H, Liu G, Zhang R, Jin S. Phenol degradation in microbial fuel cells. *Chemical Engineering Journal* . 2009;147(2 - 3):259–264.

196. Chan CH, Lim PE. Evaluation of sequencing batch reactor performance with aerated and unaerated {FILL} periods in treating phenol-containing wastewater. *Bioresource Technology* . 2007;98(7):1333–1338.

197. Uygur A, Kargi F. Phenol inhibition of biological nutrient removal in a four-step sequencing batch reactor. *Process Biochemistry* . 2004;39(12):2123–2128.

198. Luck F. A review of industrial catalytic wet air oxidation processes. *Catalysis Today* . 1996;27(1):195–202.

199. Luck F. Wet air oxidation: past, present and future. *Catalysis Today* . 1999;53(1):81–91.

200. Debellefontaine H, Chakchouk M, Foussard J, Tissot D, Striolo P. Treatment of organic aqueous wastes: Wet air oxidation and wet peroxide oxidation. *Environmental Pollution* . 1996;92(2):155–164.

201. Zou LY, Li Y, Hung YT. Wet air oxidation for waste treatment. Springer. ISBN 978-1-59745-173-4. 2007:575–610.

202. Mishra VS, Mahajani VV, Joshi JB. Wet air oxidation. *Industrial & Engineering Chemistry Research* . 1995;34(1):2–48.

203. Andreozzi R, Caprio V, Insola A, Marotta R. Advanced Oxidation Processes (AOP) for water purification and recovery. *Catalysis Today* . 1999;53(1):51–59.

204. Deng Y, Zhao R. Advanced Oxidation Processes (AOPs) in wastewater treatment. *Current Pollution Reports* . 2015;1(3):167–176.

205. Glaze WH. Drinking–water treatment with ozone. *Environmental Science & Technology* . 1987;21(3):224–230. PMID: 22185096, .

206. Turhan K, Uzman S. Removal of phenol from water using ozone. *Desalination* . 2008;229(1):257–263.

207. Kasprzyk-Hordern B, Ziółek M, Nawrocki J. Catalytic ozonation and methods of enhancing molecular ozone reactions in water treatment. *Applied Catalysis B: Environmental* . 2003;46(4):639–669.

208. Esplugas S, Giménez J, Contreras S, Pascual E, Rodriguez M. Comparison of different advanced oxidation processes for phenol degradation. *Water Research* . 2002;36(4):1034–1042.

209. Venkatachalam N, Palanichamy M, Murugesan V. Sol–gel preparation and characterization of alkaline earth metal doped nano-TiO_2: Efficient photocatalytic degradation of 4-chlorophenol. *Journal of Molecular Catalysis A: Chemical* . 2007;273(1–2):177–185.

210. Baban A, Yediler A, Lienert D, Kemerdere N, Kettrup A. Ozonation of high strength segregated effluents from a woollen textile dyeing and finishing plant. *Dyes and Pigments* . 2003;58(2):93–98.

211. Kušić H, Koprivanac N, Božić AL, Selanec I. Photo-assisted Fenton type processes for the degradation of phenol: A kinetic study. *Journal of Hazardous Materials* . 2006;136(3):632–644.

212. Fenton HJH. LXXIII.-Oxidation of tartaric acid in presence of iron. *Journal of the Chemical Society, Transactions* . 1894;65:899–910.

213. Barb WG, Baxendale JH, George P, Hargrave KR. Reactions of ferrous and ferric ions with hydrogen peroxide. Part I.-The ferrous ion reaction. *Transactions of the Faraday Society* . 1951;47:462–500.

214. Pignatello JJ. Dark and photoassisted iron(3+)-catalyzed degradation of chlorophenoxy herbicides by hydrogen peroxide. *Environmental Science & Technology* . 1992;26(5):944–951. .

215. Barb WG, Baxendale JH, George P, Hargrave KR. Reactions of ferrous and ferric ions with hydrogen peroxide. Part II.-The ferric ion reaction. *Transactions of the Faraday Society* . 1951;47:591–616.

216. Dunford H. Oxidations of iron(II)/(III) by hydrogen peroxide: from aquo to enzyme. *Coordination Chemistry Reviews* . 2002;233–234:311–318.

217. Neyens E, Baeyens J. A review of classic Fenton's peroxidation as an advanced oxidation technique. *Journal of Hazardous Materials* . 2003;98(1 - 3):33–50.

218. Babuponnusami A, Muthukumar K. A review on Fenton and improvements to the Fenton process for wastewater treatment. *Journal of Environmental Chemical Engineering* . 2014;2(1):557–572.

219. Falcon M, Peyrille B, Reihac P, Foussard J, Debellefontaine H. Oxydation en voie humide de la pollution organique aqueuse par le peroxyde d'hydrogène Procédé "Wet Peroxide Oxidation" (WPO®) Etude de nouveaux catalyseurs. *Journal of Water Science* . 1993;6(4):411–426.

220. Duesterberg CK, Mylon SE, Waite TD. pH effects on iron–catalyzed oxidation using Fenton's reagent. *Environmental Science & Technology* . 2008;42(22):8522–8527. PMID: 19068842, .

221. Chang CY, Hsieh YH, Cheng KY, Hsieh LL, Cheng TC, Yao KS. Effect of pH on Fenton process using estimation of hydroxyl radical with salicylic acid as trapping reagent. *Water Science and Technology* . 2008;58(4):873–879. .

222. Legrini O, Oliveros E, Braun AM. Photochemical processes for water treatment. *Chemical Reviews* . 1993;93(2):671–698. .

223. Bhatkhande DS, Pangarkar VG, Beenackers AA. Photocatalytic degradation for environmental applications: a review. *Journal of Chemical Technology and Biotechnology* . 2002;77(1):102–116.

224. Chun H, Yizhong W, Hongxiao T. Destruction of phenol aqueous solution by photocatalysis or direct photolysis. *Chemosphere* . 2000;41(8):1205–1209.

225. Chiou CH, Wu CY, Juang RS. Influence of operating parameters on photocatalytic degradation of phenol in UV/TiO_2 process. *Chemical Engineering Journal* . 2008;139(2):322–329.

226. Chiou CH, Wu CY, Juang RS. Photocatalytic degradation of phenol and m-nitrophenol using irradiated TiO_2 in aqueous solutions. *Separation and Purification Technology* . 2008;62(3):559–564.

227. Yawalkar AA, Bhatkhande DS, Pangarkar VG, Beenackers AA. Solar–assisted photochemical and photocatalytic degradation of phenol. *Journal of Chemical Technology and Biotechnology* . 2001;76(4):363–370.

228. Ray AK. A new photocatalytic reactor for destruction of toxic water pollutants by advanced oxidation process. *Catalysis Today* . 1998;44(1–4):357–368.

229. Peiró AM, Ayllón JA, Peral J, Doménech X. TiO_2-photocatalyzed degradation of phenol and ortho-substituted phenolic compounds. *Applied Catalysis B: Environmental* . 2001;30(3–4):359–373.

230. Fuster D, Dutilleul H, Guibert P, Da Costa P, Zaleski S. Dispositif et procédé de traitement de liquide par cavitation. 2015. SATT Lutech, FR 1558892.

231. Rivas DF, Stricker L, Zijlstra AG, Gardeniers HJ, Lohse D, Prosperetti A. Ultrasound artificially nucleated bubbles and their sonochemical radical production. *Ultrasonics Sonochemistry* . 2013;20(1):510–524.

232. Rienstra SS, Hirschberg AA. An introduction to acoustics. . 2004. Online; accessed 03 April 2017.

233. Igualada E. On the translation of bubbles under the effect of short pressure pulses. Phd thesis, Universidad Carlos III. 2016.

234. Medina A. Experimental and analytical study of the interaction between short acoustic pulses and small clouds of microbubbles. Phd thesis, Universidad Carlos III. 2015.

235. Brenner MP, Hilgenfeldt S, Lohse D. Single-bubble sonoluminescence. *Reviews of Modern Physics* . 2002;74:425–484.

236. Williams P, Williams P, Brown S. A study of liquid jets formed by bubble collapse under shock waves in elastic and Newtonian liquids. *Journal of Non-Newtonian Fluid Mechanics* . 1998;76(1–3):307–325.

237. Brown S, Williams P. The tensile behaviour of elastic liquids under dynamic stressing. *Journal of Non-Newtonian Fluid Mechanics* . 2000;90(1):1–11.

238. Gordon M, Yerushalmi J, Shinnar R. Instability of jets of non–newtonian fluids. *Transactions of the Society of Rheology* . 1973;17(2):303–324. .

239. Obreschkow D, Tinguely M, Dorsaz N, Kobel P, De Bosset A, Farhat M. Universal scaling law for jets of collapsing bubbles. *Physical Review Letters* . 2011;107(20):204501.

240. Drijvers D, Langenhove HV, Beckers M. Decomposition of phenol and trichloroethylene by the ultrasound/H_2O_2/CuO process. *Water Research* . 1999;33(5):1187–1194.

241. Devlin HR, Harris IJ. Mechanism of the oxidation of aqueous phenol with dissolved oxygen. *Industrial & Engineering Chemistry Fundamentals* . 1984;23(4):387–392. .

242. Duprez D, Delanoë F, Barbier J, Isnard P, Blanchard G. Catalytic oxidation of organic compounds in aqueous media. *Catalysis Today* . 1996;29(1):317–322.

243. Alejandre A, Medina F, Rodriguez X, Salagre P, Sueiras J. Preparation and activity of Cu-Al mixed oxides via hydrotalcite-like precursors for the oxidation of phenol aqueous solutions. *Journal of Catalysis* . 1999;188(2):311–324.

244. Péroxyde d'hydrogène et solutions aqueuses; MSDS No.123 [Online]; INRS. . [Online; accessed 2017-04-05].

245. Jiang Y, Pétrier C, Waite T. Effect of pH on the ultrasonic degradation of ionic aromatic compounds in aqueous solution. *Ultrasonics Sonochemistry* . 2002;9(3):163–168.

246. Mijangos F, Varona F, Villota N. Changes in solution color during phenol oxidation by Fenton reagent. *Environmental Science & Technology* . 2006;40(17):5538–5543. PMID: 16999137, .